Technical Report

TR-01-34

Measurements of cutter forces and cutter temperature of boring machine in Äspö Hard Rock Laboratory

Z X Zhang, S Q Kou, P-A Lindqvist
Luleå University of Technology

April 2001

Svensk Kärnbränslehantering AB
Swedish Nuclear Fuel
and Waste Management Co
Box 5864
SE-102 40 Stockholm Sweden
Tel 08-459 84 00
+46 8 459 84 00
Fax 08-661 57 19
+46 8 661 57 19

Measurements of cutter forces and cutter temperature of boring machine in Äspö Hard Rock Laboratory

Z X Zhang, S Q Kou, P-A Lindqvist
Luleå University of Technology

April 2001

Keywords: EDZ, TBM, cutter force, rock mechanical properties, uniaxial compressive strength, uniaxial tensile strength, cracks caused by mechanical boring.

Abstract

This report presents both the testing methods used and the testing results obtained for cutter forces and cutter temperature during field boring in Äspö Hard Rock Laboratory.

In order to estimate the strains induced by cutter forces in the cutter shaft and choose proper transducers, first a numerical simulation was performed. The simulation results indicated that the cutter forces should be measurable by ordinary strain gauges. Furthermore, an independent three-direction loading system for laboratory calibration was set up to solve force-coupling problems appearing in field measurements. By means of the established measuring system, which was proved successful in the laboratory, the normal forces, tangential forces, and side forces of two button cutters in the boring machine were measured in the field. In addition, the temperature in the shaft of the front cutter was measured. After the measurements of the cutter forces and cutter temperature, rock core samples were taken from the bottom and the wall of the testing borehole. Then the samples were cut, polished, and examined by means of the Scanning Electron Microscope (SEM). After that, the lengths of major cracks induced by the cutters in the rock samples were measured, and an approximate relationship between the length of the medium cracks and the relevant cutter forces was obtained. This relationship was compared with the theoretical relationship established before. Finally, according to the measured results, the cracked zones around the borehole were described. The results show that: (1) there are two kinds of cracked zones: one in the borehole wall and the other in the bottom of the borehole. The depth of the cracked zone in the borehole bottom is much larger than that in the borehole wall because the maximum normal force of the front cutter is always much larger than that of the gauge cutter. (2) Each cracked zone includes a densely cracked zone and all the longest medium cracks caused by mechanical boring. (3) According to the measurements for four rock core samples, the maximum depth of the cracked zone in the borehole bottom is 27.1 mm, and the maximum depth of the densely cracked zone is 2.5–3 mm.

Sammanfattning

I denna rapport presenteras både testmetoder och resultat från mätning av verktygskrafter och temperatur under fullborrning av schakt i Äspölaboratoriet.

För att bedöma deformationer som induceras i axlarna på verktygen (cutters) och för rätt val av kraftgivare genomfördes numeriska beräkningar. Dessa visade att vanliga trådtöjningsgivare kunde användas. Ett system med oberoende belastning i tre riktningar för kalibrering i laboratorium av kraftgivare monterades för att lösa problemet med koppling mellan givare under fältmätningen. Med hjälp av det därpå utvecklade mätsystemet, som testades i laboratorium, mättes normalkraft, tangentiell kraft och sidokraft på två verktyg i fält. Dessutom mättes temperaturen i axeln på ett av verktygen i fronten på borrhuvudet. Efter mätning av verktygskrafter och temperatur, uttogs borrkärnor från botten och väggar på det schakt som borrats. Proverna sågades, polerades och undersöktes i svepelektronmikroskop. Längden på sprickor som uppstått under verktygen mättes och ett approximativt samband mellan längden på mediansprickor och relevanta verktygskrafter kunde skapas. Detta samband jämfördes med teoretiska samband som etablerats tidigare. Slutligen kunde, utgående från de erhållna resultaten, den spruckna zonen omkring schaktet beskrivas. Resultaten visar att: (1) två olika sprickzoner kan utskiljas: en i väggarna och en i botten på schaktet. Djupet på den uppspruckna zonen i botten är mycket större än i väggarna på schaktet beroende på att den maximala normalkraften på verktyg riktat framåt (front cutter) alltid är mycket högre än på verktyget mot väggen (gauge cutter). (2) Varje sprickzon inkluderar dels en kraftigt uppsprucken zon dels glest liggande, långa mediansprickor. (3) Från mätningen av fyra bergprover har maximala djupet på mediansprickor i schaktbotten uppmätts till 27,1 mm och maximala djupet på den kraftigt uppspruckna zonen till 2,5–3,0 mm.

Contents

Page

1 Introduction

The formation of subsurface fractures in the tunnel or borehole wall after mechanical boring is of great concern in the design of nuclear waste storage. Therefore, it is important to measure the real forces of the cutters of a TBM machine directly in the field while it is excavating rock. The aims of measuring the real forces can be summarised as follows:

- to verify and modify the theoretical models for mechanical rock penetration established at the Division of Mining Engineering, Luleå University of Technology on the basis of laboratory tests,
- to investigate the possible effects of the machine parameters on rock excavation, particularly on crack formation,
- to provide a feasible method of choosing an optimum excavation method or relevant mechanical excavation parameters for forthcoming tunnel excavation and borehole drilling in nuclear waste storage engineering,
- to propose some comments on the design of the TBM machine according to field measurements.

Force measurement on a disc cutter or cutter head during rock fragmentation in the laboratory has been widely reported by many authors, such as Takaoka et al. /1973/, Morrell and Larson /1974/, Wang et al. /1974/, Lindqvist et al. /1979, 1994/, Snowdon et al. /1982/, Roxborough /1985/, and Ozdemir and Dollinger /1987/. The laboratory tests have usually been performed on a small scale and by using a single cutter. The cutter has been installed on modified common machines for linear cutting, in which the cutter has mostly been fixed in position and the rock sample has been displaced. The vertical and lateral forces and the displacement of the cutter have been sensed by strain gauges and a displacement transducer attached to the loading machine or the support of the rock sample. These simplified test designs are much easier and economical for the investigation of many factors which are very helpful in the study of rock fragmentation and which benefit boring machine manufacturers. On the basis of the experimental results, some formulas and theoretical models have been established. Therefore, laboratory rock fragmentation testing is an important method.

Field rock fragmentation has long been a common practice. Global boring parameters such as penetration rate, thrust, and rotation speed can now be obtained as routine records. Concerning information relevant to the machine head or cutters, the situation is different. A special test design is required to take into account the underground working conditions, the rotating cutter head, continuous rock cutting by a group of cutters, etc.

Field tests of the cutter forces on a boring machine such as the tunnel boring machine (TBM) have not been so extensive, mainly due to the inconvenience of instrumentation and the complexity of field working conditions. The cutter force is one important parameter in cutter design and in understanding the rock fragmentation process in the field. An increasing interest in field tests is arising to take into account factors which are ignored in laboratory tests, and to verify and calibrate the established models. Field

tests, although few, have been attempted /Hopkins and Foden, 1979; Samuel and Seow, 1984/.

The field conditions of rock excavation are very complicated, since the machine head and cutters not only progress forward, but also rotate in the excavation face. The control of both the machine and the rock fragmentation is performed by the operator on the machine platform or surface, far from the machine head. In addition, the environment of rock fragmentation is very tough, with substantial vibration of the equipment, high humidity, and a great deal of dust or floating cuttings, which can deteriorate the instruments and the data logging. Therefore high demands are made on the installation of transducers and transmitters, and special care is required during the measurement.

Hopkins and Foden /1979/ used a series of strain gauges welded at different locations on a cutter shaft to measure the normal force and tangential force of a raise-boring machine during field excavation. A telemetry system, consisting of a transmitter, a receiver and a power supply, was used to transmit the information from the rotating cutter head to the receiver near the raise-boring machine /Hopkins and Foden, 1979/. Nickel cadmium batteries were used to drive the electronic units on the cutter head. The telemetry system was proved to be able to transmit the data from holes over 100 metres deep.

In the TBM case, a rotary joint in the centre of the cutting head has been used to transmit four-channel signals of the force components and moment /Samuel and Seow, 1984/. In this slip ring method, the power and signals are coupled directly between the strain gauges and the ground instruments by a connector, which is composed of one stationary part and one rotating part. Depending on the number of signal channels, a multiple channel connector is needed. The connector has to be specially designed to fit the borer pipe and has to be installed close to the machine to facilitate the connection of signals.

In the direct connecting method all the signals and the power supply are connected by a multi-channel cable from the cutter head to the surface. Since the cable is winded, the length should suffice to match the rotation speed (10 rpm) and the required recording time (5–10 min). For a drill pipe of a diameter of 150 to 300 mm, the cable length is about 50 to 100 m. This method is economical, but the signal must be strong for the long conducting path. Some mechanical damage might easily be caused to the cable and connected devices.

Of the three methods of signal transmission, the telemetry system is the most reliable and easy to install. It causes least disturbance to the boring machine. In the slip ring method, the contact resistance is more sensitive to vibration, which may distort the signals and result in large error in the logging data. Hence it is not appropriate to use it in boring conditions.

On the basis of the above background, we chose strain gauges and the telemetry method to measure the cutter forces in boring.

2 Experimental system

2.1 Requirements of field tests

The main parameters to be measured are the forces on the cutters, which can be decomposed into the normal force, tangential force and side force (or lateral force), of which the normal force is most important. See Figure 2-1 for their definitions (the tangential force is perpendicular to the paper surface in Figure 2-1).

The global boring parameters needed are Total Thrust, Torque, Penetration Rate, and Rotation Speed.

Core-drilled rock samples from the borehole bottom are to be examined for an investigation of cracking.

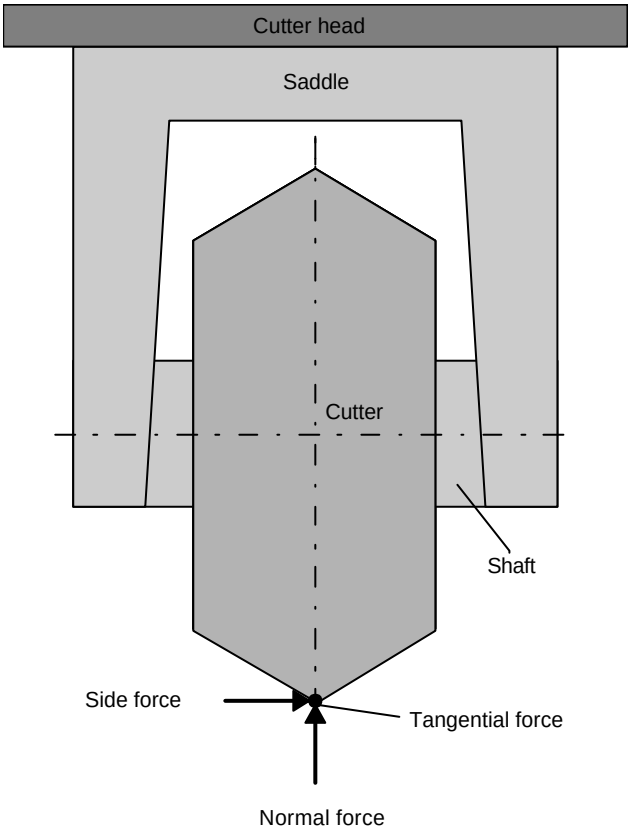

Figure 2-1. *Diagram of three forces on a cutter.*

2.2 Test design and instrumentation

2.2.1 Boring equipment

According to the design concept for nuclear waste storage at Äspö, the waste repository will be situated in a series of vertical holes with a diameter of 1.75 m and a length of 8 m. Such holes are to be bored by a new machine named the Boretec DS 1.6 TBM. This machine is shown in Figure 2-2.

In the Boretec machine, there are a total of 20 cutters distributed on its cutter head. Our field tests were performed only in borehole 2, as numbered by Äspö Laboratory. While borehole 2 was bored, a total of 16 button cutters and 4 disc cutters were installed in the cutter head. Each button cutter had 30 carbide buttons (two rows, each of which had 15 buttons) situated on the roller of the cutter. The vacuum method was used to move the cuttings out of the 1.75 m-diameter and 8.0 m-length hole. In instantaneous rock breakage, each cutter had one to three buttons in contact with the bottom of the borehole. The spacing between the neighbouring buttons or cutting trajectories was about 3 cm. The nine side cutters were installed slantingly with the axis of the borehole. The total designed maximum thrust was 2470 kN. The rotation speed was 0 to 20 rpm.

Of all the cutters on the cutter head, from two button cutters we measured the cutter forces. One cutter was in the outmost circumference of the cutter head, so it was called the gauge cutter, and the other was in a front position and was therefore called the front cutter. From these two cutters we could obtain the cutter force information in typical loading situations.

2.2.2 Instruments

The instrumentation system consists of the following components:

1. Gauges. The popular bonded metal-foil gauges (resistance 350 Ω) were chosen, which are suitable for attachment onto metal and follow well the deformation of the measured component. For the measurement of the three forces on the cutter, strain gauges of the type named the WK-06-125BT-350 were employed. Their matrix sizes are 9.4×4.1 mm and their grid sizes 5.46×1.57 mm. In normal working environments, the strain gauges can work at temperatures of –269° to +290°C. For the temperature measurement, gauges of the type named the ETG-50A/Option E with the LST Matching Network LST-10C-350D were used; and they can work at temperatures of –150° to +260°C. All the gauges are manufactured by Measurements Group, Micro-Measurements Division in the USA.

   Because the strain and temperature gauges were to work in a tough field environment, the glue M-Bond 610 was used to bond the gauges on the shaft. This glue is apt for dynamic stress analysis and can work at temperatures of –269° to +370°C. After the gauges were bonded on the surfaces of the shaft, a protection material (silicone rubber), 3145-RTV, was put on the gauges. This protection material can stand temperatures of –75° to +315°C. The most appropriate position for placing the gauges is the shaft of the cutter. The shaft diameter is 70 mm. The saddle span is about 182 mm. To obtain the three orthogonal force components, three groups of strain gauges were placed onto the cutter shaft. The strain gauges were distributed at locations where the largest strain corresponding to the component force would take place, see Figure 2-3. Here we consider the two ends of the shaft as fixed supports according to the true structure of the cutter body. Therefore, E and F should have the maximum (or near maximum) tensile stress and the maximum (or near maximum) compressive stress corresponding to the side force, respectively.

Figure 2-2. *Boring machine Boretec DS 1.6 and its cutter head.*

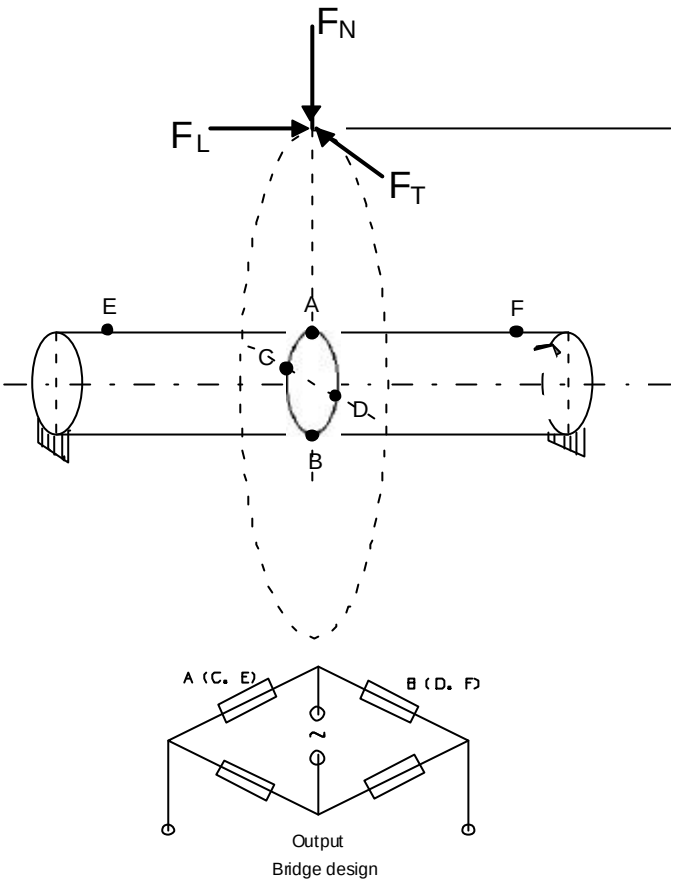

Figure 2-3. *Arrangement of strain gauges on the cutter shaft and bridge circuits.*

2. Bridge circuit. Two strain gauges were needed for measuring one force component, and they were connected in a bridge circuit. Besides this we put two other temperature gauges to measure the temperature variation on the front cutter. To obtain the strain signals of the three force components, the strain gauges were connected in the bridge circuit at the positions A to F as shown in Figure 2-3. The circuit package was protected in a box and located in a proper place behind the cutter head.

3. Power and signal transmission. The telemetry method was employed and the system consisted of a transmitter, a receiver and a power supply, see Figure 2-4. For our purpose, the telemetry system was able to measure seven-channel signals (six for force and one for temperature). The transmitter is portable and can stand vibration, high temperature (up to +85°C) and high acceleration. It was installed at the back of the cutter head. The receiver antenna was positioned on the upper part of the boring machine and the receiver instrument at the control cabin for safety and easy coupling with the data acquisition system. The power supply to the strain and temperature gauges was a battery (operating time about 4 hours) which was compact and easy to handle. The DT 11 (6 channels) and DT 12 (1 channel) transmitters were used to transmit force and temperature signals, respectively. Both kinds of transmitters can work at temperatures of –10° to +85°C. A six-channel receiver for the force measurement and a one-channel receiver for the temperature measurement were used to pick up and amplify all the signals from the transmitters. The frequency of both the transmitters and the receivers can reach 300 kHz.

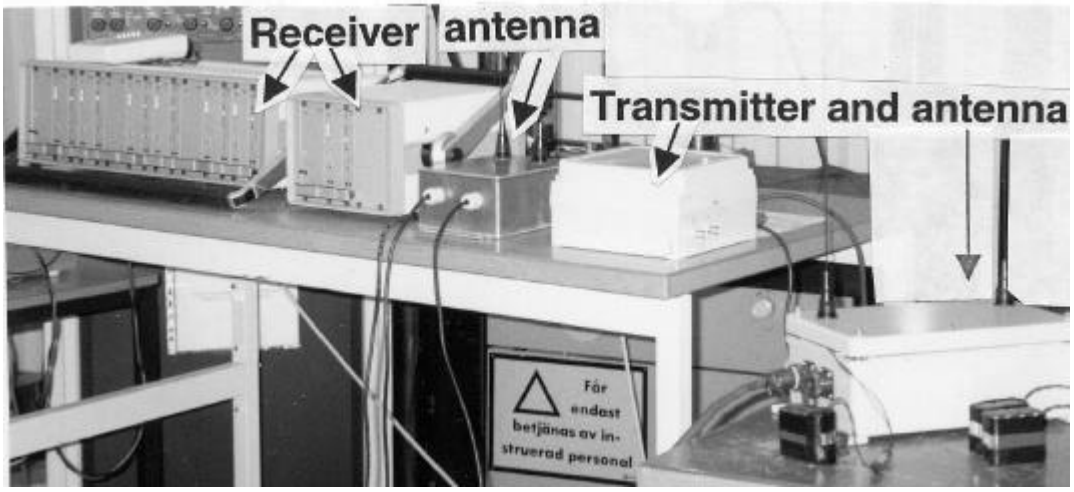

Figure 2-4. *Telemetry system.*

4. Data acquisition system. The system consisted of a computer and two receivers. The facilities were designed specifically for field use and to be able to stand field dust and humidity. They were housed in the control cabin of the boring machine. The software named Ochestrator was used for data acquisition.

2.3 Procedures for cutter force measurement

To fulfil the task of field measurement, the following preparation work was done first:

- Strain gauge attachment. Three cutter shafts were brought to the laboratory at LTU. In the surface of each shaft, four slots through the axis of the shaft were cut to glue 8 strain gauges and to house the cable as well as relevant protection materials. Measures were taken to insulate the gauges from oil, moisture, and dust by using special glue that could work at high temperature. The protection and fixing of the conducting cables and the connection with the transmitter were designed according to the structure of the boring machine.

- Load calibration. The cutter force signals from the attached strain gauges must be calibrated in the laboratory. However, first we have to know if the strains induced by the cutter forces are large enough to measure. Secondly we need to know if there exist some coupling phenomena in the measurement of the three forces before the laboratory calibration. If no coupling phenomena occur, the calibration will be simple and easy. In other words, we only need to establish the relationship between each cutter force and its respective strain independently. Otherwise, if coupling phenomena appear, we have to use three-direction loading simultaneously in the calibration. According to stress analysis by means of materials mechanics theory, if the shaft was long enough to be taken as a long beam, points A to F on the shaft only have one directional non-zero force or strain, and the other two directional forces are zero. As a result, there should be no coupling phenomena. However, it should be pointed out that the shaft of the cutter in the boring machine is quite short. The ratio between the length of the shaft and its diameter is not large enough

to satisfy the requirements for a long beam. Therefore, it is necessary to use the finite element method to perform the stress analysis of the cutter body, so as to estimate the amplitude of the strains to be measured and try to check the possible coupling phenomena.

2.4 Numerical analysis of stresses in the cutter body

In order to predict the maximum strains or stresses (on the shaft) and try to check the possible coupling phenomena induced by the normal force, tangential force and side force, we used a FEM (finite element method) code, ABAQUS, to calculate the stresses and strains in the cutter body. The code ABAQUS has a great potential for modelling the problems connected with complicated structures. In such cases, a conventional materials mechanics analysis method is usually difficult to apply.

2.4.1 Numerical model of cutter body

In this study, a numerical model of the whole cutter body was employed to calculate the stresses and strains in the body. However, some simplifications were made so that reasonable results could be obtained in the limited time and at a limited cost.

The cutter body is composed of three parts: the shaft, cutter, and saddle. During rock boring, the cutter rotates around the shaft, while the shaft is fixed on the saddle at its two ends. The bottom of the saddle is welded on the cutter head of the boring machine. The real geometrical structure of the cutter body is quite complicated. We have to simplify the real structure so that we will obtain a relatively satisfactory result at a limited cost. The simplified cutter body is shown in Figure 2-5. In this numerical model, the shaft and saddle are completely fixed together. This is slightly different from their original contact condition, but we think that the difference can be ignored. Similarly, the shaft and cutter are also completely fixed to each other. This is quite different from the real conditions, i.e. in original situations the cutter rotates around the shaft, while the cutter is cutting rock. Naturally, there exists some friction between the cutter and shaft during rock cutting. However, a numerical analysis considering the friction would be complicated and highly costly. Therefore, a model that did not consider the friction was used to calculate the stresses and strains in the cutter body.

During rock boring, there is a resultant force acting on one or a few buttons in the button cutter. The resultant force is composed of three directional forces: the normal force F_N, the tangential force F_T and the side force F_L. Because the loading area is far from the shaft, the three forces can be simplified into three linearly distributed loads. This simplification will more or less result in some differences between the real stresses or strains and the calculated stresses or strains of the cutter, but we think that such differences should be small and can be neglected.

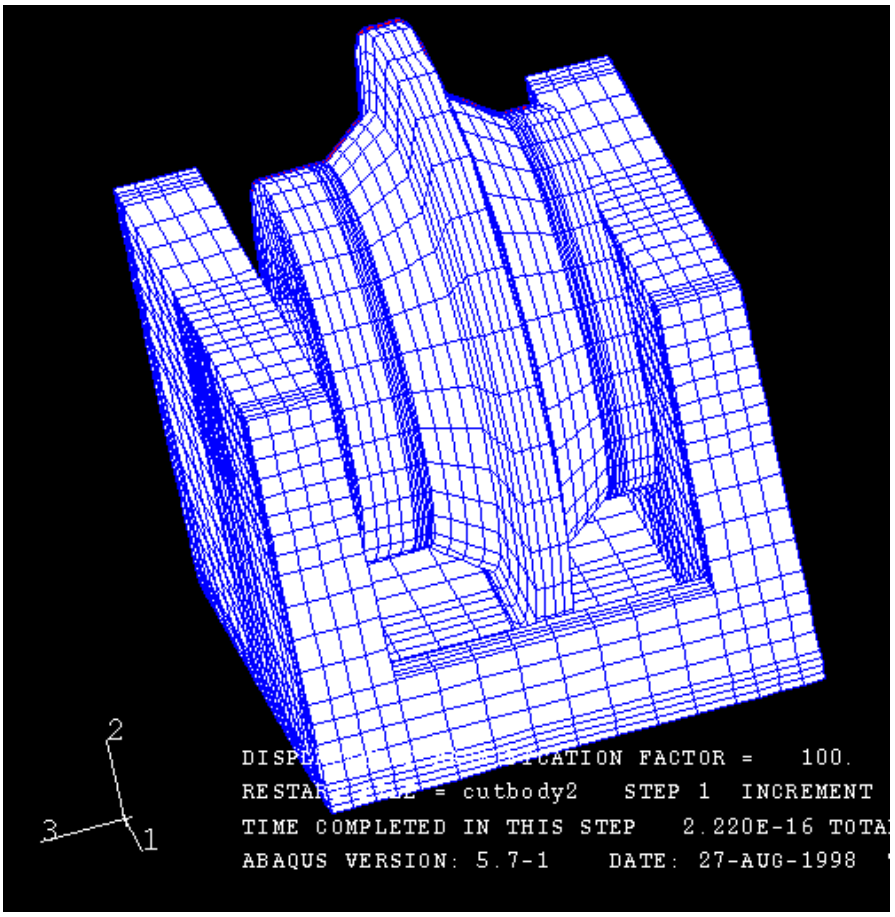

Figure 2-5. *Simplified cutter body.*

2.4.2 Results of numerical calculation

The loading and deformation of the cutter body in field excavation should be in an elastic state. Therefore, the elastic analysis method of the ABAQUS program was applied to the numerical model of the cutter body shown in Figure 2-5. In addition, the whole process of analysing the stresses or strains of the cutter body was divided into three independent stages:

- Normal force F_N=100kN. Figure 2-6 shows the distribution of the normal stresses along the axial direction of the shaft as the normal force F_N=100 kN acts on the cutter. The figure indicates that on the top and at the bottom of the whole shaft, the normal stresses are compressive and tensile, respectively. However, two critical cross-sections are located at two positions between the shaft and the saddle, instead of in the middle section of the shaft. The maximum compressive stress and maximum tensile stress are equal to 44.6 MPa and 35.7 MPa, respectively. And the respective maximum compressive strain and maximum tensile strain are 192 με (blue) and 156 με (red), respectively.

- Tangential force F_T=45 kN. When a tangential force is applied on the cutter, the relevant compressive stress and tensile stress are located on the two sides of the shaft, and the maximum compressive stress and maximum tensile stress are 18.7 MPa and19.2 MPa, respectively. Although the maximum compressive and tensile

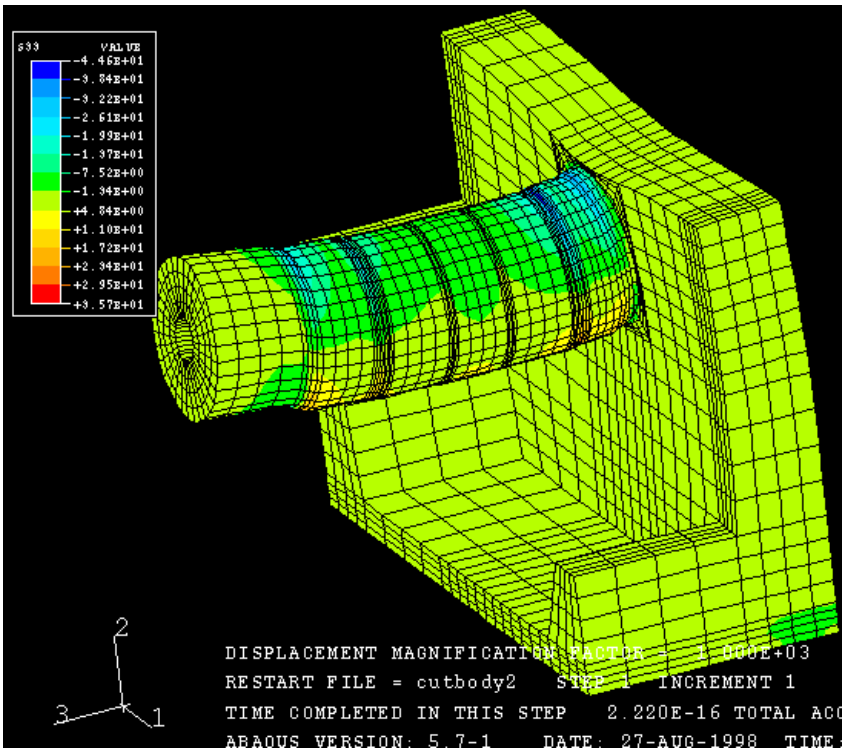

Figure 2-6. *Normal stress along the axis of the shaft.*

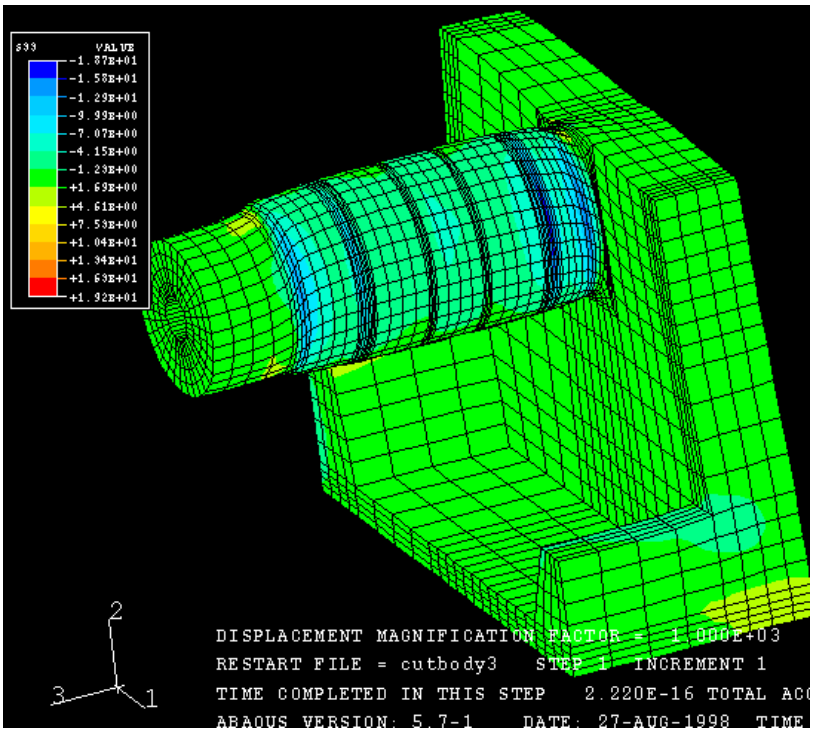

Figure 2-7. *Normal stress induced by F_T along the axis of the shaft.*

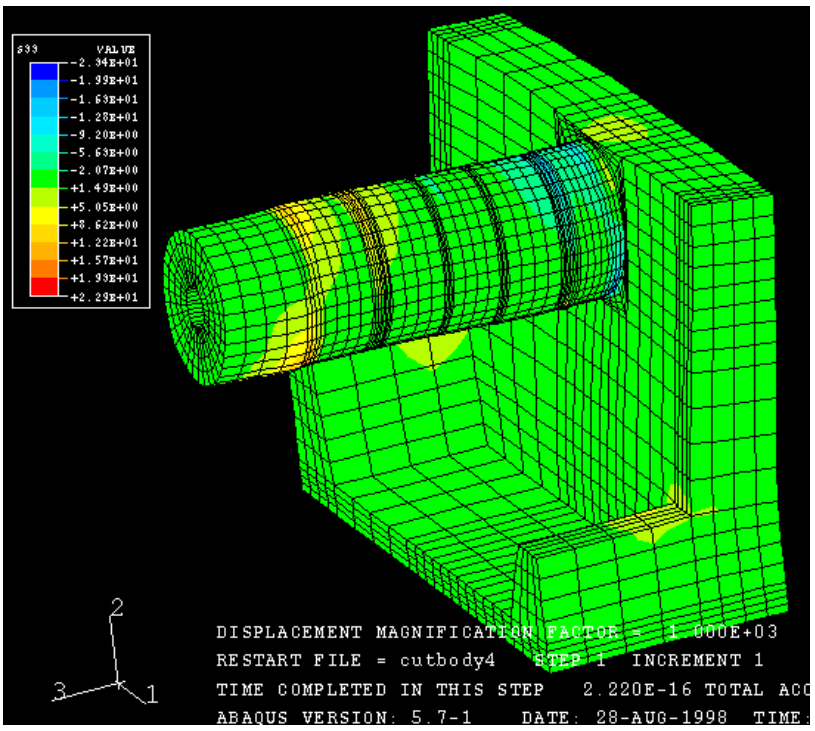

Figure 2-8. *Normal stress induced by F_L along the axis of the shaft.*

stresses are located near the two ends of the shaft, on the two sides of the middle section of the shaft, the normal stresses are quite large. From Figure 2-7 we can see the blue part in the middle section. The relevant maximum compressive strain and maximum tensile strain are equal to 82.8 με and 84.9 με, respectively.

- Side force F_L=45 kN. The distribution of the normal stresses induced by F_L is shown in Figure 2-8. The maximum compressive stress is 29.4 MPa. The maximum tensile stress is 22.9 MPa.

2.4.3 Concluding remarks

- The above calculated results show that when the normal force F_N=100 kN, the maximum compressive strain is located on the top of the shaft and is equal to 192 με, and the maximum tensile strain is on the bottom of the shaft and is equal to 156 με. According to the experience of strain measurements, such maximum strains are large enough to be measured. However, the positions of the maximum strains are in two cross-sections between the shaft and the saddle, rather than in the middle section of the shaft. This is mainly caused by the fact that in numerical calculation the shaft and the cutter are completely fixed to each other, i.e. the cutter cannot rotate around the shaft. This is quite different from the real support condition.
- When the tangential force F_T=45 kN, the numerical calculation shows that the maximum strains on the shaft are located on the two lateral surfaces and the maximum compressive and tensile strains are 82.8 με and 84.9 με, respectively. Similarly to the above, such strains should be measurable in the field in general conditions.

- When the side force F_L=45 kN, the maximum tensile stress and maximum compressive stress along the shaft top are located on the left and right, respectively. This result is consistent with the analysis using the materials mechanics method.

We are not sure if there is a force-coupling phenomenon in the loading process of the cutter body according to the above numerical analysis, mainly because the numerical analysis is based on a simple model that does not consider the friction between the cutter and the shaft. Consequently, the results are not adequate for answering such a question. To achieve success in cutter-force measurements, we have to consider the possibility of force coupling and employ a laboratory calibration system that can realise three-direction loading simultaneously, so that the possible force-coupling problem may be solved by means of this calibration.

3 Laboratory calibration

The aim of the laboratory calibration is to establish the relationships between the cutter forces and strains (or voltages) recorded by means of the strain gauges on the cutter shaft. To achieve this aim, we first have to know if the force-coupling phenomenon mentioned above exists. The force-coupling phenomenon means that a strain value from one of the three groups of strain gauges on the shaft is actually related to all the three directional forces rather than only one of them. If no such force-coupling phenomenon were to exist, the laboratory calibration would be very easy. In other words, we would only need to apply the three cutter forces independently in laboratory calibration, and then establish the relationship between each cutter force and its respective strain or voltage. Otherwise, if the force-coupling phenomenon is considerable or cannot be neglected, we must consider the force-coupling phenomenon and solve this problem through laboratory calibration.

As described in Chapter 2, we cannot exclude the possibility that a force-coupling phenomenon may occur in field tests. Therefore, in order to obtain correct measurement results in field tests, we have to consider the force-coupling problem.

3.1 Calibration equation

Assuming that the influence of the force-coupling phenomenon is linear, then we have

$$\left.\begin{aligned} V_{FN} &= a_1 F_N + a_2 F_T + a_3 F_L \\ V_{FT} &= a_4 F_N + a_5 F_T + a_6 F_L \\ V_{FL} &= a_7 F_N + a_8 F_T + a_9 F_L \end{aligned}\right\} \qquad (3\text{-}1)$$

Here V_{FN}, V_{FT} and V_{FL} are the voltages measured from the strain gauges A/B (for normal force), C/D (for tangential force) and E/F (for side force), respectively. F_N, F_T and F_L are the normal force, tangential force and side force, respectively. In the laboratory calibration, F_N, F_T and F_L are applied by a testing machine named Instron and two hydro-cylinders, respectively, see Figure 3-1. The hydro-cylinder for F_L is at the back of the cutter in Figure 3-1. The aim of the laboratory calibration is actually to determine α_1, $\alpha_2 \ldots \alpha_9$. Then we can use equation (3-1) to calculate F_N, F_T and F_L by means of the V_{FN}, V_{FT} and V_{FL} measured in the field.

As $F_T = F_L = 0$, according to (3-1) we have

$$\left.\begin{aligned} a_1 &= V_{FN} / F_N \\ a_4 &= V_{FT} / F_N \\ a_7 &= V_{FL} / F_N \end{aligned}\right\} \qquad (3\text{-}2)$$

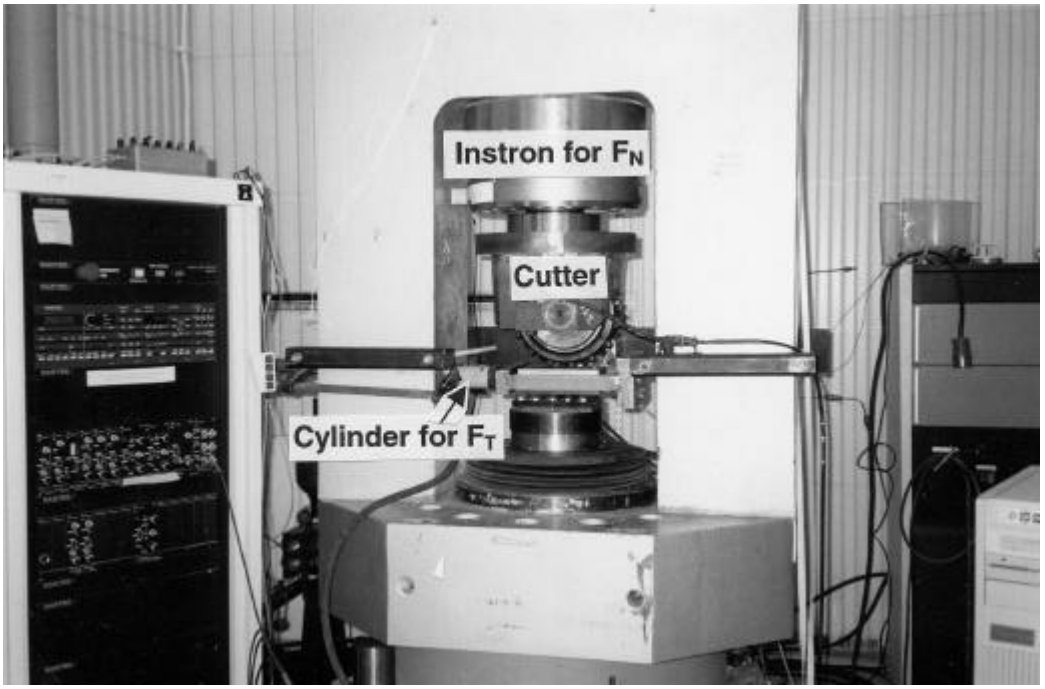

Figure 3-1. *Three cutter forces applied in laboratory calibration.*

As $F_T = F_N = 0$, according to (3-1) we have

$$\left.\begin{aligned} a_3 &= V_{FN} / F_L \\ a_6 &= V_{FT} / F_L \\ a_9 &= V_{FL} / F_L \end{aligned}\right\} \tag{3-3}$$

Because we cannot only apply F_T to the shaft (in the cutter body) without the normal force in the laboratory, we have to choose F_N= constant ≠0 and F_L=0. Thus from (3-1) we obtain

$$\left.\begin{aligned} a_2 &= (V_{FN} - a_1 F_N) / F_T \\ a_5 &= (V_{FT} - a_4 F_N) / F_T \\ a_8 &= (V_{FL} - a_7 F_N) / F_T \end{aligned}\right\} \tag{3-4}$$

According to the description above, for one cutter body we can perform three kinds of laboratory calibrations as listed above. Then we can determine $\alpha_1, \alpha_2 \ldots \alpha_9$.

3.2 Determination of the coefficients a_1, a_2–a_9 for the front cutter (cutter 3)

The determination of the coefficients α_1– α_9 for cutter 3 is in detail described in Appendix A. Here the result for the values of the coefficients is only shown in the following.

$$\left.\begin{aligned} a_1 &= 0.0197 \\ a_2 &= 0.0127 \\ a_3 &= -0.0176 \\ a_4 &= -0.0004 \\ a_5 &= -0.1011 \\ a_6 &= -0.0007 \\ a_7 &= 0.0054 \\ a_8 &= -0.0131 \\ a_9 &= -0.0263 \end{aligned}\right\} \qquad (3\text{-}5)$$

3.3 Determination of equations for calculating cutter forces

According to equation (3-1), we have

$$\Delta = \begin{vmatrix} a_1 & a_2 & a_3 \\ a_4 & a_5 & a_6 \\ a_7 & a_8 & a_9 \end{vmatrix}$$

(3-6a)

$$F_N = (1/\Delta) \begin{vmatrix} V_{FN} & a_2 & a_3 \\ V_{FT} & a_5 & a_6 \\ V_{FL} & a_8 & a_9 \end{vmatrix} \qquad (3\text{-}6b)$$

$$F_T = (1/\Delta) \begin{vmatrix} a_1 & V_{FN} & a_3 \\ a_4 & V_{FT} & a_6 \\ a_7 & V_{FL} & a_9 \end{vmatrix} \qquad (3\text{-}6c)$$

$$F_L = (1/\Delta) \begin{vmatrix} a_1 & a_2 & V_{FN} \\ a_4 & a_5 & V_{FT} \\ a_7 & a_8 & V_{FL} \end{vmatrix} \qquad (3\text{-}6d)$$

For cutter 3, applying the values of the coefficients α_1–α_9 in equation (3-5) to (3-6), we can obtain

$\Delta=3.916\times10^{-5}$
$1/\Delta=2.5536\times10^{4}$

$$\left.\begin{aligned} F_N &= 67.66V_{FN} - 45.66V_{FL} + 14.42V_{FT} \\ F_T &= -0.37V_{FN} + 0.53V_{FL} - 10.8V_{FT} \\ F_L &= 14.07V_{FN} - 50.73V_{FL} + 8.3V_{FT} \end{aligned}\right\} \quad (3\text{-}7)$$

3.4 Modification of equations for front cutter

The three forces calculated by equation (3-7) would have some errors compared with their respective real forces, particularly because of the determination of the coefficient α_8. Such errors can be seen in Figure B-1 and B-2 in Appendix B. Therefore, equation (3-7) needs to be modified according to the laboratory calibration tests. Two laboratory tests numbered CUT3N14 and CUT3N18 were used for the modification. The modified result is shown in equation (3-8), and the detailed modification is described in Appendix B.

$$\left.\begin{aligned} F_N^* &= 55.34V_{FN} - 16.58V_{FL} + 2.47V_{FT} \\ F_T^* &= 1.02V_{FN} - 4.56V_{FL} - 11.35V_{FT} \\ F_L^* &= 10.9V_{FN} - 40.76V_{FL} - 13.54V_{FT} \end{aligned}\right\} \quad (3\text{-}8)$$

Here the modified cutter forces F_N^*, F_T^*, and F_L^* are in fact the calculated forces shown in Figure 3-2. The comparison between the forces calculated by equation (3-8) and the real forces is shown in Figure 3-2. Equation (3-8) will be used to determine the true cutter forces in field tests according to the data for V_{FN}, V_{FL} and V_{FT} measured in the field. In order to confirm the feasibility of the above modification, equation (3-8) is applied to other calibration tests listed in Table A-2 in Appendix A. The results indicate that the differences between the calculated normal and tangential forces and the real normal and tangential forces are usually within 16% for repeat loading and 18% for one-time loading, while the calculated side force is sometimes much larger than the real side force by 100% under both one-time loading and repeat loading, particularly as all the three directional cutter forces reach their maximum values.

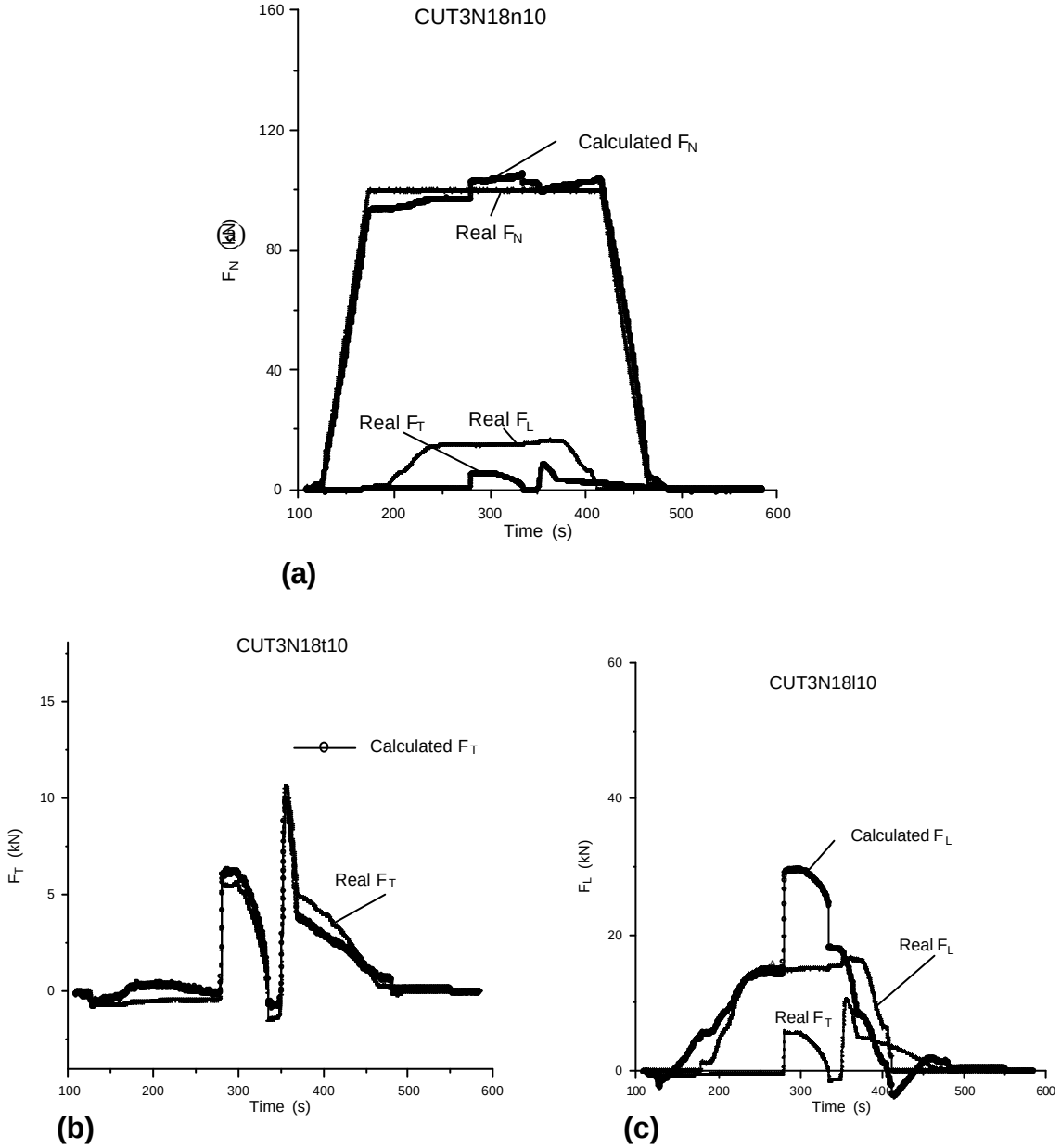

Figure 3-2. *Final calculated forces and real forces.*

3.5 Final equation for gauge cutter (cutter 2)

Similarly, we can obtain all the values of α_1–α_9 for the gauge cutter (cutter 2). The data for all the calibration tests are listed in Table C-1 and C-2 in Appendix C.

The values of α_1–α_9 for cutter 2 is in the following.

$$\left.\begin{aligned} a_1 &= 0.018 \\ a_2 &= 0.0115 \\ a_3 &= -0.0141 \\ a_4 &= -0.0007 \\ a_5 &= -0.0916 \\ a_6 &= -0.0036 \\ a_7 &= 0.0056 \\ a_8 &= -0.0112 \\ a_9 &= -0.0201 \end{aligned}\right\} \qquad (3\text{-}9)$$

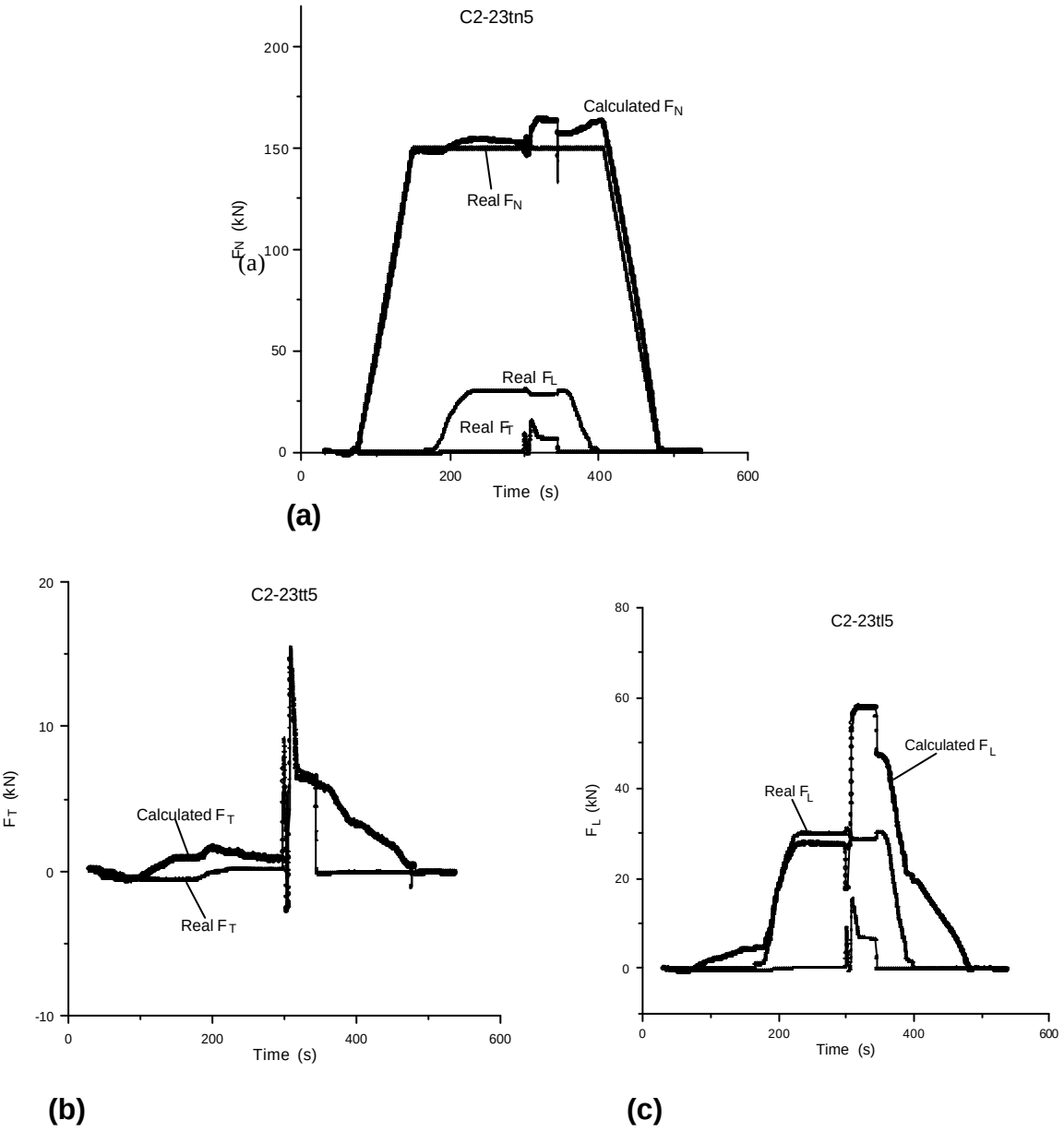

Figure 3-3. *Calculated forces and real forces for CUT2N23.*

Using similar methods to those used in the treatment of the front cutter (cutter 3), we obtain the following final equation for the gauge cutter.

$$\left.\begin{aligned} F_N^{\ *} &= 59.02V_{FN} - 17.77V_{FL} + 4.17V_{FT} \\ F_T^{\ *} &= 0.77V_{FN} - 1.61V_{FL} - 11.99V_{FT} \\ F_L^{\ *} &= 18.83V_{FN} - 49.93V_{FL} - 0.59V_{FT} \end{aligned}\right\} \qquad (3\text{-}10)$$

The curves determined by equation (3-10) for CUT2N23 are shown in Figure 3-3.

Similarly, equation (3-10) is applied to the other calibration tests listed in Table C-2. The result is similar to that for cutter 3, i.e. the differences between the calculated normal and tangential forces and the real normal and tangential forces are usually within 15% for repeat loading and 23% for one-time loading. However, the calculated side force and the real side force sometimes have a big difference. Particularly as the tangential force reaches its maximum peak value, the calculated side force is sometimes larger than the real side force by 100%.

All in all, the modification treatment described above is proved apt for all the laboratory tests performed in this study. Therefore, the calibration results should be valid and reliable for all the field measurements of both cutters. However, it must be pointed out that the side force measured in the field is probably quite larger than the real side force, and this is particularly true of the maximum peak side forces.

4 Field testing results for cutter forces

4.1 Testing system

The whole testing system in the field is shown in Figure 4-1. After finishing the laboratory calibration, we installed the two cutters on the boring machine. The two cutters were put at the front and outermost positions of the cutter head, respectively. We also call them the front cutter and the gauge cutter respectively. Then we put a transmitter on the cutter head. The transmitter and the strain gauges were connected with cables numbered 3 in the figure. In addition, the antenna of the receiver shown in the figure was installed on the stationary part of the machine. A cable from the antenna was connected to the receiver, and then the receiver was connected to a computer in a cabin near the borehole in the field. In this testing method the signal transmission is carried out by the telemetry system, consisting of the transmitter and the receiver.

The field tests started from field function tests at the Äspö underground site. The function tests were successful. All the field tests were performed in only one borehole, numbered “2”. Another borehole numbered “1”, neighbouring on borehole 2, had first been finished by the same machine. The cutter head of the boring machine had a total of 20 cutters. Borehole 1 was bored by using all the disc cutters, but borehole 2 had been bored by using 16 button cutters and 4 disc cutters.

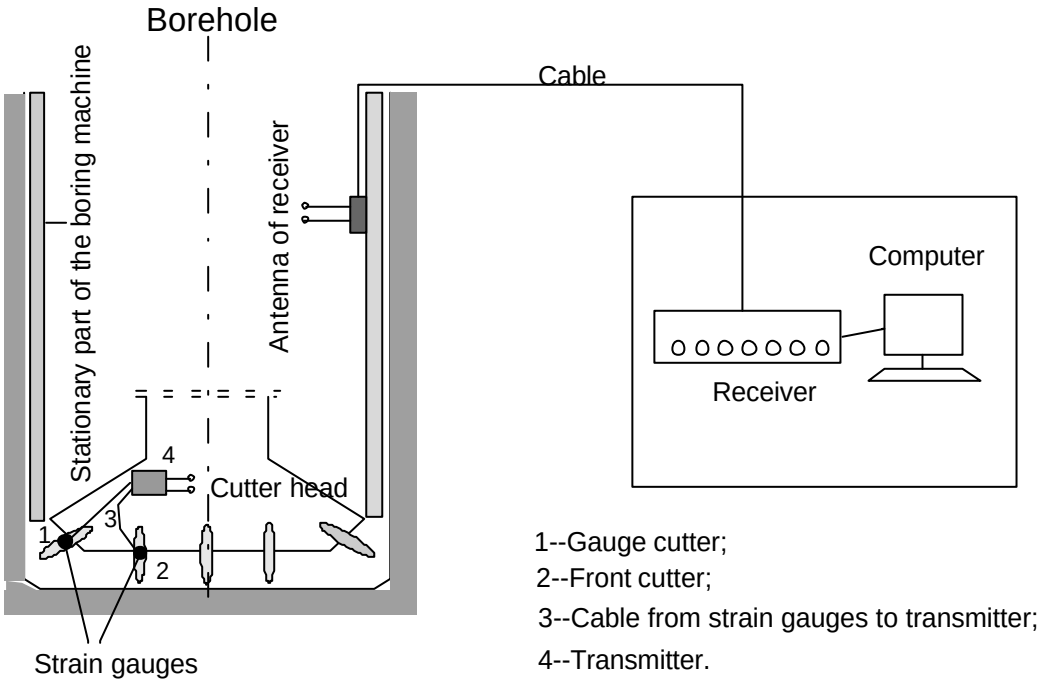

Figure 4-1. *Field testing system.*

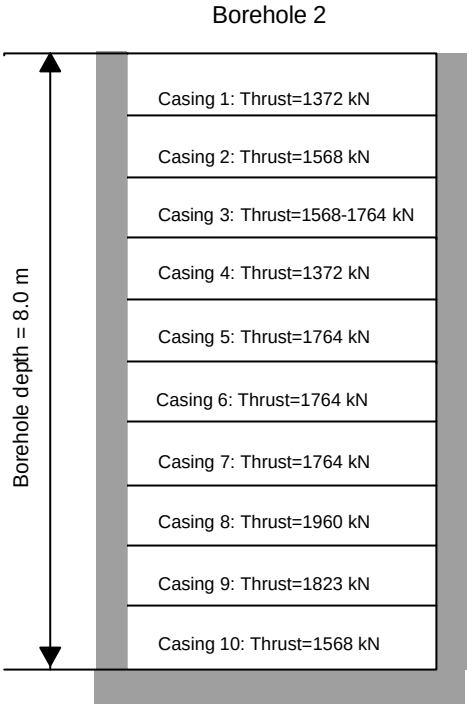

Figure 4-2. *Borehole 2 and its casings.*

Borehole 2 was divided into 10 casings along its depth, see Figure 4-2. The depth of each casing is equal to 0.8 m. The rotation speed of the machine was 15 rpm in casing 2, and 10 rpm in the other 9 casings. The thrust of the machine was changed in the different casings.

According to previous experience, the main energy components corresponding to the cutter forces lie in the range of signal frequency 0–10 Hz /Samuel and Seow, 1984/. Therefore, we chose 100 Hz as the sampling frequency in the field tests. In order to correlate the recorded force signals with the rock damage in the rock samples core-drilled from the walls of the borehole, the positions of the measured cutter at each specific time were co-ordinated.

4.2 Results of cutter force measurements

When boring the first three casings of borehole 2, the force signals from the front cutter were not stable, probably because the relevant gauges' contact with the shaft was not good. In addition, the temperature signals from the same cutter suddenly became abnormal during the boring of the first casing. The reason was possibly the same as the reason for the abnormal force signals just mentioned above. While the boring of the third casing was performed, a motor of the boring machine had a breakdown. Consequently, we did not obtain good results from the first three casings.

From casing 4 to casing 10, all the signals for every individual force or temperature were very good. Here we only show some measured results from casing 10. Figure 4-3a–f indicates the measured forces of both the front cutter (in the machine this cutter is numbered "10") and the gauge cutter (numbered "18A") within the first 7 minutes

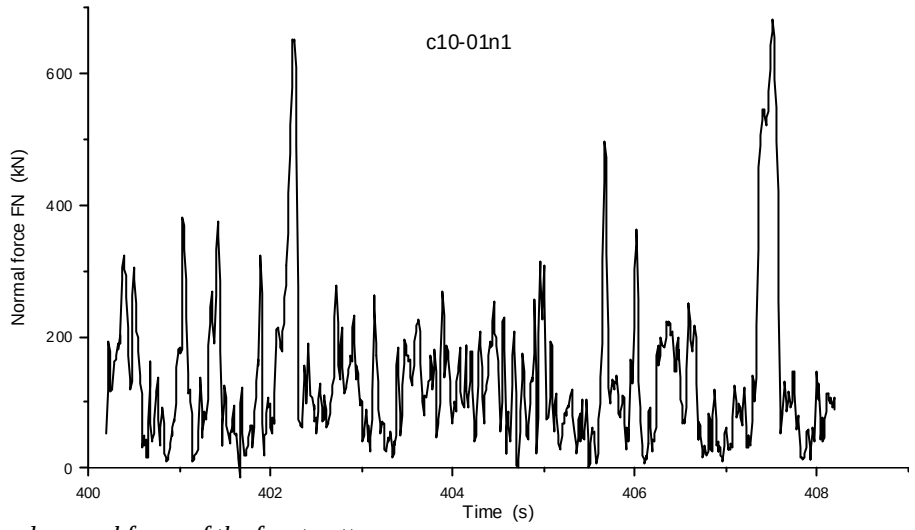

(a) *Measured normal force of the front cutter.*

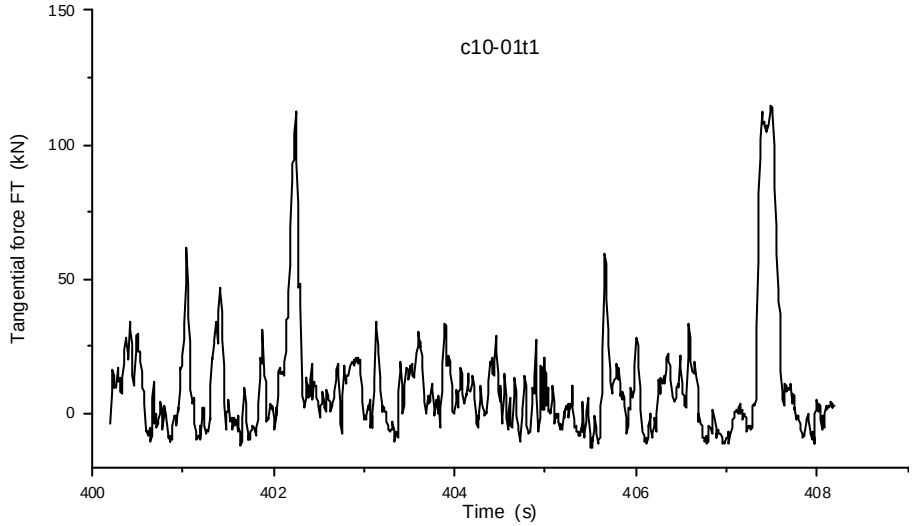

(b) *Measured tangential force of the front cutter.*

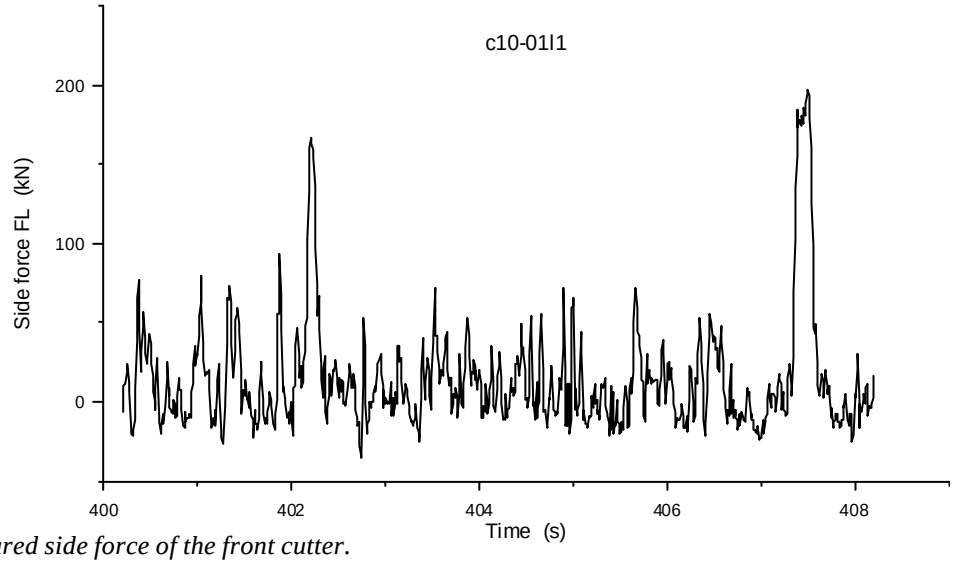

(c) *Measured side force of the front cutter.*

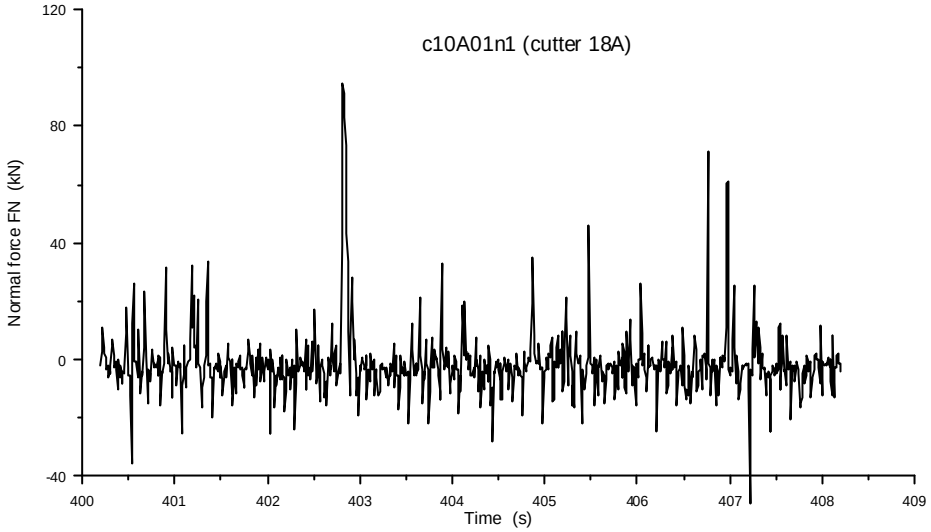

(d) *Measured normal force of the gauge cutter.*

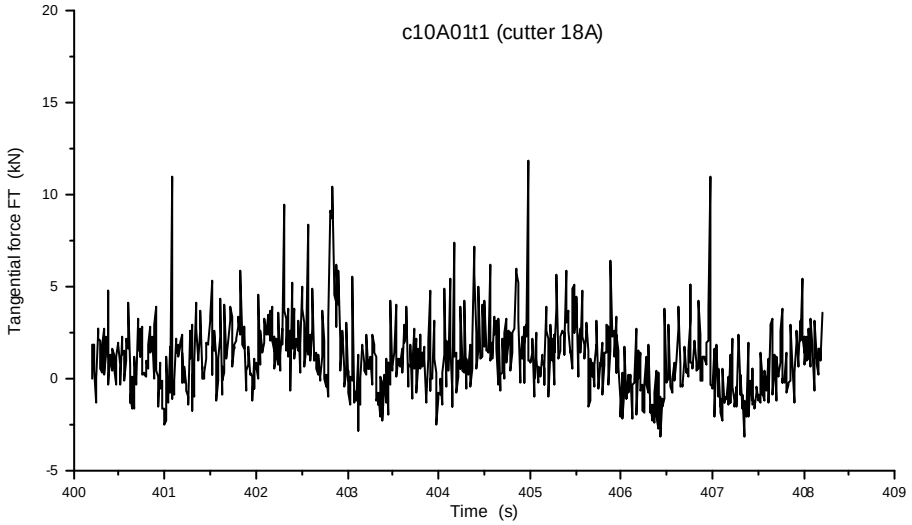

(e) *Measured tangential force of the gauge cutter.*

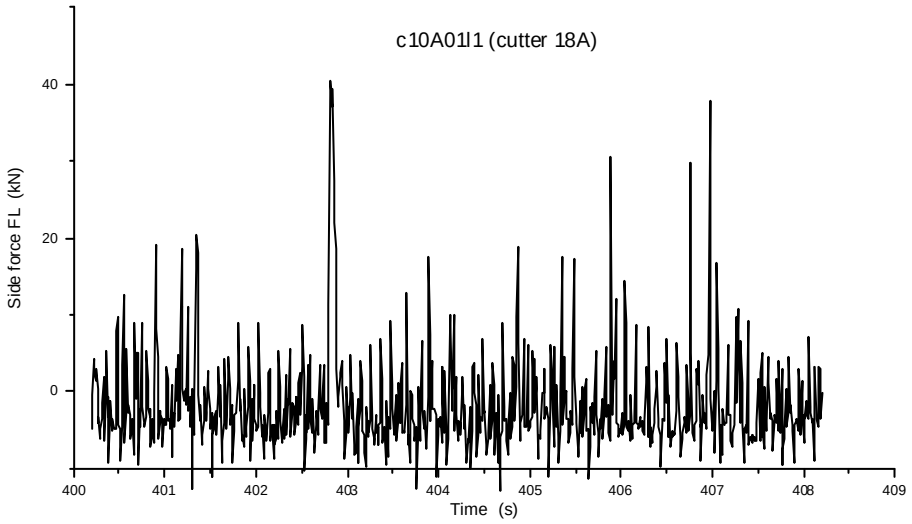

(f) *Measured side force of the gauge cutter.*

Figure 4-3a–f. *Measured cutter forces.*

of excavation in casing 10. From Figure 4-3 the following two conclusions can be drawn. (1) The maximum cutter forces, i.e. the normal force, tangential force and side force, of the front cutter are much larger than the maximum cutter forces of the gauge cutter. The chief reason for these results is that the gauge cutter during most of boring time goes into the position where another gauge cutter located on its nearest periphery on the cutter head has produced rock breakage earlier. One further explanation may be that the distance between the two gauge cutters in the diameter direction of the cutter head is only 16 mm. Obviously, rock boring is quite different from metal cutting. It is possible for the sizes of rock chips caused by a cutter to reach 16 mm. Concerning rock breakage, the gauge cutter whose forces we measured does not play a significant role. (2) The maximum normal, tangential and side forces of the front cutter appear once every 5–7 seconds. On the one hand, this result shows that the force-coupling phenomenon is strong. On the other hand, the result indicates that the maximum normal force, tangential force and side force are quite larger than the average normal force, tangential force and side force. Such a big difference between the maximum force and the average one is unreasonable from the viewpoint of rock boring. In other words, a very high cutter force is unnecessary to rock boring. (3) Each peak of the normal forces, except for the negative ones, means a whole penetration process of one button. Here we assume that only one button contacts rock when the peak of the normal force is reached. In the process, the button is loaded from a low level to the maximum level, i.e. the peak value. When the peak normal force is reached, the rock beneath the button is broken and the button as well as the cutter in question is unloaded. At the same time, the normal force decreases. According to Figure 4-3a, the smallest normal force peak is about 60 kN. This indicates that only when the normal force is equal to or greater than 60 kN, can the rock be broken by the button.

However, Figure 4-3 only shows the cutter forces measured during 8 seconds of the boring of the machine. This is not long enough to find the basic characteristics of the force signals. Therefore, it is necessary to perform spectral analysis of the force signals by means of fast Fourier transforms.

4.3 Spectral analysis for cutter forces

The MATLAB program was employed to perform the spectral analysis. Figure 4-4 shows the results of the spectral analysis for both the front cutter and the gauge cutter during the first 7 minutes of boring in casing 10. From Figure 4-4 we can find the maximum, minimum and mean normal force (or tangential force or side force) of both the front cutter and the gauge cutter during the first 7 minutes of boring. The results indicate that the maximum, minimum and mean normal forces of the front cutter are 684, -43 and 120 kN, respectively. However, the maximum, minimum and mean normal forces of the gauge cutter in the same period are 104, -69 and –1.2 kN, respectively. It is clear that the maximum normal force of the front cutter is much larger than that of the gauge cutter. The tangential force and side force of both cutters show similar results. The chief reason for these results has been analysed above.

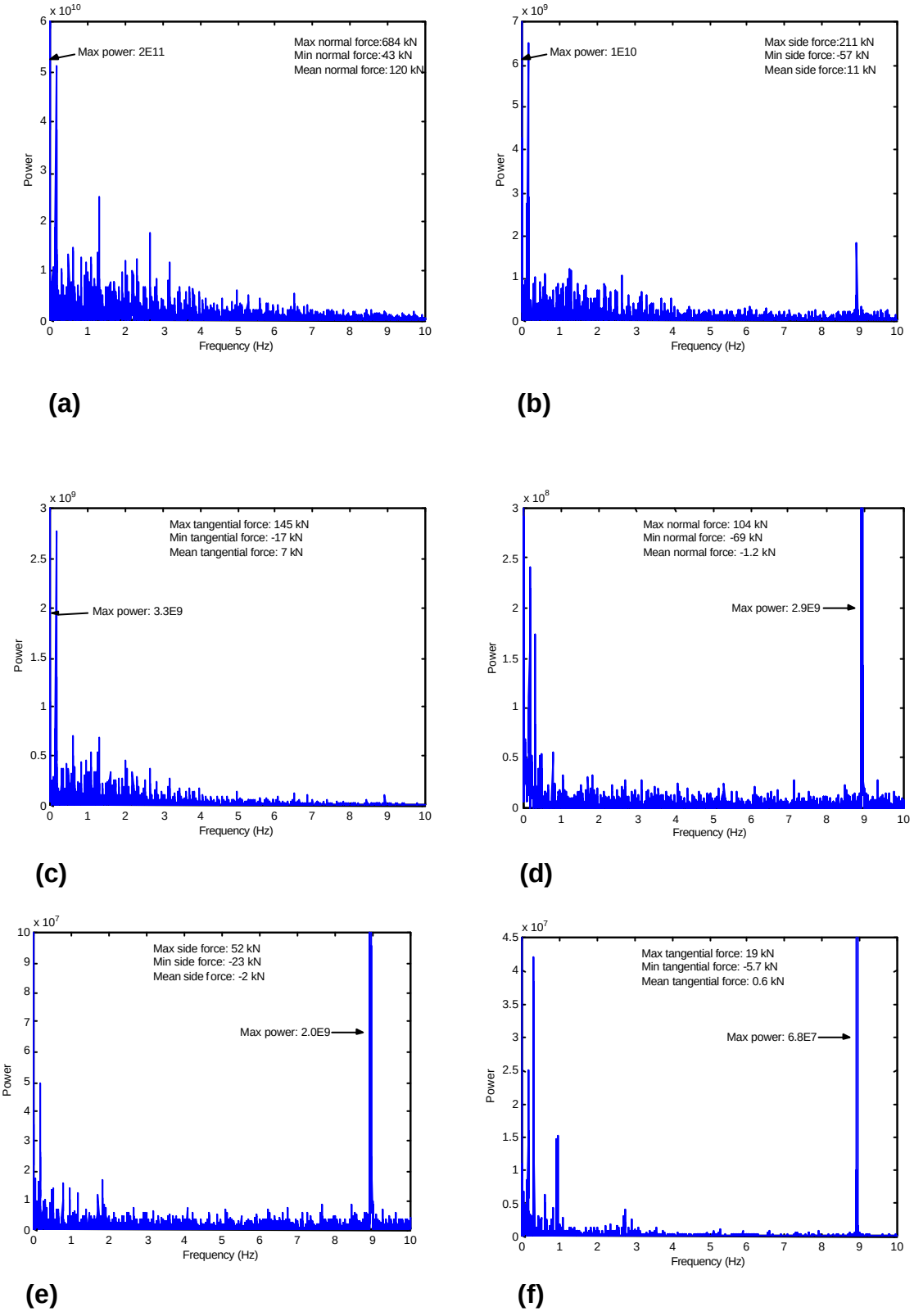

Figure 4-4. *Power and frequency for cutter forces in Casing 10 (first 7 minutes of boring). (a) Normal force of the front cutter. (b) Side force of the front cutter. (c) Tangential force of the front cutter. (d) Normal force of the gauge cutter. (e) Side force of the gauge cutter. (f) Tangential force of the gauge cutter.*

From Figure 4-4 we can make the following conclusions

- For the front cutter, the main energy components lie in the range 0–5 Hz.
- For the gauge cutter, the main energy components lie in the range 0–10 Hz, because a high level of power appears at the frequency f ≈ 9 Hz. In addition, corresponding to f ≈ 9 Hz, a relatively high level of power occurs in the power spectra plot for the side force of the front cutter, see Figure 4-4b.
- According to Figure 4-4a-c, as f ≈ 0.15 Hz, the second highest levels of power relevant to F_N, F_T, and F_L occur. The F_N, F_T, and F_L corresponding to f ≈ 0.15 Hz should be the two peak values in Figure 4-3a, 4-3b, and 4-3c, respectively. This is because the peak forces appear in the period T = 5–7 seconds. Under such peak cutter forces, the rock beneath the cutter should definitely be broken.

Figure 4-5a indicates that most of the normal force is concentrated in the region of F_N=0–100 kN. As described above, when $F_N \geq 60$ kN, the rock beneath the cutter can be broken, so that we can conclude that the distribution of the normal force in the figure is not so good for rock boring. In other words, there would be a good distribution of the normal force if most of the normal force were larger than 60 kN, which can be considered as a critical force for rock breakage by the cutter in the condition of this study. In the case of Figure 4-5a, the distribution curve should be moved from left to right.

For the boring machine, as well as its cutters, the side force had better be zero. The reason can be explained as follows. A large horizontal force is possibly formed by the side forces from each cutter and then applied to the machine. This horizontal force makes the machine shake or move in the horizontal direction that is perpendicular to the axis of the borehole. Furthermore, such a horizontal force gives rise to an increase in the roughness of the wall of the borehole and even creates some grooves in the walls. Therefore, the side force should be reduced into as small a value as possible. Particularly, a large side force should be avoided. For example, the distribution curve for the side force in Figure 4-5b should be concentrated in the area around F_L=0 kN.

Similarly to the case of normal force in Figure 4-5a, the distribution of the tangential force is also unreasonable. A good result would involve the current distribution being moved into the right side of Figure 4-5c.

As described above, the cutter forces of gauge cutter 18A are much smaller than those of the front cutter. In other words, the gauge cutter does not play its role in rock fragmentation effectively. Similarly to the front cutter, the gauge cutter has an unreasonable distribution of the cutter forces too. A better distribution would involve the present distribution curves being moved to the right.

In conclusion, from Figure 4-4 we can find that the design of the cutters should be improved, because a large side force is caused during boring. Such a side force will probably give rise to a large horizontal force for the boring machine. This is not only harmful for the stability of the machine, but also bad for the smoothness of the walls of the borehole. In addition, from Figure 4-3 we note that the maximum cutter forces (or the forces close to the maximum values) periodically appear once every 5–7 seconds.

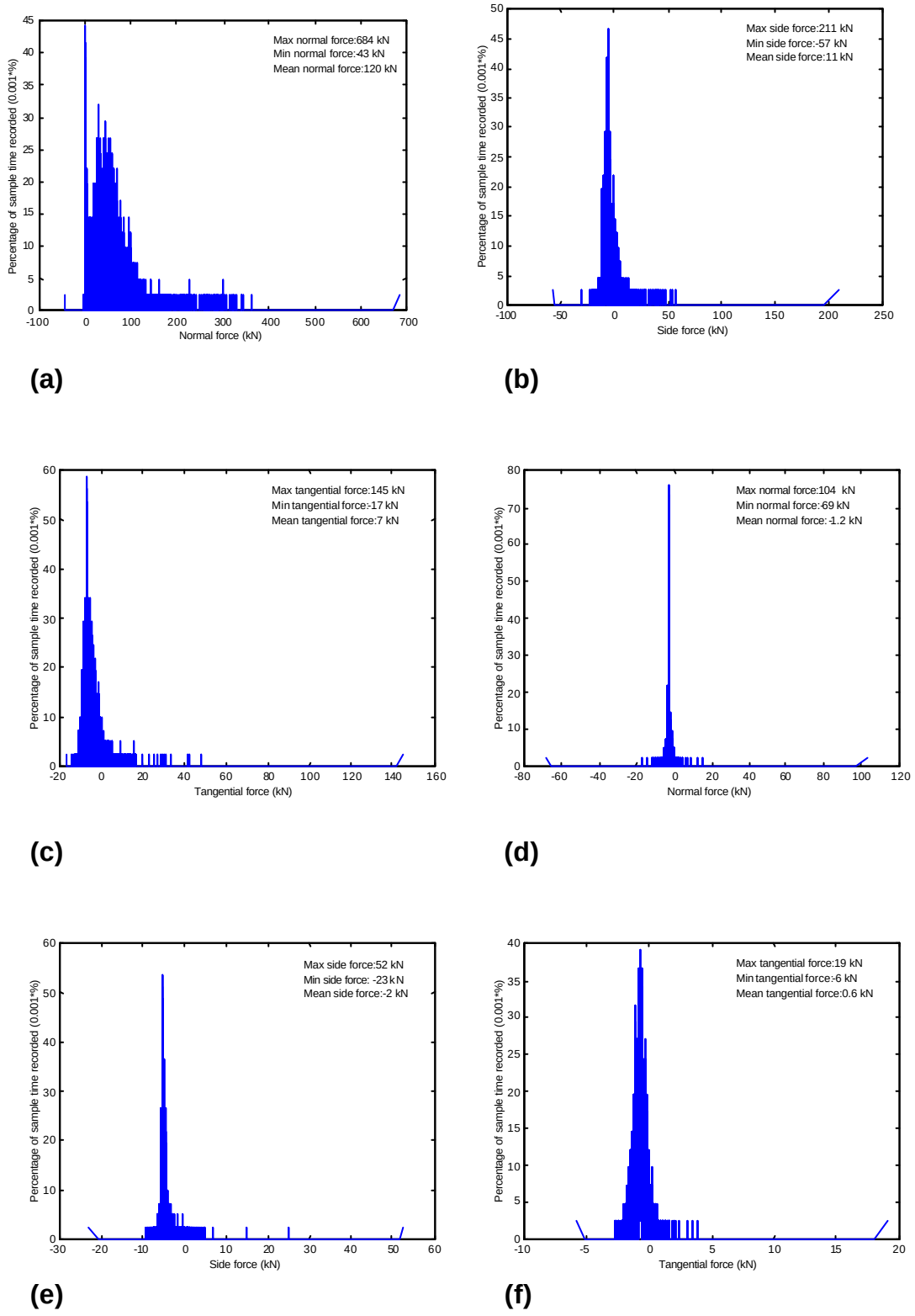

Figure 4-5. *Distribution of cutter forces in Casing 10 (first 7 minutes of boring). (a) Normal force of the front cutter. (b) Side force of the front cutter. (c) Tangential force of the front cutter. (d) Normal force of the gauge cutter. (e) Side force of the gauge cutter. (f) Tangential force of the gauge cutter. Percentage of sample time recorded = the number of times during sampling when an equal F_N occurs / the total sampling times (here the total sampling times = 40858).*

This is reflected in the part of the frequency < 0.2 Hz in Figure 4-4. It seems that rock boring does not mainly rely on the maximum forces, because cutter forces smaller than the maximum ones should be enough to break the rock beneath the cutter. For example, as 60 kN $<F_N<$400 kN, the cutter should be able to break the rock. If so, we should avoid such maximum cutter forces appearing in rock boring, because excessively high cutter forces are not good for the machine.

4.4 Analysis of boring machine parameters

In the field measurements, we recorded the thrust and torque of the machine and the rotation speed of the cutter head, and wrote down the average penetration rate of the machine during every 6 minutes of boring. The total thrust of the machine is supplied by four hydro-cylinders. Table 4-1 shows the recordings of the thrust and the penetration rates from 6 casings. The rotation speed, corresponding to the data in Table 4-1, of the cutter head is approximately 10 rpm. The relationship between the thrust and the penetration rate is drawn in Figure 4-6.

Table 4-1. Thrust and penetration rates of the machine.

Total thrust (kN)	**1372**	**1568**	**1764**	**1960**
Penetration rate (cm/hour)	36	45	60.5	69
Casing No.	4	10	5–7	8

Figure 4-6 indicates that the penetration rate of the machine increases with an increasing thrust of the machine in the case of a constant rotation speed of the cutter head. This implies that the cracks in rock produced by a cutter with a high normal force should be longer than those produced by a cutter with a low normal force. Therefore, in order to increase the rock excavation speed, we should increase the thrust of the boring machine. However, from the viewpoint of nuclear waste management, the thrust of the machine should not be too high, so as not to produce longer cracks in the bottom and wall of a borehole.

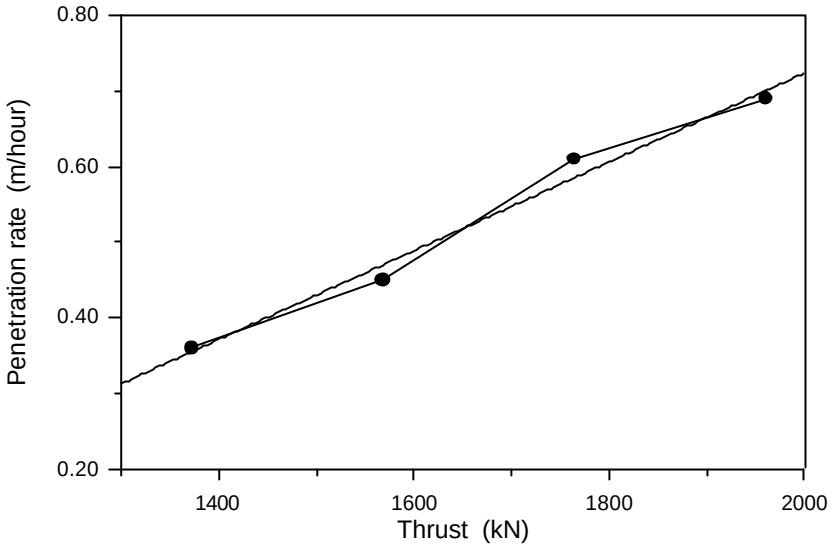

Figure 4-6. *Relationship between thrust and penetration rate of the machine.*

5 Measurements of cutter temperature

For a long time engineers have been concerned about the real temperature in the cutters of TBM machines or in the bits of percussive/rotary drilling machines during boring or drilling. High temperature will worsen the material properties of the cutters or bits, and in turn speed up their surface wear in the process of excavation or drilling. However, up to date we have not found any report that has presented in-situ temperature measurements of cutters or bits, or provided information on the real temperature of cutters or bits during boring or drilling. Therefore, it is interesting to measure the cutter temperature of the boring machine during field tests.

5.1 Method of temperature measurement

5.1.1 Transducer

We employed a special temperature gauge named ETG-50A/Option E, for measuring the temperature in one cutter of the boring machine. Two such gauges with the LST Matching Network LST-10C-350D were used.

The temperature gauges can work at temperatures of –150° to +260°C. Because the gauges usually work in tough field environments, the glue M-Bond 610 is used to bond them on the shaft. This glue is apt for dynamic stress analysis and can work at temperatures of –269° to +370°C. After the gauges were bonded on the surfaces of the shaft, a protection material (silicone rubber), 3145-RTV, was put on the gauges. This material can stand temperatures of –75° to +315°C. The gauges were placed at a position on the lowest surface of the cutter shaft, see Figure 5-1.

5.1.2 Bridge circuit

The temperature gauges were connected in the bridge shown in Figure 5-1. The circuit package was protected in a box and located in a proper place behind the cutter head.

5.1.3 Signal transmission

The telemetry method was employed and the system consisted of a transmitter, a receiver, and a power supply. For our purpose, the telemetry system is able to measure seven-channel signals (six for the cutter forces and one for the temperature). The transmitter is portable and can stand vibration, high temperature (up to +85°C) and high acceleration. It was installed at the back of the cutter head. The receiver antenna was positioned on the upper part of the boring machine and the receiver instrument was located at the control cabin for safety and easy coupling with the data acquisition system, see Figure 4-1.

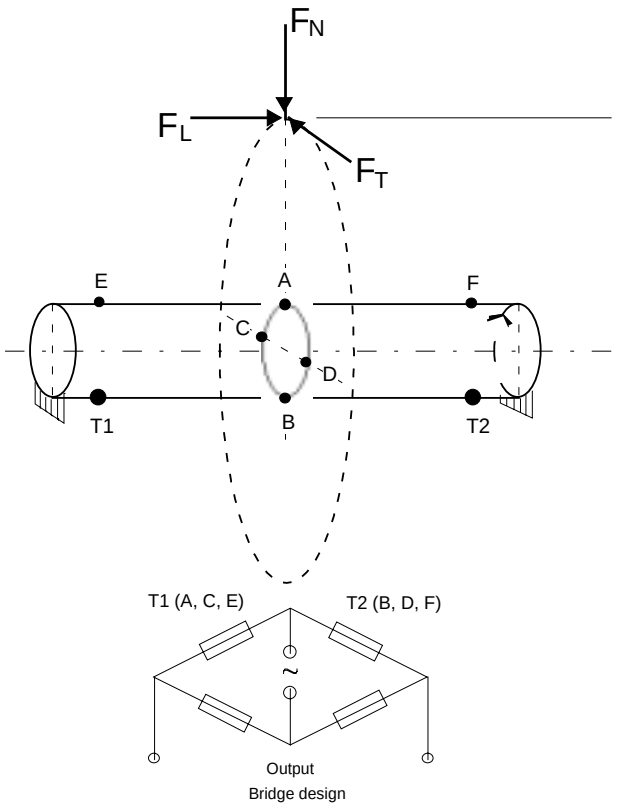

Figure 5-1. *Arrangement of temperature gauges T1 and T2 on the cutter shaft and bridge circuits.*

The data acquisition for the temperature measurements was carried out by the same data acquisition system as that used for the cutter force measurements described previously.

5.2 Laboratory calibration

Calibration was performed in the laboratory. The cutter body, together with a cable, was put into an oven, see Figure 5-2. The cable connected the cutter to the transmitter outside the oven. The telemetry system, consisting of the transmitter and the receiver, is connected to a computer. As the temperature in the cutter varies, the computer can record the data of both the voltages from the temperature gauges and the real temperature from the oven itself. Considering the safety of the cable, which can normally work at 90°C, 55°C was chosen to be the highest temperature in the laboratory calibration. The results of the calibration for the front cutter are shown in Figure 5-3.

From Figure 5-3 we can find that the average heating rate of the oven is approximately 2.8°C per hour. At such a low heating rate we assume that the temperature on the cutter surfaces, including the two ends of the shaft, is the same as that in the whole shaft. Therefore, the temperature in the oven should be equal to that in the shaft. Furthermore, the temperature measured in the field should actually be that of the shaft. To express this more precisely, the temperature measured should be that of the shaft surfaces where the two strain gauges were bonded.

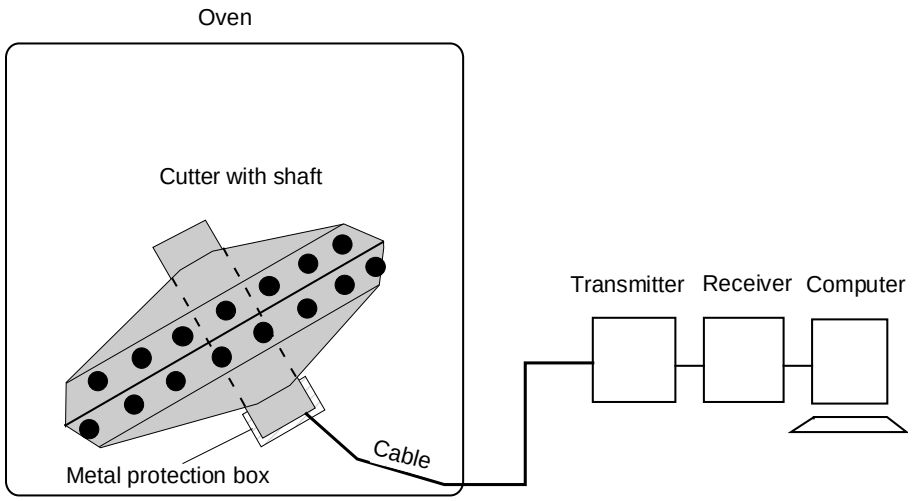

Figure 5-2. *Calibration system for temperature.*

As described above, the highest temperature in the laboratory calibration was only 55°C due to the safety of the cable. However, the actual temperature in the shaft in field excavation is probably higher than 55°C. Thus the calibration in the range of 0–55°C is not adequate to meet our requirements for temperature measurements. In order to solve this problem, we can extend the calibration equation in Figure 5-3. Because the temperature and voltages shown in Figure 5-3 have quite a good linear relationship, we can prolong the fitted straight line directly forward. In other words, we suppose that the calibration equation in Figure 5-3 can be used to determine the real temperature in the shaft.

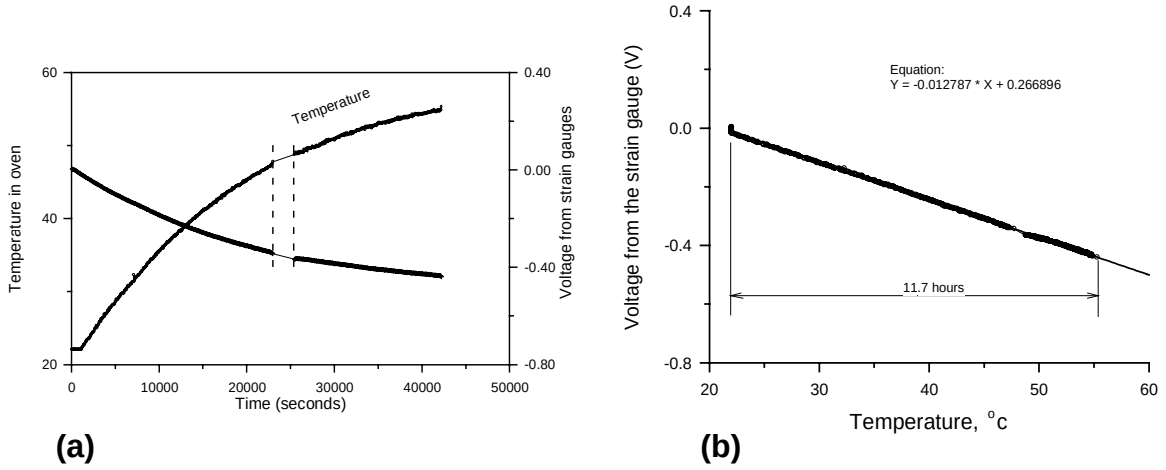

Figure 5-3. *Calibration results for temperature. (a) Recordings of temperature in oven and voltages from temperature gauges. (b) Calibration curve.*

5.3 Results of temperature measurements

The above calibration results were obtained without considering the effects of cutter forces on the temperature measurements. So it is necessary to check if such effects exist. In the laboratory force calibration, the temperature in the shaft of a cutter was equal to room temperature. During one-time calibration, which usually lasted 10–15 minutes, there was almost no change in the room temperature. Thus, any variation of the voltage from temperature gauges during the force calibration should only be caused by changes in the cutter forces. The calibration results proved good in that they showed that the cutter forces did not influence the temperature measurements. Figure 5-4 is the result of one laboratory calibration. From this figure we can see that, as the three forces change greatly, the voltage from the temperature gauges does not vary. Naturally, we can directly apply the results shown in Figure 5-3 to determine the real temperature in the shaft during field boring, and do not need to consider the effects of the cutter forces on the temperature measurements.

The calibration results in Figure 5-3 can be expressed as the following equation:

$$T = 20.85 – 78.13\ V \qquad (5\text{-}1)$$

Using equation (5-1), we can obtain the measurement results for the cutter temperature during the field excavation. Figure 5-5 shows the measurement results for casing 8–10. The different dot symbols in the figure are the measurement results. Each dot stands for the average temperature during 3.3 seconds of excavation. The solid lines are the fitted results. From the results shown in Figure 5-5 we can draw the following conclusions:

- The temperature in the shaft is mainly caused by the heat conducted from the cutter surface, rather than by the heat produced by the friction between the shaft surface and the inner surface of the cutter due to the cutter rotation. Otherwise, the first straight line in Figure 5-5 would have the same slope as the second line.

- The temperature on either the cutter surface or the shaft surface is mainly dependent on the boring time, if the rotation speed is kept as a constant. The thrust of the boring machine almost does not influence the temperature. This can be seen from Figure 5-5a. In this figure the thrust in casing 8 is markedly larger than that in casing 10. However, the slopes of their second lines and third lines are the same.

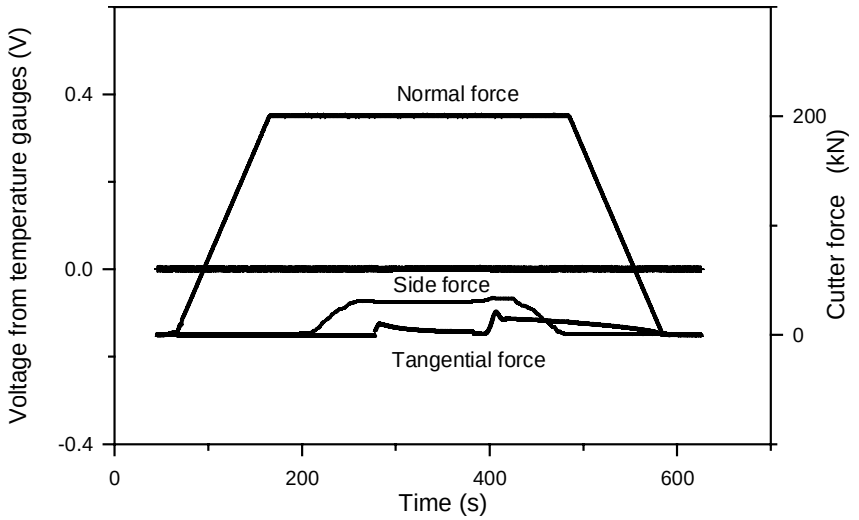

Figure 5-4. *Effect of cutter forces on temperature measurements.*

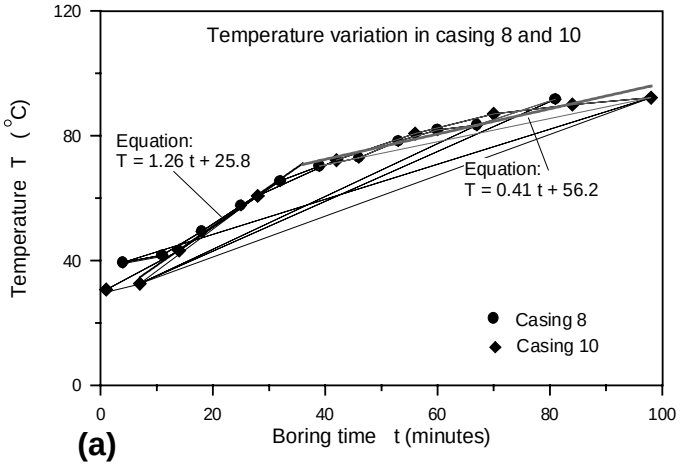

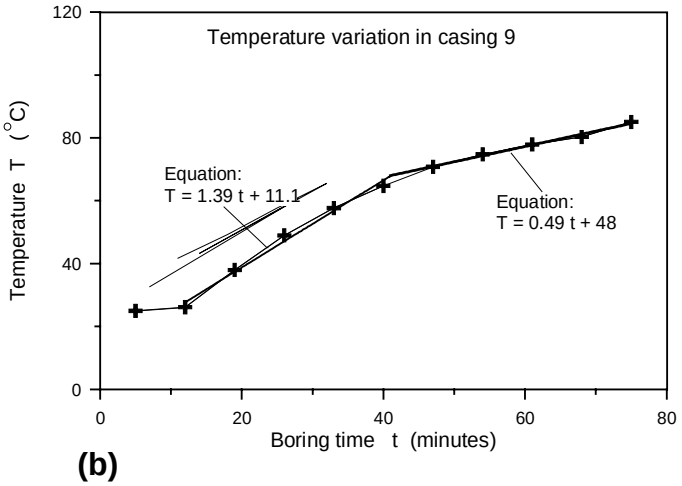

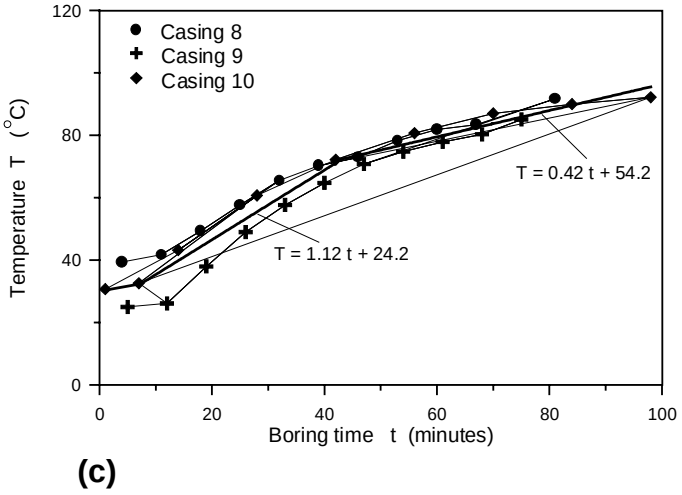

Figure 5-5. *Temperature variation in casing 8–10.*

- The relationship between the temperature and the boring time for each casing can be expressed by using three-part straight lines. The first line shows the variation of the cutter temperature in the initial period of each casing. This period lasts about 7–14 minutes. On the one hand, the temperature in the shaft decreases continuously in this period due to the temporary interruption of boring after the completion of the previous casing. On the other hand, the increasing heat from the cutter surface due to the resumption of boring is transferred into the shaft, and the temperature in the shaft starts to rise. Thus, the temperature on the shaft surface increases slowly compared with the subsequent two periods.

- The second straight line describes the cutter temperature under 75°C or so. During this period the difference between the cutter temperature and the air temperature surrounding the cutter is not so large, so the heat loss in the process of heat conduction from the cutter surface to the shaft is small or can be neglected. In other words, it can be assumed that the second line approximately expresses the variation of the temperature on the cutter surface.

- When the difference between the cutter temperature and the air temperature surrounding the cutter increases to a certain degree, the heat loss through radiation in the process of heat conduction from the cutter surface to the shaft augments greatly. Therefore, the third straight line in Figure 5-5 can only stand for the temperature on the shaft surface, rather than that on the cutter surface. Naturally, the temperature on the cutter surface should be higher than that on the shaft surface.

- The cooling time (or the duration of the temporary interruption of boring) between two neighbouring casings influences the slopes of the straight lines in Figure 5-5. For example, the cooling times between casing 7 and casing 8, casing 8 and casing 9, and casing 9 and casing 10 are 190 minutes, 910 minutes, and 253 minutes, respectively. Because the difference between 190 minutes and 253 minutes is not large, the second and third straight lines for casing 8 have the same slopes as the corresponding lines for casing 10 in Figure 5-5a. However, because 910 minutes is much longer than 190 minutes or 253 minutes, the slopes of the second and third lines for casing 9 in Figure 5-5b are greater than the corresponding slopes for casing 8 and casing 10. Moreover, it can be found that the influence of the cooling time on the slopes of the straight lines decreases with increasing boring time. For example, the influence of the cooling time on the slope of the third line is smaller than the corresponding influence on the slopes of the first and second lines. Therefore, for practical applications, the influence of the cooling time can be neglected, since our attention should be focused on boring for long periods rather than on boring for short periods.

On the basis of the above description, equation (5-2) and (5-3) below may be used to predict the shaft temperature of the cutter.

$$T = A_1 t + B_1 \qquad t < 45 \text{ minutes} \qquad (5\text{-}2)$$

$$T = A_2 t + B_2 \qquad t \geq 45 \text{ minutes} \qquad (5\text{-}3)$$

where A_1, B_1, A_2, and B_2 are the parameters determined by the measured data from casings 8–10. Their values are $A_1 = 1.12$, $B_1 = 24.2$, $A_2 = 0.42$, and $B_2 = 54.2$. They are determined according to the fitted results for all three casings. Equation (2) and (3) are also shown in Figure 5-5c.

It is necessary to point out that the above equations, including the parameters, are obtained while the rotation speed of the boring machine is kept at 10 rpm. Because the cutter temperature mainly increases due to the friction between the cutter surface and the rock, as analysed above, the rotation speed of the machine greatly influences the cutter temperature. A laboratory study of rock cutting using a diamond cutter shows that, if the cutter rotation speed is increased from 40 to 100 rpm, the cutter temperature rises from 7°C to 17°C /Cooper et al., 1994/. This almost means that, if the rotation speed is increased by 100%, the cutter temperature rises by 100% too. Assuming that the boring in the laboratory study is comparable to the field rock boring at Äspö, the real cutter temperature calculated by equation (5-2) and (5-3) should be doubled if the rotation speed is increased from 10 rpm to 20 rpm. For example, if the continuous boring lasts 1.5 hours, the shaft temperature will rise to 92°C according to equation (5-3). However, if the rotation speed of the boring machine is increased from 10 rpm to 20 rpm, the shaft temperature will rise to 184°C on the basis of the above analysis.

On the other hand, as discussed in conclusion 4 above, it is assumed that equation (5-2) may be used approximately to predict the cutter surface temperature. Then the cutter surface temperature will rise to 250°C if the boring lasts 1.5 hours and the rotation speed of the boring machine is kept at 20 rpm. In this case, the highest instantaneous temperature on the surface of the rock beneath the cutters probably rises to 250°C, but such a temperature does not last a long time for a certain piece of rock due to the continuous rotation of cutters. Therefore, if the continuous boring time is controlled within 1.5 hours or so, it can be considered that the high temperature due to rock boring does not markedly influence the mechanical properties of the rock beneath cutters. When the boring time is longer than 1.5 hours, however, a further study based on new measurements of the cutter temperature is needed. Finally, it is necessary to point out that in this study the air cooling method is used for the boring machine. If other cooling methods, such as water-cooling, were employed, the equations for the temperature would be different to a certain degree.

6 Investigation of cracks caused by mechanical boring

6.1 Determination of rock sampling positions

6.1.1 Boring period related to sampling positions

The aim of rock sampling from the borehole has mainly been to examine the cracks induced by mechanical boring, and to try to establish the relationship between the boring forces and the induced crack lengths.

According to the field photography shown in Figure 6-1, it can be determined that during the last rotation in boring the borehole, most buttons in the button cutter produced a small crater on the bottom of the borehole. This shows that most of the small craters, particularly the larger of the small craters, on the surfaces of the core samples were probably produced during the last rotation of boring. Furthermore, this does not exclude the possibility that some of the small craters were produced in previous rotations. However, the small craters produced in previous rotations should be smaller than those produced in the last rotation of boring.

On the basis of the above description, it is considered that the large craters on the surfaces of the core samples should mainly be connected to the cutter forces in the last rotation of boring.

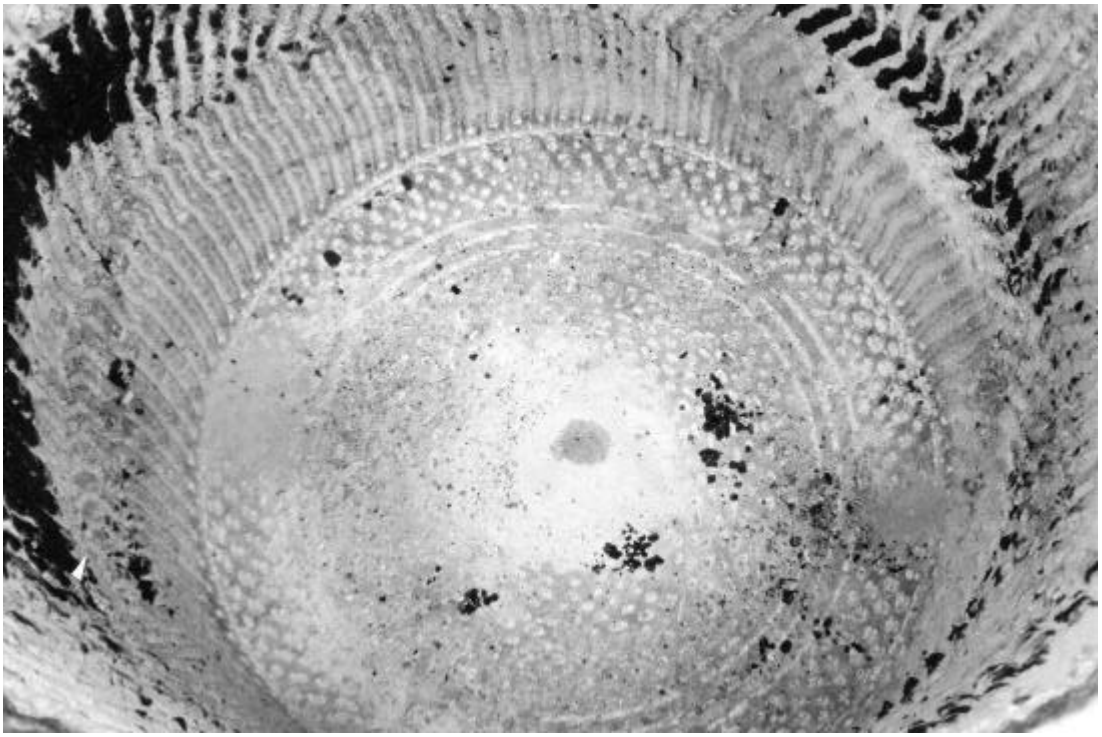

Figure 6-1. *Photograph of the borehole bottom.*

6.1.2 Selecting optimum sampling positions based on cutter forces

According to the rotation speed of the boring machine, we can estimate the time during which the machine covers one rotation. Therefore, we are able to obtain the normal forces of both the front cutter and the gauge cutter during the last rotation of boring, which is shown in Figure 6-2.

In order to examine the cracks induced by mechanical boring, the optimum sampling positions should be the places corresponding to the maximum normal forces in the last rotation of boring. However, these places were difficult to reach due to the limitation of in-situ core drilling. For example, two cases were sometimes encountered at the originally planned sampling positions during the core drilling: (1) there were clear joints, and (2) core drilling failed to take out a sample that was long enough to be used to examine the cracks. Thus, in the core drilling we were only able to approach the positions with the maximum normal forces as closely as possible.

First, we chose several maximum normal forces as the optimum sampling positions according to Figure 6-2. Then we determined the co-ordinates of the sampling positions relevant to the maximum normal forces. This process is described in the following.

- Four maximum normal forces for the front cutter were selected as the optimum sampling positions and named M1, M2, M3, and M4, as shown in Figure 6-2a. Similarly, two maximum normal forces for the gauge cutter were selected as the optimum sampling positions and named SA and SB, as shown in Figure 6-2b.

- The co-ordinates were determined for the sampling positions relevant to the maximum normal forces. The position of cutter 18A corresponding to a fixed point on the wall of the bored hole can be recorded at any time during boring. This fixed point is named “F1” in the drawing for the bottom of the borehole. We referenced the drawing as Figure 6-3. Therefore, the position of cutter 10 at any time in the borehole can also be decided as long as the angle between the two cutters (cutter 10 and 18A) in the cutter head is known. We know that this angle is 60 degrees from the drawings for the machine design.

We use α to stand for the instant position of cutter 10 in the Äspö co-ordinate system, shown by “Äspö 0°”in Figure 6-3. However, the field tests only give us the instant position angle α_G of cutter 18A in the “0” co-ordinate system, shown by “0°” in Figure 6-3. The broken lines in Figure 6-2 stand for α_G, and they imply that the in-situ measurement of the instant angle α_G is quite approximate. In order to choose sampling positions easily, we connect each upper point of one of the broken lines to express the angle α_G. Thus the instant position of cutter 10 in the “0” co-ordinate system is expressed by α_F, and we can obtain the following relationships according to Figure 6-3.

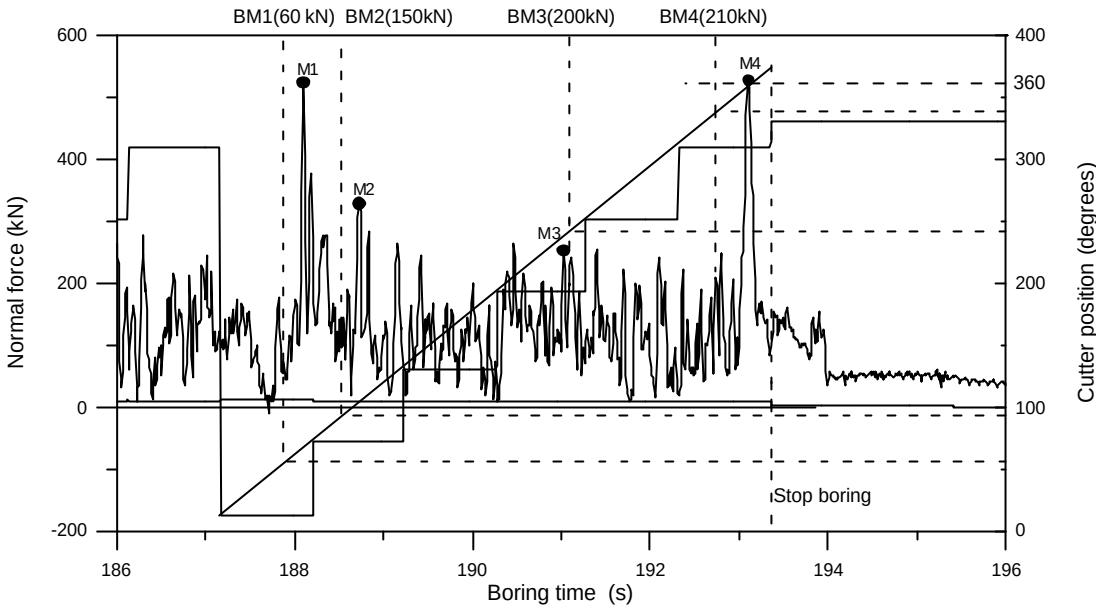

(a)

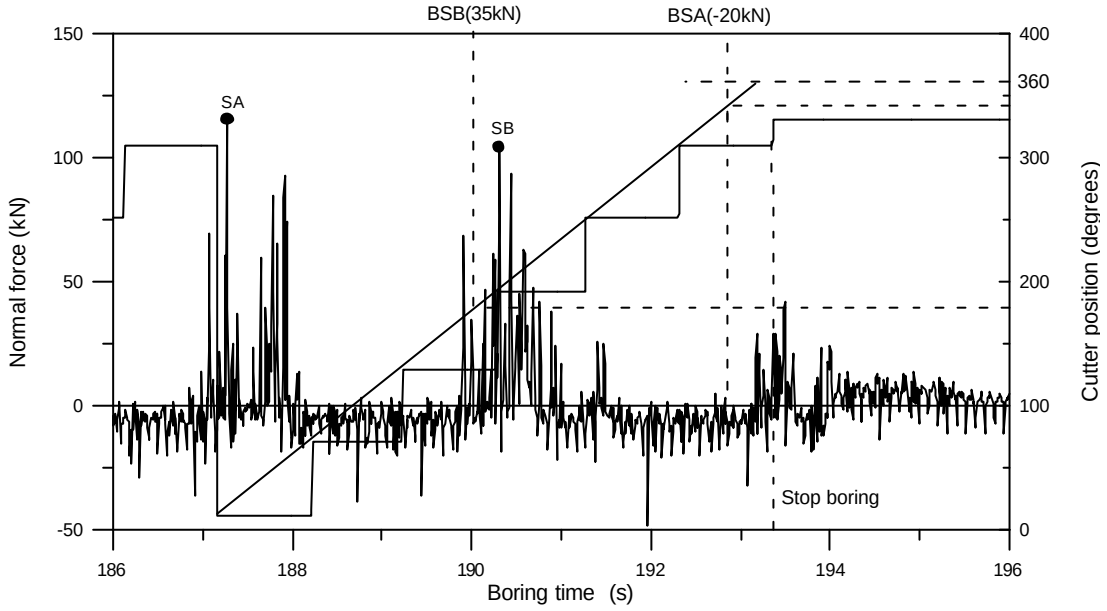

(b)

Figure 6-2. *Measured cutter forces during last rotation of boring. (a) Cutter forces of the front cutter corresponding to the sampling positions in the bottom of the borehole; (b) Cutter forces of the gauge cutter corresponding to the sampling positions in the bottom of the borehole.*

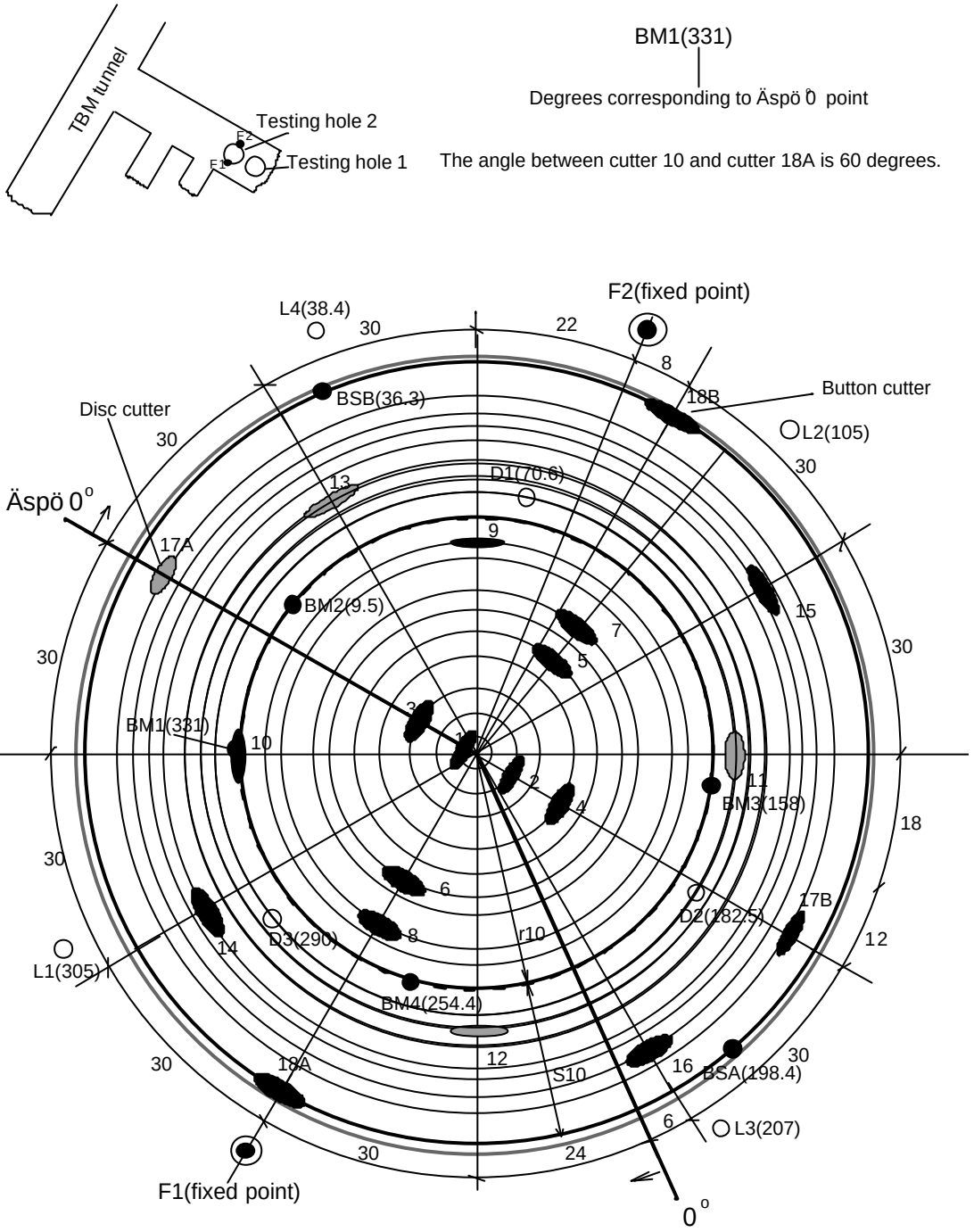

r1=5.5; r2=13.5; r3=21; r4=29; r5=36; r6=45; r7=51.5; r8=59.3; r9=65.5; r10=72.5 mm
r11=79, r12=85; r13=91; r14=96; r15=102; r16=106; r17A=r17B=110; r18A=r18B=112
Scale:1:8 (Real figures). e.g. in the borehole r10=72.5*8=580mm, S10=316mm

Figure 6-3. *Sampling positions on borehole bottom.*

$\alpha_F = 60° + \alpha_G$

$$\alpha = \alpha_F + 216° = 276° + \alpha_G \quad (6\text{-}1a)$$

or

$$\alpha_G = \alpha - 276° \quad (6\text{-}1b)$$

Equation (6-1b) is used for the front cutter. Here α_G is actually the readings for the gauge cutter from the field-sampling data. Similarly, we can also obtain the following relationships for the gauge cutter:

$$\beta = \alpha_G + 216° \quad (6\text{-}2a)$$

or

$$\alpha_G = \beta - 216° \quad (6\text{-}2b)$$

Where β is the instant position of gauge cutter 18A in the Äspö co-ordinate system, and α_G the instant position of cutter 18A in the "0" co-ordinate system.

According to the above process, the angle α corresponding to each maximum normal force can be determined. Considering the actual limitation of in-situ core drilling, some final sampling positions are more or less different from the originally planned ones. The rock core samples taken from the final positions are named BM1, BM2, BM3, BM4, BSA and BSB. The relevant data for the samples corresponding to cutter 10 and cutter 18A are shown in Table 6-1 and 6-2. And their respective normal forces can be seen in Figure 6-2.

Table 6-1. Sampling positions on the bottom for cutter 10.

Reference No.	No. of sample	Co-ordinate Z (m)	Angle a (from Äspö 0 point)	a_G from sampling data	Inclination degrees)
KD0086G05	BM1	-425.5	331	55	-90
KD0086G06	BM2	-425.5	9.5	-266.5/93.5	-90
KD0086G07	BM3	-425.5	158	-118/242	-90
KD0086G08	BM4	-425.5	254.4	-21.6/338.4	-90

Table 6-2. Sampling positions on the bottom for cutter 18A.

Reference No.	No. of sample	Co-ordinate Z (m)	Angle b (from Äspö 0 point)	a_G from sampling data	Inclination degrees)
KD0086G09	BSA	-425.3	198.4	-17.6/342.4	-20
KD0086G10	BSB	-425.3	36.3	-179.7/180.3	-20

Three positions on the bottom for the disc cutter were chosen so that we might investigate the cracking induced by disc cutters. The data are listed in Table 6-3.

Table 6-3. Sampling positions on the bottom for disc cutter.

Reference No.	No. of sample	Co-ordinate Z (m)	Angle (from Äspö 0 point)	Inclination degrees)
KD0086G11	D1	-425.4	70.6	-90
KD0086G12	D2	-425.4	182.5	-90
KD0086G13	D3	-425.4	289.7	-90

Four other positions on the wall of the borehole were selected for examining the cracking in different casings and different geological conditions. L1 and L2 were chosen in casing 10, and L3 and L4 in casing 9 and in another rock type. The data are listed in Table 6-4.

Table 6-4. Sampling positions on the wall for cutter 18A.

Reference No.	No. of sample	Co-ordinate Z (m)	Angle a (from Äspö 0 point)	Inclination degrees)
KD0086G14	L1	-424.8	304.9	0
KD0086G15	L2	-424.8	104.8	0
KD0086G16	L3	-424.2	207.3	0
KD0086G17	L4	-424.2	38.4	0

*The height from the bottom (middle part) of the borehole to the top of cutter 18A is equal to 200 mm according to the drawing for the machine design.

The positions of all the cutters in the cutter head are shown in Figure 6-3. Each cutter produces a circular track on the bottom of the borehole. The outermost circle close to the circle of cutter 18A is assumed to be the wall of the borehole. In fact, the distance between the outermost circle and that of cutter 18A is quite small, or it can be ignored. For most cutters, except for cutter 5 and 7, the angle between two neighbouring cutters in the periphery direction is 30 degrees. The final sampling positions on the bottom of the borehole for BM1-BM4, BSA and BSB are shown in Figure 6-4.

Two other samples were taken from the wall of the first test borehole that was completely drilled by disc cutters. Their relevant data are listed in Table 6-5. The geological conditions in the sampling positions are basically the same as most of the rock in the two boreholes.

Table 6-5. Sampling positions on the wall of borehole 1.

Reference No.	No. of sample	Co-ordinate Z (m)	Angle (from Äspö 0 point)	Inclination degrees)
KD0092G05	1	-424.7	118.8	0
KD0092G06	2	-424.4	273.8	0

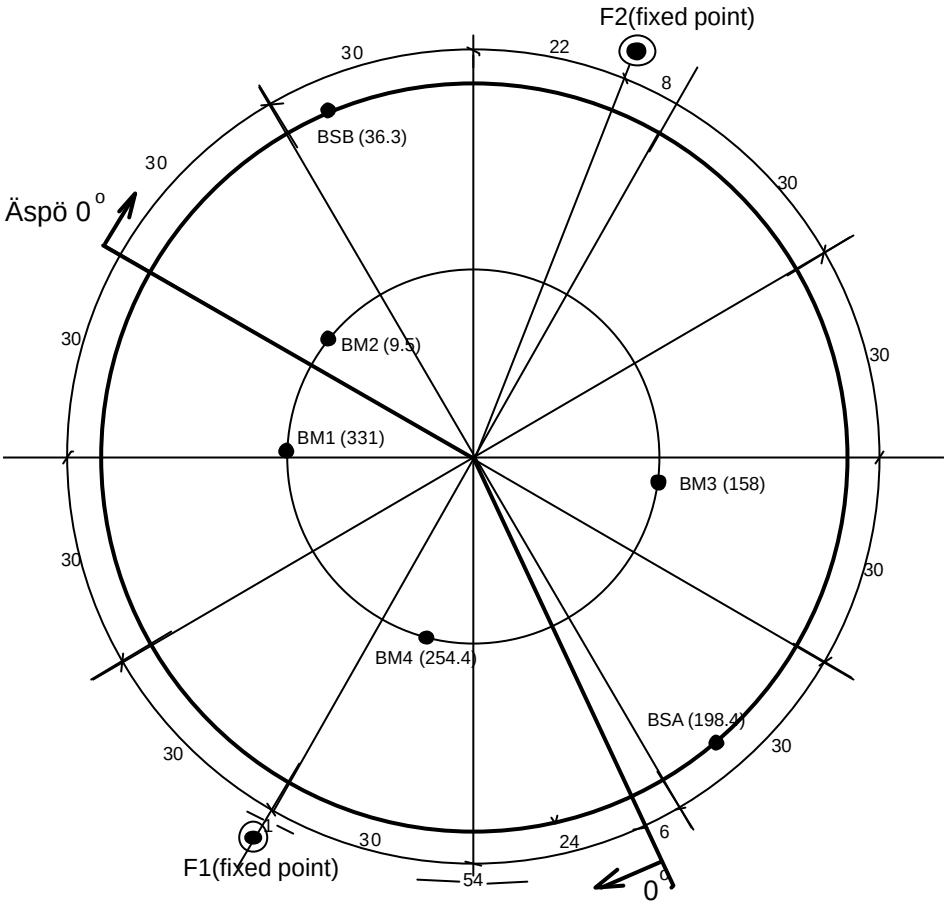

Figure 6-4. *Sampling positions in the bottom of the test borehole. The figures corresponding to each sampling number are based on the Äspö co-ordinate system.*

Furthermore, the rock samples taken from the borehole show that there are usually multi-craters on the surfaces of the samples. Figure 6-5 indicates the co-ordinates of the craters on the surface of each sample. The sizes of all the craters are basically divided into two kinds: large or small. It is evident that the large craters on the surface of one sample were produced during the last rotation of boring, because the distances between them are usually the same as the distances between the neighbouring buttons in the cutters. For example, the shortest distance between two neighbouring craters is 46 mm. This is exactly equal to the distance between two neighbouring buttons located on two different rows of the cutters. Thus, the co-ordinates of all the craters can be determined. They are listed in Table 6-6.

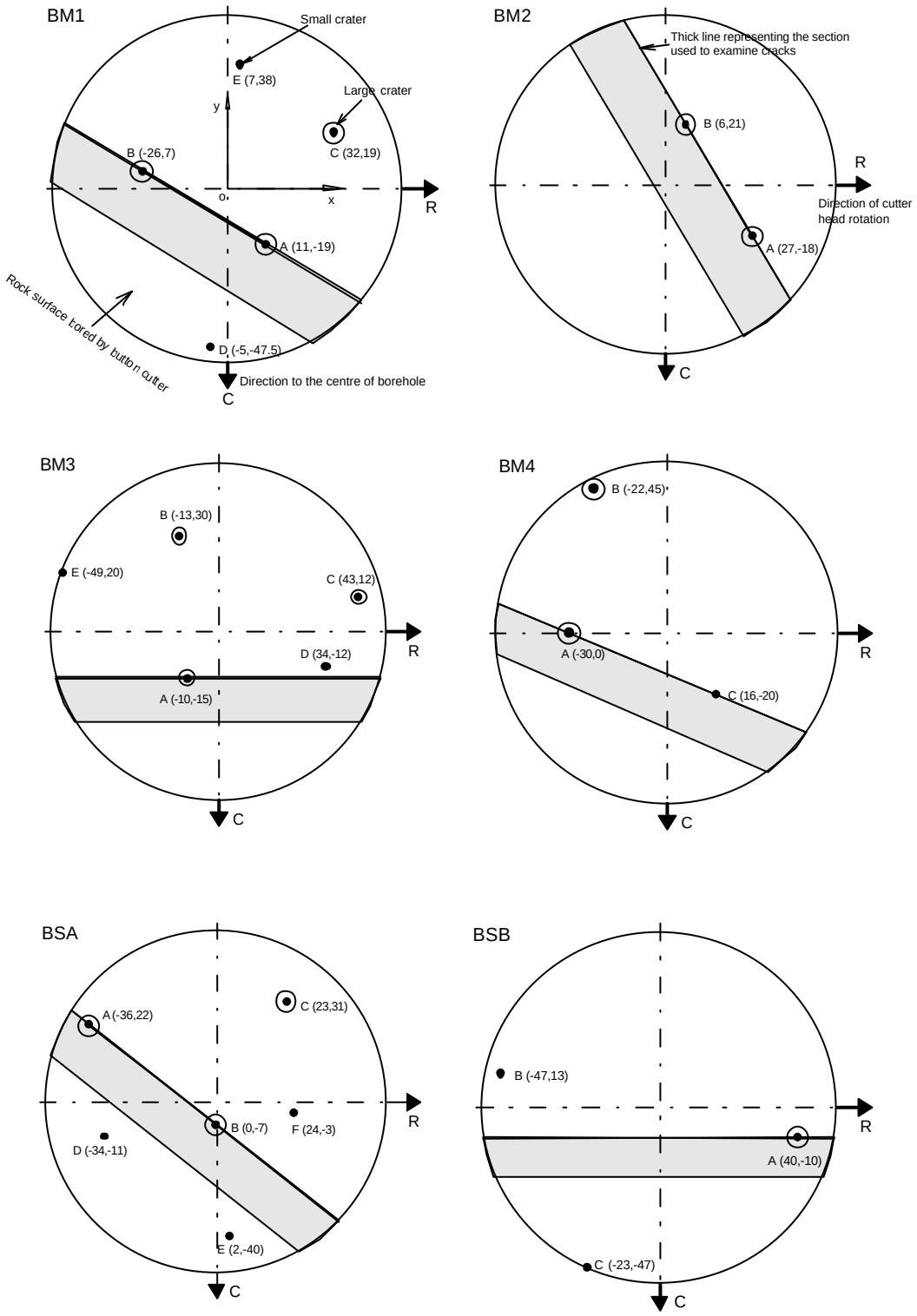

Figure 6-5. *Co-ordinates of craters produced on surfaces of rock core samples. The shadows represent the parts of the core samples that remained after cutting. The remaining parts were used to investigate cracks. The thicker lines in the shadows indicate the polished surfaces on which the crack examinations were performed.*

Table 6-6. Sampling positions on the bottom for cutter 10.

Reference No.	No. of sample or crater	Co-ordinate Z (m)	Angle a (from Äspö 0 point)	a_G from sampling data
KD0086G05	BM1	-425.5	331	55
	BM1(A)	-425.5	332.2	56.2
	BM1(B)	-425.5	328.2	52.2
KD0086G06	BM2	-425.5	9.5	-266.5/93.5
	BM2(A)	-425.5	12.2	-263.8/96.2
	BM2(B)	-425.5	10.1	-265.9/94.1
KD0086G07	BM3	-425.5	158	-118/242
	BM3(A)	-425.5	157	-119/241
KD0086G08	BM4	-425.5	254.4	-21.6/338.4
	BM4(C)	-425.5	256	-20/340
	BM4(A)	-425.5	251.4	-24.6/335.4

Table 6-7. Sampling positions on the bottom for cutter 18A.

Reference No.	No. of sample or crater	Co-ordinate Z (m)	Angle b (from Äspö 0 point)	a_G from sampling data
KD0086G09	BSA	-425.3	198.4	-17.6/342.4
	BSA(A)	-425.3	196	-20/340
	BSA(B)	-425.3	198.4	-17.6/342.4
KD0086G10	BSB	-425.3	36.3	-179.7/180.3
	BSB(A)	-425.3	38.9	-177.1/182.9

In Table 6-6 and 6-7, the symbol " - " in last column can be replaced by a positive value after " / ". For example, -216.5 and 143.5 have the same position in the bottom of the borehole. Their relation is –216.5 + 360 = 143.5. Thus, on the basis of the values of α_G we can find the cutter forces corresponding to the sampling positions in Table 6-6 and 6-7.

According to the results in Table 6-6 and 6-7, the normal forces relevant to each crater are shown in Figure 6-6 and listed in Table 6-8.

Table 6-8. Normal forces corresponding to each crater on the samples during last rotation.

Crater No.	Normal force(kN)	Crater No.	Normal force(kN)	Crater No.	Normal force(kN)
BM1(A)	60	BM3(A)	240	BSA(A)	3
BM1(B)	80			BSA(B)	-20
BM2(A)	185	BM4(A)	175	BSB(A)	15
BM2(B)	120	BM4(C)	210		

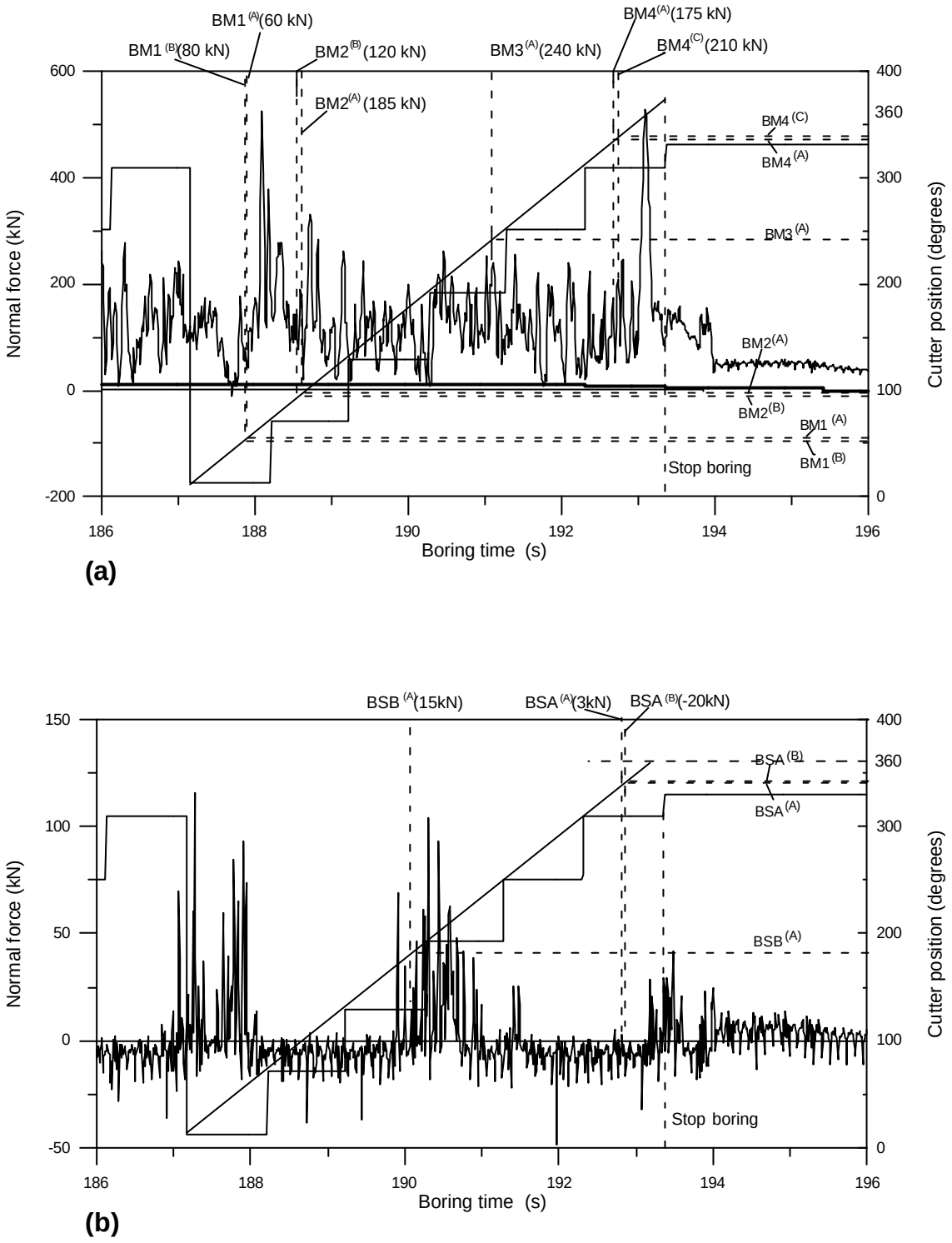

Figure 6-6. *Cutter forces and sampling positions. (a) Cutter forces of the front cutter corresponding to the sampling positions in the bottom of the borehole; (b) Cutter forces of the gauge cutter corresponding to the sampling positions in the bottom of the borehole.*

From Figure 6-6 we can find that the craters $BM1^{(A)}$ and $BM1^{(B)}$ are not related to any peaks of normal forces, and the normal forces corresponding to $BSA^{(A)}$ and $BSB^{(A)}$ are either negative or very small. Such normal forces are not large enough to produce the craters in the rock surface. A similar result was also found when the normal forces corresponding to the previous rotations were analysed. As discussed above, this is probably caused by the approximate values of the instant angles of cutter 18A measured in-situ. A reasonable but approximate method is to use the shadow areas in Figure 6-7 to substitute the upper straight lines. Thus, it is possible that a number of normal force peaks within the overlapped area of a horizontal dash line and the slanting shadow area are the normal force that in fact produces the relevant crater in a core sample. On the basis of the above description, we take a range of normal forces from minimum to maximum in the overlapped area as the normal force to be determined. However, in determining the minimum and maximum normal forces, the following three factors were considered. (1) The time between two neighbouring craters (such as $BM1^{(A)}$ and $BM1^{(B)}$) in each core sample should be as equal as possible to each other. (2) The time between any two rock samples in Figure 6-7 should be as constant as possible. (3) Only as $F_N \geq 60$ kN, can the crater be produced by a button. In other words, the selected normal force peak should be equal to or greater than 60 kN. Considering these factors, the minimum normal forces (with the symbol of a small circle) and the maximum normal forces (with the symbol of a small square) were determined, and they are shown in Figure 6-7.

In addition, according to the above description, the crater $BM4^{(C)}$ was probably produced in the rotation previous to the last rotation of boring. This can also be confirmed by the fact that there is no other peak force near the crater $BM4^{(A)}$. Thus the force relevant to $BM4^{(C)}$ should be determined by the results measured for the second rotation of boring counted from the last rotation. This is shown in Figure 6-7b. For the craters $BSA^{(A)}$ and $BSA^{(B)}$, from Figure 6-7c for the last rotation of boring, the possible maximum force is only 42 kN. It is considered that such a normal force cannot produce a crater in rock as analysed above. Therefore, we should find their respective normal forces in the second rotation of boring shown in Figure 6-7d. Following this procedure, we can obtain the results indicated in Figure 6-7 and Table 6-9.

Table 6-9. Normal forces corresponding to each crater.

Crater No.	Normal force(kN)	Crater No.	Normal force(kN)	Crater No.	Normal force(kN)
$BM1^{(A)}$	150–375	$BM3^{(A)}$	130–253	$BSA^{(A)}$	70–106
$BM1^{(B)}$	150–525			$BSA^{(B)}$	60–78
$BM2^{(A)}$	150–281	$BM4^{(A)}$	160–532	$BSB^{(A)}$	62–103
$BM2^{(B)}$	134–330	$BM4^{(C)}$	150–240		

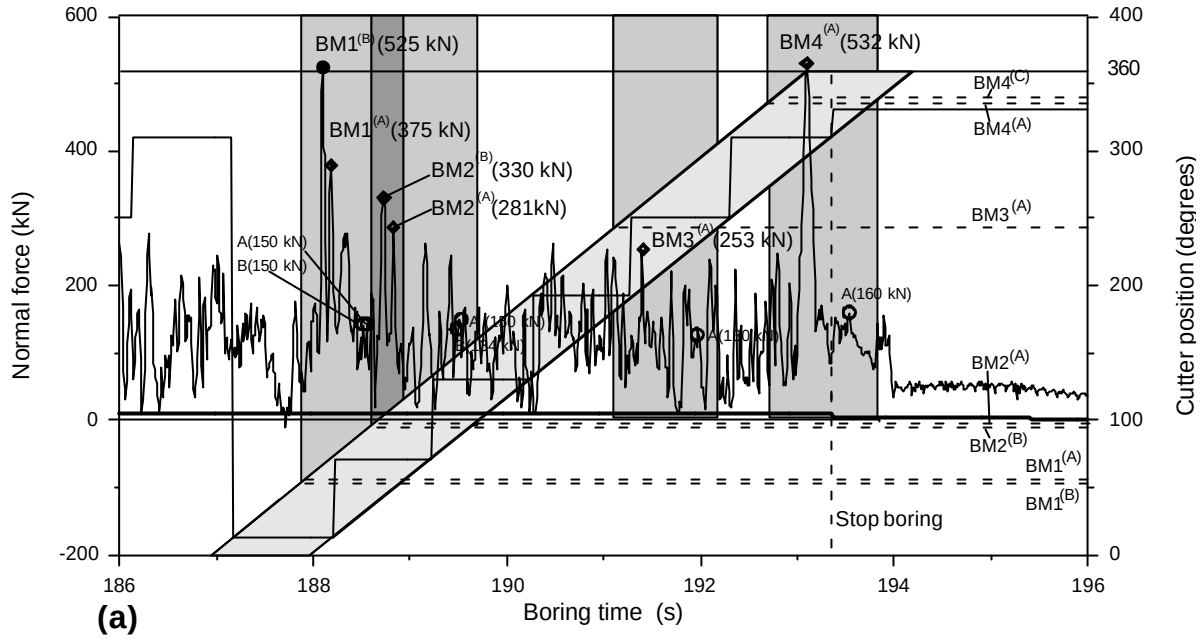
BM1(B) (525 kN)
BM4(A) (532 kN)
BM4(C)
BM4(A)
BM1(A) (375 kN)
BM2(B) (330 kN)
BM2(A) (281kN)
BM3(A) (253 kN)
BM3(A)
A(150 kN)
B(150 kN)
A(160 kN)
BM2(A)
BM2(B)
BM1(A)
BM1(B)
Stop boring
Normal force (kN)
Cutter position (degrees)
Boring time (s)
600
400
200
0
-200
400
360
300
200
100
0
186
188
190
192
194
196

(a)

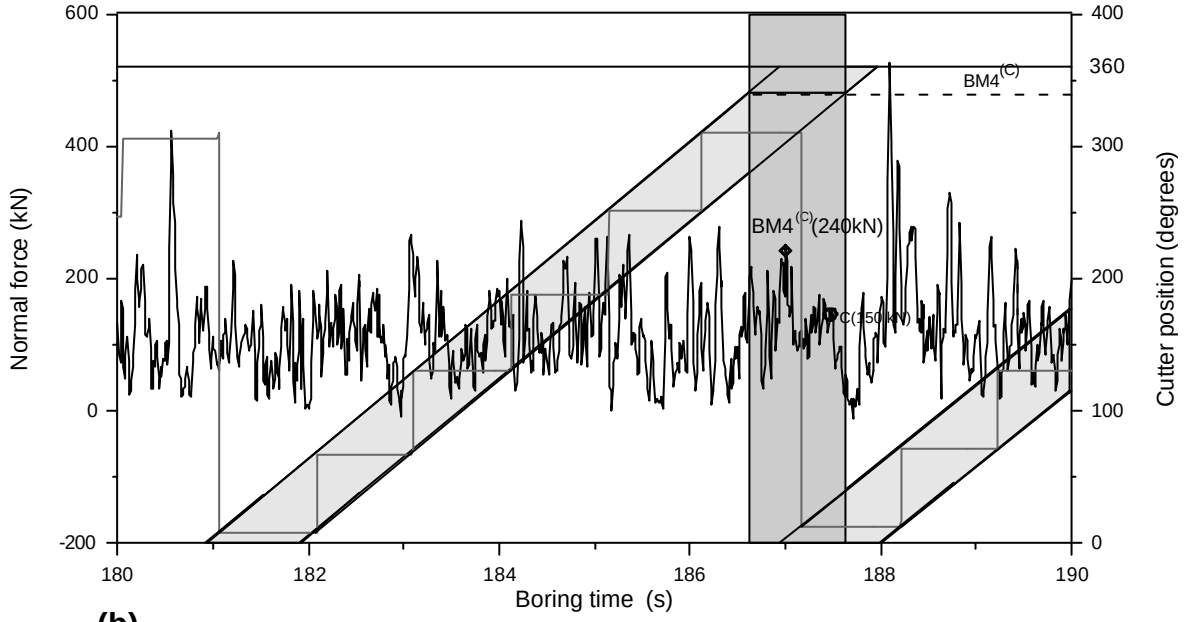
BM4(C)
BM4(C) (240kN)
C(150 kN)
Normal force (kN)
Cutter position (degrees)
Boring time (s)
600
400
200
0
-200
400
360
300
200
100
0
180
182
184
186
188
190

(b)

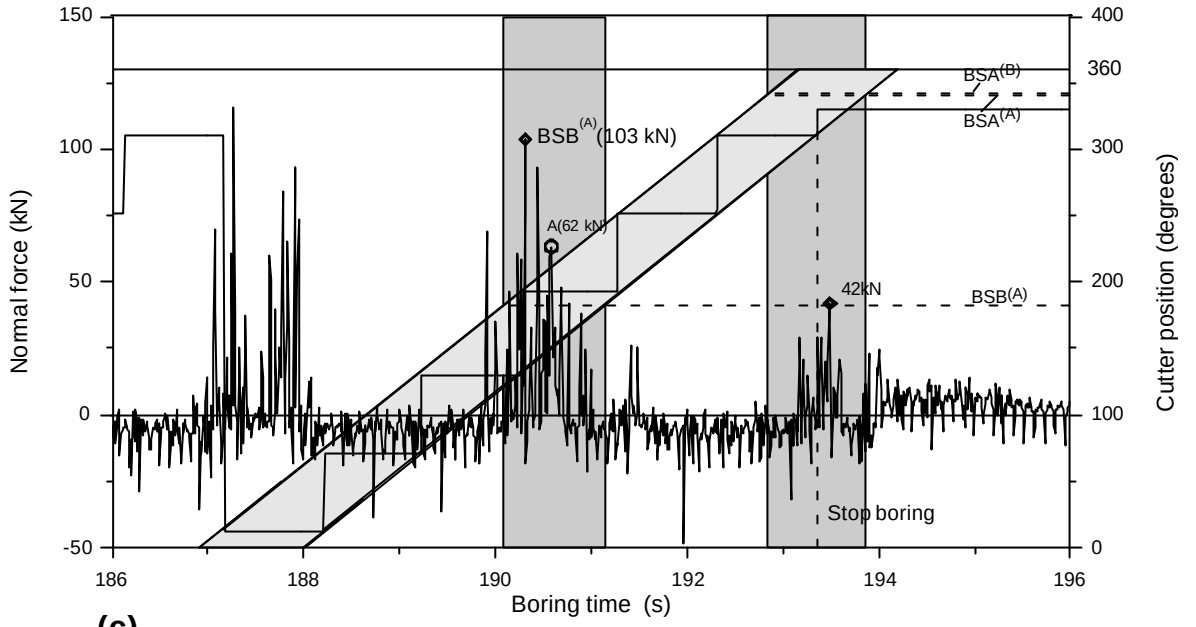

(c)

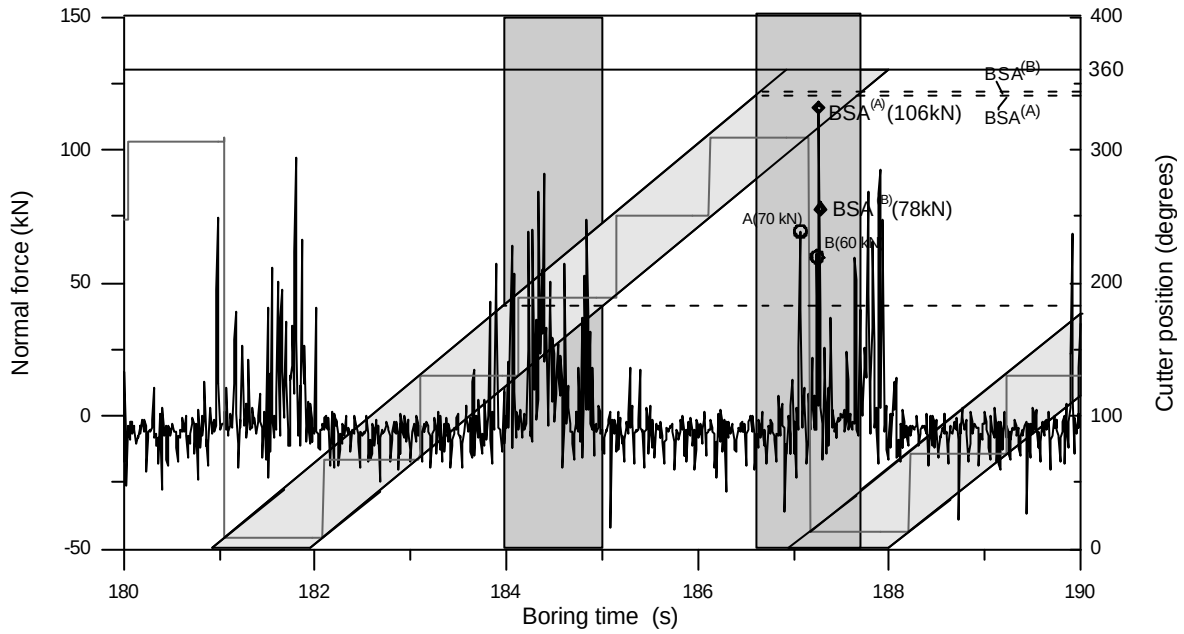

(d)

Figure 6-7a–d. *Normal forces relevant to each produced crater.*

6.2 In-situ rock sampling

According to previous experience of Äspö in-situ rock sampling Svemar, 1995; Kou and Tan, 1995; Tan and Kou, 1995/, two kinds of rock samples were taken from each sampling position. The first kind was for crack examination and the second for strength testing. The diameter of the first kind of samples is D=105 mm, and the length L=300 mm. The diameter of the second kind of sample is D*= 40 mm, and the length L*=600 mm. Except for the sampling positions D1 and D2, from which only the first kind of sample was taken, all the other positions (BM1, BM2, BM3, BM4, BSA, BSB, L1, L2, L3 and L4) were used to take out both kinds of core-rock samples. The sampling sizes of the core samples are shown in Figure 6-8. The core samples from BSA and BSB were taken out at an angle of 20 degrees with the horizontal direction of the bottom.

BM1 to BM4 are located on the circle periphery made by cutter 10. There are many small craters on this circle periphery, see Figure 6-9. Such small craters are caused by the buttons on cutter 10 during boring. Every two craters are usually joined together since their respective buttons on the cutter are very close to each other. It can be easily found that the circle periphery for cutter 10 is situated on the 9th circle from the outside edge, see Figure 6-9. The 6th, 7th and 8th circles are formed due to three disc cutters. The tracks for these three circles are very different from those for button cutters. Thus we can easily find the 9th circle.

Using a similar method to the one above, we can find the first circle periphery on which BSA and BSB are located. On the bottom of the borehole, the track for the first circle periphery is not so clear as the other ones, e.g. the 2nd and 6th. However, we can still find it by means of observation of the bottom. In fact, below the ends of the almost vertical straight grooves produced by the buttons on the surface of the fixed outside part of the boring machine, there is a circle periphery consisting of many small craters.

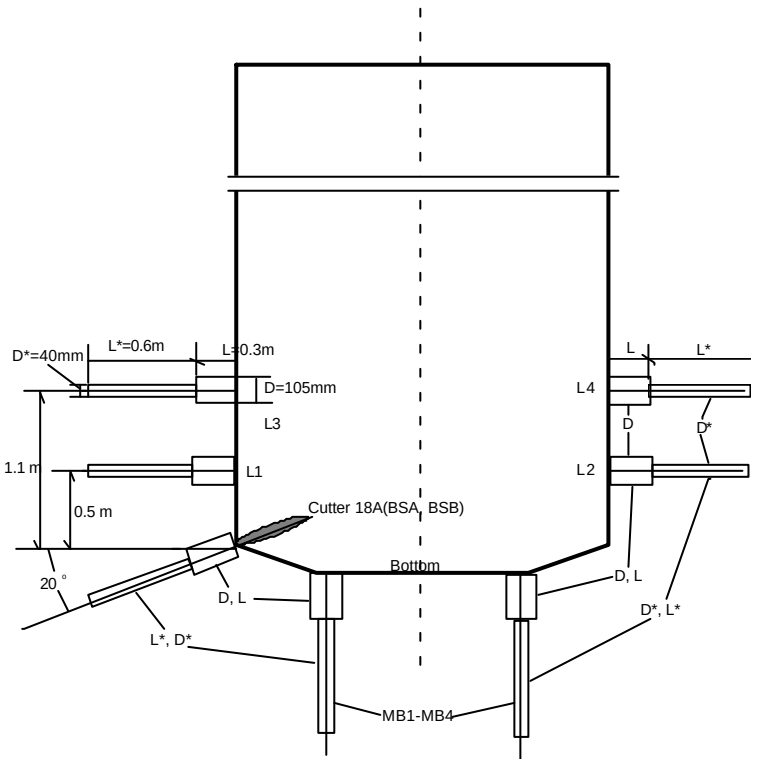

Figure 6-8. *Positions and sizes of core rock samples.*

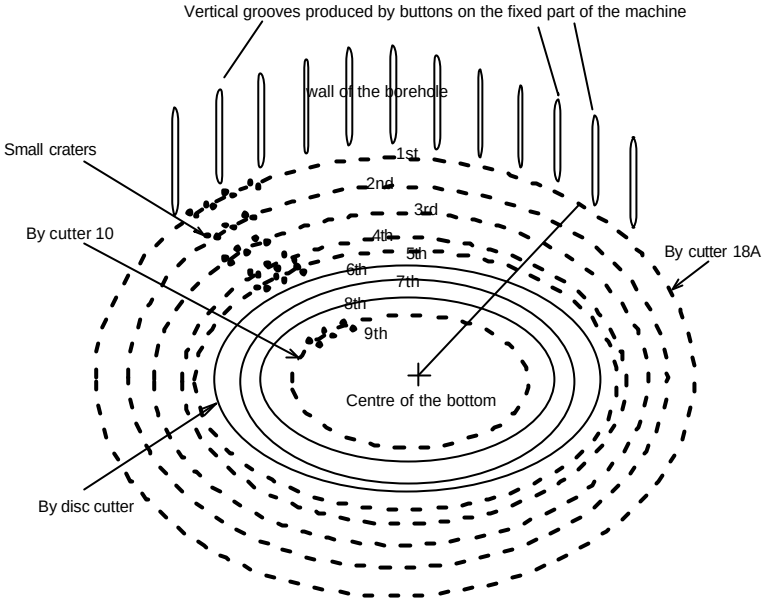

Figure 6-9. *Tracks produced by different cutters on bottom.*

For the sampling positions made by button cutters, the core samples should include at least two joined small craters made by buttons on the cutter, see Figure 6-10a. For the sampling positions made by disc cutters, the core samples should include at least one track made by the disc cutter, see Figure 6-10b. For the sampling positions on the wall of the borehole, the core samples should include at least one vertical track on the wall, see Figure 6-10c.

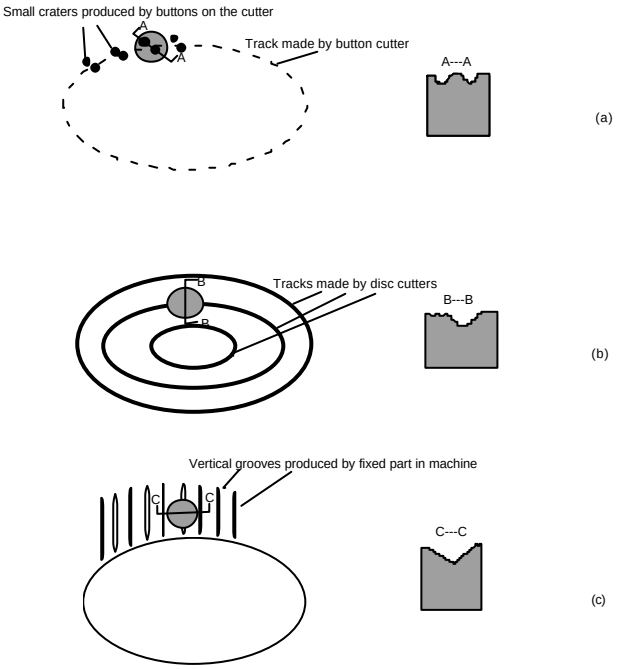

Figure 6-10. *Positions for core drilling in borehole.*

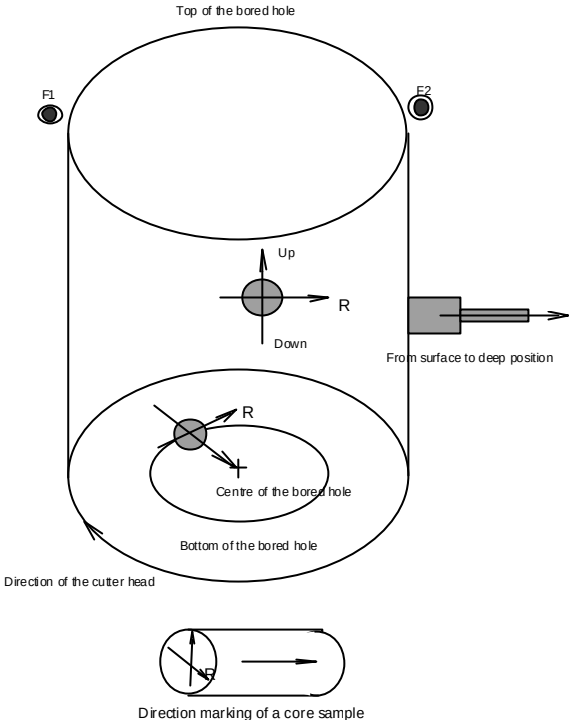

Figure 6-11. *Direction marking for core samples.*

The cutter-made surfaces (i.e. the part of the bottom or the wall of the borehole) of the core samples with a diameter of 105 mm were protected for crack examinations later on. After core drilling, all of the core samples, particularly their surfaces, were wrapped with soft materials.

For each core sample, three directions were also marked on its surface. For the core samples from the bottom of the borehole, the direction for the cutter-head rotation and the direction from the core location to the centre of the borehole were indicated. For the core samples from the wall of the borehole, the direction for the cutter-head rotation and that for the top and bottom of the borehole were marked. In addition, for all the core samples, the direction from the bottom or from the wall of the borehole to deep positions was indicated on the samples. All three directions are shown in Figure 6-11.

6.3 Mechanical properties of rock

The rock within and around the borehole can be basically divided into two kinds: Äspö diorite and granite. The geological data provided by Äspö Hard Rock Laboratory show in detail the rock types of each core sample. According to the data, rock specimens of each type were selected for strength testing. The uniaxial compressive strength, uniaxial tensile strength (by the Brazilian test), Young's modulus, and Poisson ratio of the two rocks were measured. The results are shown in Table 6-10. In Table 6-10 the specimen numbers including G represent granite, and those including D diorite.

Table 6-10a. Uniaxial compressive strength of the rocks.

No.	D (mm)	H (mm)	s_c (Mpa)	E (Gpa)	n
D1	40.2	84.2	90.22	60.13	0.175
D2	40.2	84.0	101.32	53.36	0.215
D3	40.2	84.0	60.69	32.65	0.306
D4	40.2	83.5	63.12	23.04	
D5	40.2	83.5	72.88	55.20	0.387
D6	40.2	84.2	73.15	55.52	0.141
D7	40.2	84.0	140.88	55.15	0.221
Average	0	83.9	86.04	47.86	0.24
Standard deviation	0	0.3	28.2	14.1	0.1
G1	40.2	84.0	83.71	27.09	0.322
G2	40.2	84.0	73.42	29.79	0.346
G3	40.2	84.3	167.97	61.53	0.281
G4	40.2	83.4	91.3	61.00	0.211
G5	40.2	83.0	170.14	62.66	0.203
G6	40.2	84.5	59.87	39.23	0.229
G7	40.0	84.3	77.21	55.86	0.178
G8	40.2	84.4	52.29	58.87	0.159
Average	40.2	84	96.99	49.5	0.24
Standard deviation	0.1	0.5	46.2	14.5	0.1

Table 6-10b. Uniaxial tensile strength of the rocks.

No.	D (mm)	H (mm)	s_t (MPa)	No.	D (mm)	H (mm)	s_t (Mpa)
D11	40.2	29.2	6.25	G11	40.2	27.5	11.29
D12	40.2	28.2	11.28	G12	40.0	28.0	14.07
D13	40.2	30.2	6.18	G13	40.2	25.9	10.04
D14	40.2	27.7	9.11	G14	40.2	30.7	7.84
D15	40.2	29.1	9.33	G15	40.2	28.3	12.89
D16	40.2	27.1	7.73	G16	40.2	28.5	11.03
D17	40.2	26.6	11.96	G17	40.0	28.5	7.80
				G18	40.2	29.2	6.25
Average	40.2	28.3	8.83	Average	40.2	28.3	10.15
Standard deviation	0	1.3	2.3	Standard deviation	0.1	1.4	2.7

6.4 Measured crack lengths

In order to examine the cracks induced by mechanical boring, we cut each rock sample as shown in Figure 6-5. The sections marked with thicker lines in the figure were used for examining the cracks produced by mechanical boring. Usually on each of the sections there are one or two craters which were produced by the buttons of the button cutters. Surrounding the craters, many cracks with different sizes can be clearly seen by means of the Scanning Electron Microscope (SEM). However, it is not easy to see such

cracks clearly by the naked eye. This indicates that the amplification chosen in the SEM experiments is related to the results for the crack examination. A proper amplification should be one that is large enough to see the main cracks very clearly, but not so large as to prevent a sufficient number of photographs being taken in the SEM experiments. On the basis of initial tests, we chose 20 as a fixed amplification for the SEM experiments. Figure 6-12a–h shows the results of the SEM photography. The crack system of each crater was continuously photographed. On the basis of the photographs, we are able to measure the length of each major crack induced by mechanical boring. The measurement results are compiled in Table 6-11. L_m, L_s and d in the table represent the medium crack length, the side crack length and the diameter of the hemispherical buttons in the button cutters, respectively. The symbol "*" in Table 6-11 means that no clear medium crack or side crack was found in the section of the crater in question. This is probably due to the fact that the section does not go through the position where a medium or side crack is located. So the L_m and L_s with symbol "*" were approximately determined according to the sizes of the craters produced by their relevant buttons. Naturally, such an L_m or L_s would be smaller than a real one.

Table 6-11. Length of medium and side cracks induced by mechanical boring.

No.	L_m (mm)	L_s (mm)	F_N (kN)	d (mm)	Rock type
BM1(A)	8.57*	15	150–375	24	Äspö diorite
BM1(B)	13.93*	18.57*	150–525	24	Äspö diorite
BM2(A)	17.86	21.43*	150–281	24	Äspö diorite
BM2(B)			134–330	24	Äspö diorite
BM3(A)	16.57	17.14*	130–253	24	Granite
BM4(A)	27.14	17.86	160–532	24	Äspö diorite
BM4(C)	16.43	17.14*	150–240	24	Granite
BSA(A)	7.86*	14.29	70–106	24	Granite
BSA(B)	5.71*	18.57*	60–78	24	Granite
BSB(A)	7.86*	10.71*	62–103	24	Granite

6.5 Theoretically predicted length of medium cracks

According to Kou /1995/, the relationship between the indentation force of a hemispherical indenter and the length of the medium crack induced in rock is

$$L_m^{3/2}\left(\frac{EG_{IC}}{1-n^2}\right)^{1/2}/F_N = 2.8\times10^{-2} + 3.09\times10^{-2}\left(\frac{F_N}{s_c d^2}\right) \quad (6\text{-}3)$$

where
L_m = length of medium crack,
E = Young's modulus,
G_{IC} = energy release rate,
ν = Poisson ratio,
σ_c = uniaxial compressive strength,
d = diameter of the hemispherical indenter (or button).

(a). The crater with a densely cracked zone corresponding to BM1$^{(A)}$. The densely cracked zone is located around the crater (the black area in the left side) and it consists of many short cracks. No medium crack was found, probably because this section did not go through the position where the medium crack is located.

(b). The crater with a densely cracked zone and medium cracks corresponding to BM2$^{(A)}$. The densely cracked zone is located around the crater (the black area in the left side) and it consists of many short cracks. The medium cracks are in the right side of the picture.

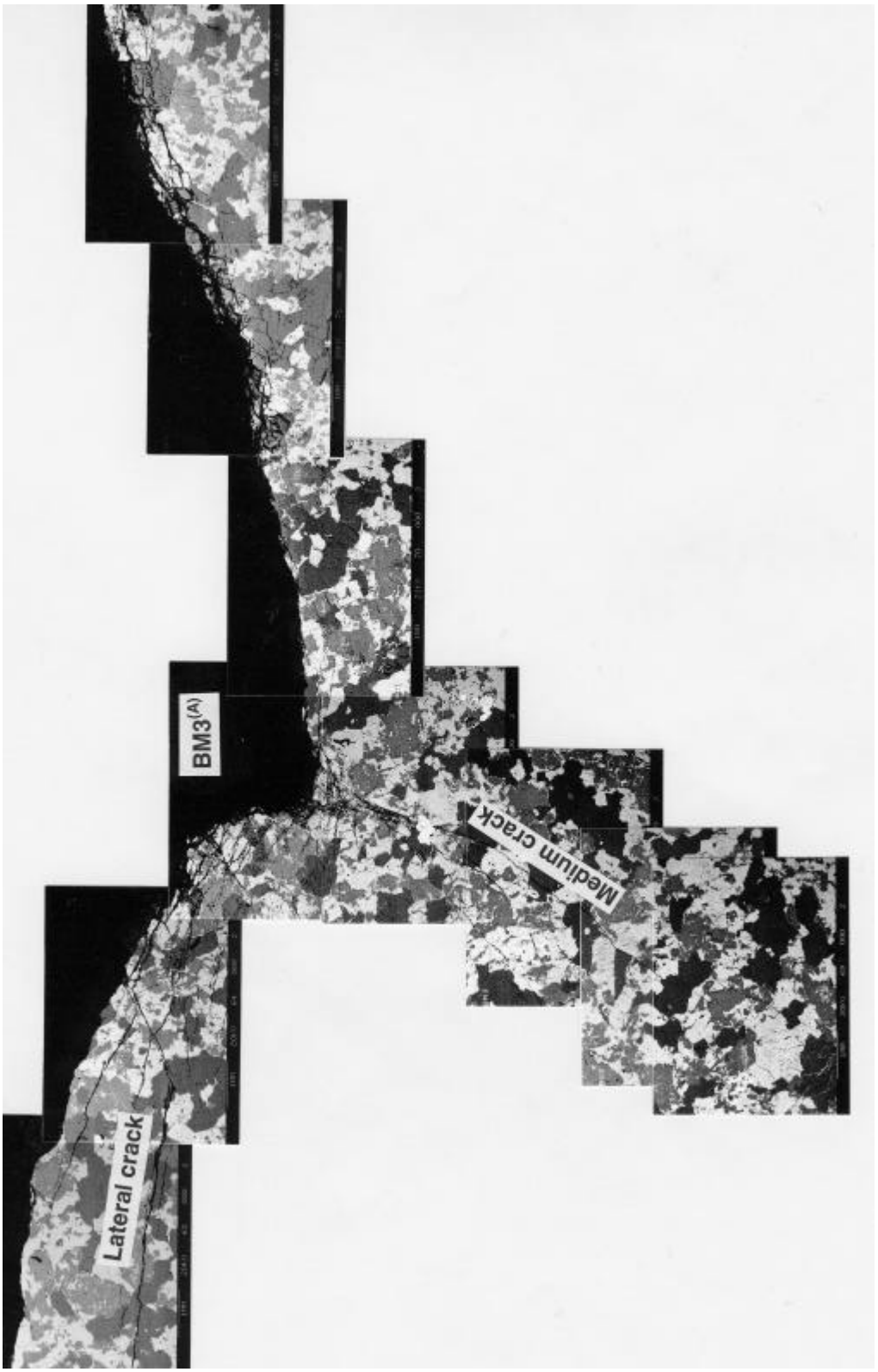

(c). The crater with a densely cracked zone, lateral cracks and medium cracks corresponding to BM3$^{(A)}$. The densely cracked zone is located around the crater (the black area in the left side) and it consists of many short cracks. The medium cracks are in the right side of the picture.

(d). The crater with a densely cracked zone and a long medium crack corresponding to BM4$^{(A)}$. The densely cracked zone is located around the crater (the black area in the upper part) and it consists of many short cracks. The medium crack is in the lower part of the picture.

(e). The crater with a densely cracked zone and a medium crack corresponding to BM4$^{(C)}$. The densely cracked zone is located around the crater (the black area in the left side) and it consists of many short cracks. The medium crack is in the right side of the picture.

(f). The crater with a densely cracked zone and lateral cracks corresponding to $BSA^{(B)}$. The densely cracked zone is located around the crater (the black area in the left side) and it consists of many short cracks. Lateral cracks are in the upper and lower part of the picture. No medium cracks are found probably because this section does not go through the position where the medium cracks are located.

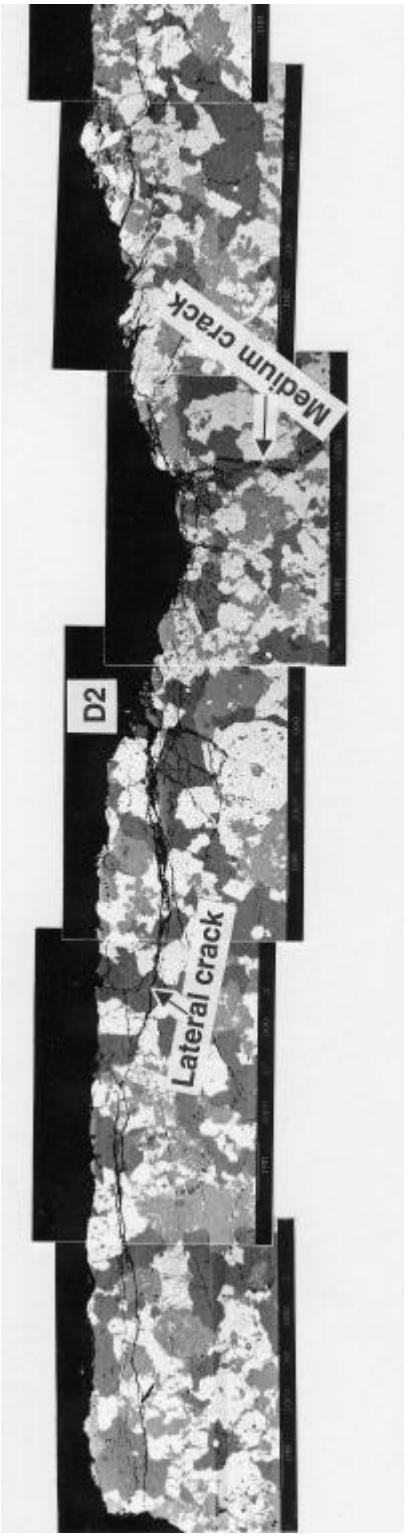

(g). The crater with a lateral crack and a medium crack corresponding to D2 (related to a disc cutter).

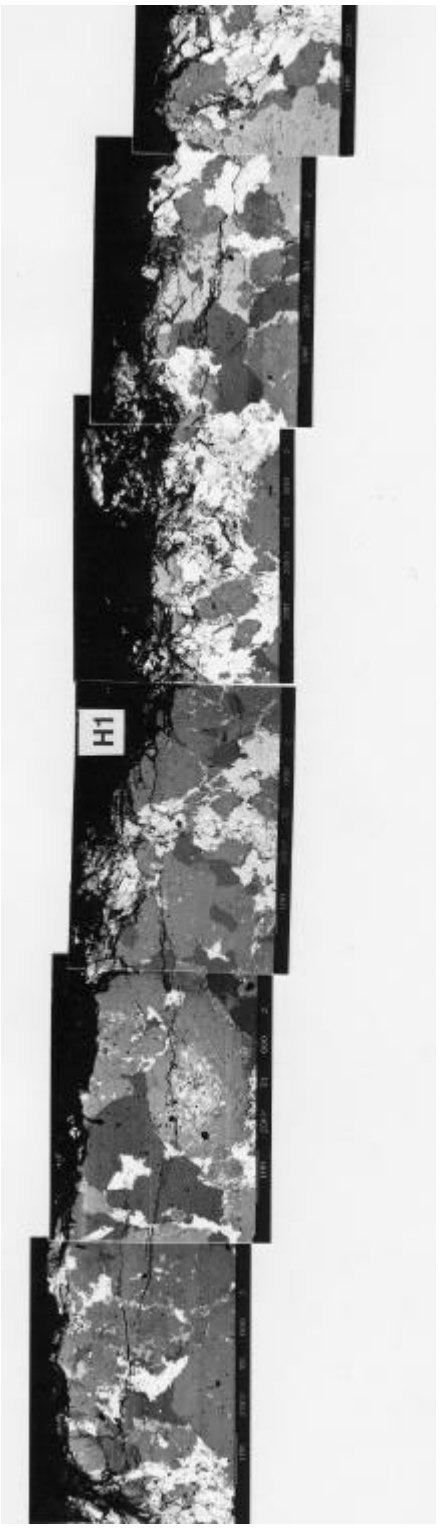

(h). The section of a sample taken from the borehole wall made by disc cutters. There are a long lateral crack and a densely cracked zone near the surface of the borehole wall.

Figure 6-12a–h. *SEM photographs of the cracks induced by mechanical boring. All of original SEM photographs have a same magnification 20, but the magnification we can see from the figures here is approximately 8.*

Equation (6-3) was based on the experimental results from rock mechanics laboratory. The theoretical derivation was based on the assumptions: rigid hemispherical indenter, semi-infinite rock mass, static load, isothermal process as well as homogeneous and isotropic rock material, etc. The field condition is different from these assumptions to a certain extent. However, it is still valid to make a comparison between them. According to linear elastic fracture theory for plain strain problems, the energy release rate G_{Ic} and the fracture toughness have the following relationship:

$$G_{Ic} = (1-\nu^2)\, K_{Ic}^{\ 2} / E \qquad (6\text{-}4)$$

where K_{Ic} is the mode-I fracture toughness of rock. When K_{Ic} is not measured directly, it can be approximately calculated by the following equation obtained from experimental results /Zhang et al., 1998/:

$$\sigma_t = 8.88\, K_{Ic}^{\ 0.65} \qquad (6\text{-}5)$$

where σ_t is the tensile strength of rock. Thus we have

$K_{Ic} = 0.79$ MPa $m^{½}$ and

$G_{Ic} = 12.28\times10^{-6}$ MPam for Äspö diorite,

and

$K_{Ic} = 1.25$ MPa $m^{½}$ and

$G_{IC} = 29.75\times10^{-6}$ MPam for Granite.

Finally we can obtain the relationship between the normal force F_N and the length of the medium crack:

$$L_m = (0.036F_N + 0.78\, F_N^{\ 2})^{2/3} \quad \text{for Äspö diorite} \qquad (6\text{-}6a)$$

$$L_m = (0.022F_N + 0.44\, F_N^{\ 2})^{2/3} \quad \text{for Granite} \qquad (6\text{-}6b)$$

where F_N is in "MN" and L_m in "m". The results from equation (6-6) are presented by two solid lines in Figure 6-13a. The measured crack lengths with their respective normal forces are shown by horizontal solid and dashed lines with two different dot symbols in the figure. From Figure 6-13a we can see that the theoretical length of a medium crack is always larger than the actual length by a few times under a certain normal force. The big difference between the theoretical and the actual lengths is probably caused by the following three major factors. (1) The theoretical results are based on a smooth rock surface into which an indenter or button is pressed, while the practical rock surface in the field is often very rough. (2) The theoretical rock surface is always clean, i.e. it has no previously crushed or broken pieces of rock. However, the actual rock surface often contains some of the previously produced pieces of rock. Such pieces of rock, we believe, greatly reduce the crack length in the field. (3) There is a difference between the confinement of field rock and that of the laboratory rock from which the theoretical result is based on due to the existence of tectonic pressure in the field. The tectonic pressure is an additional confinement to the plane strain condition. It

increases the compressive strength and energy release rate in equation (6-3) and would reduce the crack length further.

Assuming that an average value of the measured minimum and maximum normal forces corresponding to a crater is the actual normal force producing the crater, we can then find that the measured lengths of the medium cracks basically increase with increasing normal forces. This trend is similar to the theoretical results. Moreover, the theoretical results can be approximately modified by multiplying equation 6-6 by a modification factor. Thus, the modified equation can be used to predict the crack length or cracked zones induced by mechanical boring in practice. The modified results corresponding to equation 6-6 are shown in equation (6-7).

$$L_m = C_1 (0.036\, F_N + 0.78\, F_N^{\,2})^{2/3} \qquad \text{for Äspö diorite} \qquad (6\text{-}7a)$$

$$L_m = C_2 (0.022 F_N + 0.44\, F_N^{\,2})^{2/3} \qquad \text{for Granite} \qquad (6\text{-}7b)$$

where C_1 and C_2 are modification factors which should be less than or equal to 1. In addition to the medium cracks, we measured the lengths of the side cracks. The results are shown in Table 6-11 and Figure 6-13b. We can also see that the length of the side cracks has a weak increasing tendency with increasing normal forces.

In addition to the samples for the button cutter, three samples for the disc cutter were also taken from the bottom of the test borehole. Unfortunately, we did not measure the cutter forces of the disc cutters in the field due to the limitation of the testing system. Therefore, we cannot quantitatively compare the crack sizes induced by the button cutter and those induced by the disc cutter. In addition, it was found that no large medium cracks could be seen in the samples taken from the side walls of both borehole 1 and borehole 2. And we did not find clear differences between the crack sizes made by the disc cutters in the side wall of borehole 1 and those made by the button cutters in the side wall of borehole 2.

6.6 Cracked zones around borehole

According to the measurements of the crack length in the rock samples taken from the bottom and wall of the borehole, the cracked zones around the borehole can be approximately determined, which is shown in Figure 6-14 and 6-15. Here a cracked zone is defined as the region that can cover all the cracks induced by cutter forces. The maximum depth of the cracked zone is equal to the length of the longest medium crack. Within the cracked zone, a densely cracked zone can be found near the surface of the bottom or wall of the borehole. In the densely cracked zone there are many short cracks.

The maximum depth of the densely cracked zone is about 2.5–3 mm according to the approximate measurements of the rock samples listed in Table 6-11. Correspondingly, the maximum depth of the cracked zone is 27.1 mm according to Table 6-11. Such a maximum depth is produced by a possible maximum normal force of 531 kN. However, we know that the maximum normal force of the front cutter in the first 7 minutes of boring in casing 10 is 684 kN. Therefore, it is possible that in the last rotation of boring of casing 10 the maximum normal force of other front button cutters can reach 684 kN.

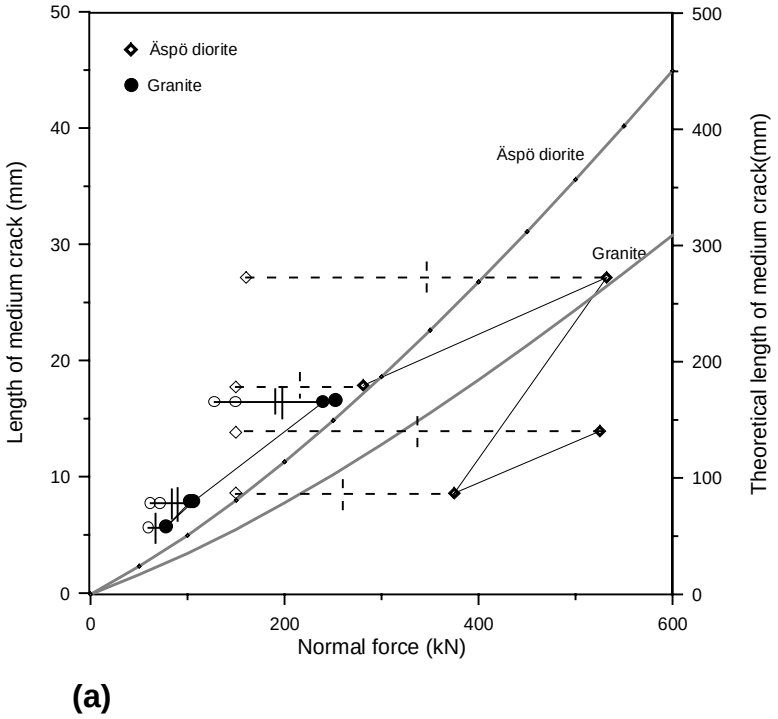

(a)

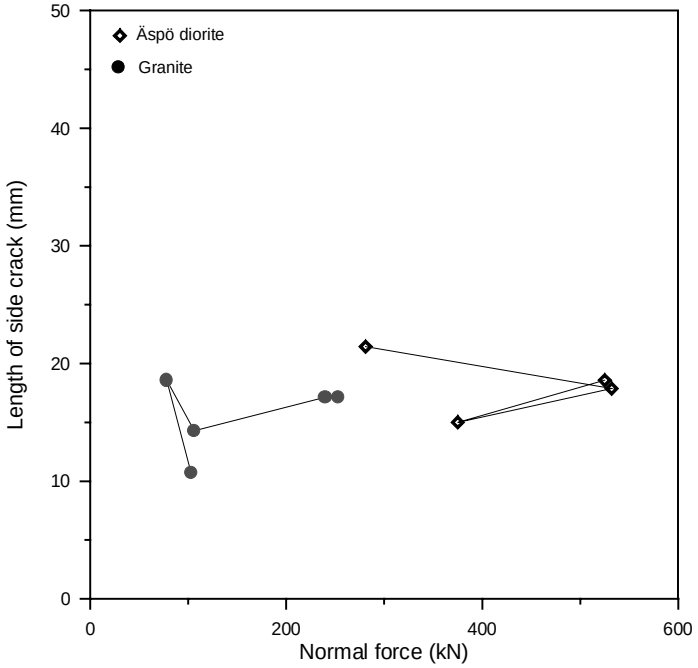

(b)

Figure 6-13. *Relationship between normal force and crack length. (a) medium cracks, (b) side cracks.*

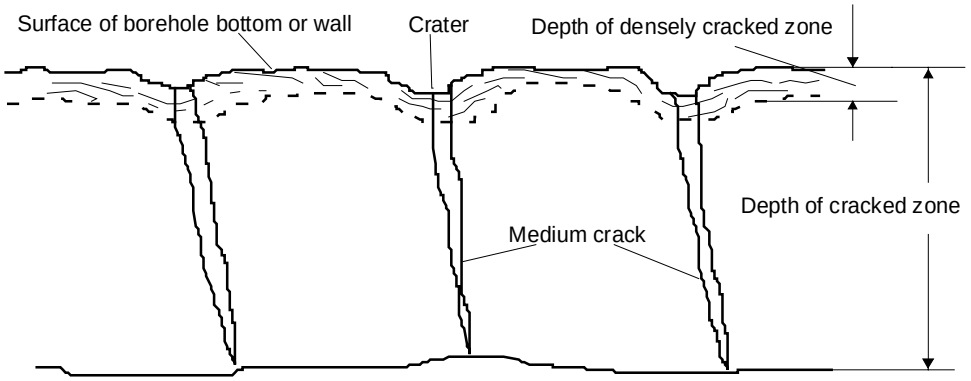

Figure 6-14. *Cracked zone and densely cracked zone.*

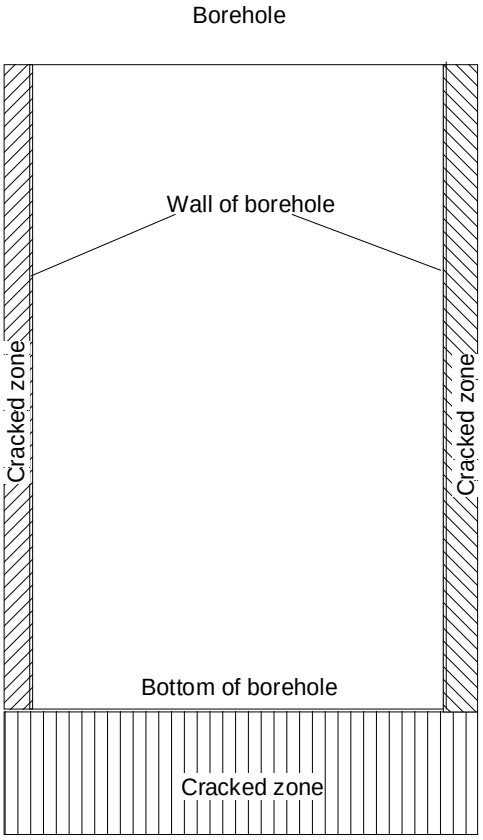

Figure 6-15. *Cracked zones around borehole.*

If so, the depth of the cracked zone in the bottom of the borehole should be larger than 27.1 mm. Assuming that $C_1 = 0.1$ in equation 6-7a, then the maximum depth of the cracked zone near the bottom of the borehole might be estimated by using equation 6-7a as $F_N = 684$ kN. Thus we can obtain $L_m = 53$ mm. In addition, assume that 106 kN is or is close to the maximum normal force in the last rotation of boring of the gauge cutters, then we know that the relevant medium crack length is 7.86 mm from Table 6-11. Therefore, the possible maximum cracked zones around the borehole can be shown in Figure 6-15: on the bottom, the maximum depth of the cracked zone would be 53 mm, while in the side wall the maximum depth of the cracked zone would be approximately 7.86 mm. Here the angle between the medium cracks produced by gauge cutters such as cutter 18A and the surface of the borehole wall is approximately considered to be 90°. And it is considered that the medium cracks in the wall of the borehole are produced by the outermost gauge cutters.

7 Discussion

7.1 Relationship between cutter forces and length of cracks

As described in Chapter 6, the theoretical length of a medium crack produced by a hemispherical button is always larger than the actual measured length by a few times when the normal (or indentation) forces of the theoretical case and the field case are equal. The big difference is mainly caused by three factors, which is discussed in Chapter 6. Therefore, a further fundamental study on the relationship between a normal or indentation force and the length of a medium crack (or other cracks) is necessary. Because the present theoretical result is based on laboratory indentation tests that seldom consider rock confinement, the roughness of the rock surfaces indented, and the rock debris on the surfaces, the further fundamental and laboratory studies should consider such factors. In addition, a series of field tests, including cutter force measurements and crack examinations, are also necessary so as to verify or modify relevant theoretical results. If such tests were to be conducted, a better theoretical result would be obtained which could be used for predicting cracked zones induced by mechanical boring in practice.

7.2 Estimation of loading rates in field mechanical excavation

K_{Ic} is the fracture toughness of the rock at Äspö, T_c the critical time (the time from zero force to the peak of the normal force), and $\dot{k}$ the loading rate. Here we assume that the crack starts to be unstable at the peak value of the normal force. According to the measured results for the normal force in casing 10 shown in Figure 7-1, as $F_N > 60$ kN, the T_c in every normal force wave is approximately between 0.019 seconds and 0.2 seconds, i.e. $T_c = 0.019–0.2$ s. According to dynamic fracture mechanics, the loading rate can be expressed by:

$$\dot{k} = K_{Ic} / T_c \qquad (7\text{-}1)$$

According to the measured results /Zhang et al., 1999/, the fracture toughness of gabbro $K_{Ic} = 3–60$ MPa $m^{½}$. Here the maximum fracture toughness of gabbro was obtained in high-speed impact loading. Assuming that the fracture toughness of the two rocks at the Äspö underground laboratory is within $K_{Ic} = 3–60$ MPa $m^{½}$, then the actual maximum loading rate of the boring machine should be

$$\dot{k} \approx 10^{1}–10^{3} \text{ MPa } m^{½} s^{-1} \qquad (7\text{-}2)$$

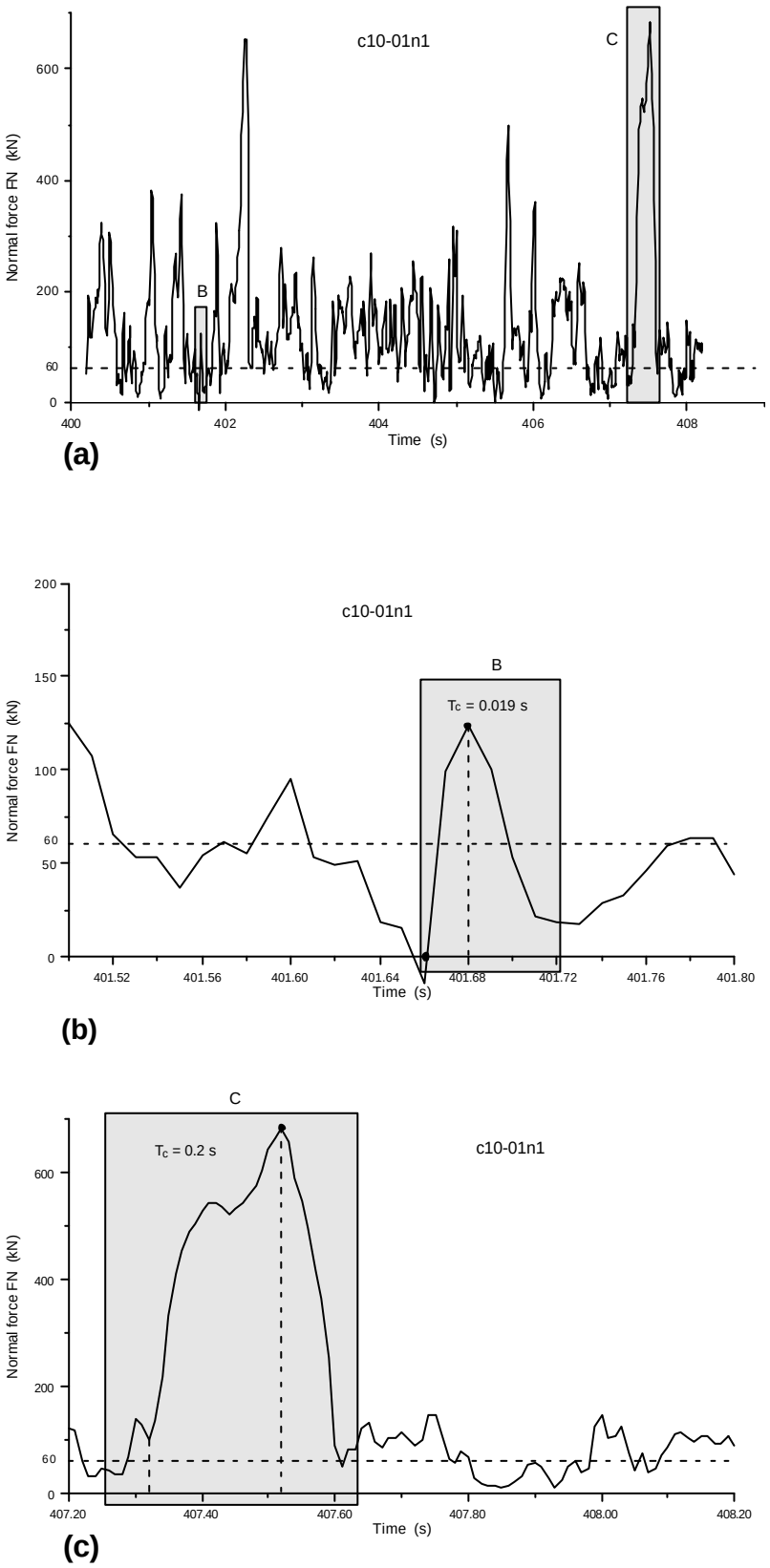

Figure 7-1. *Estimate of actual loading rate of boring machine.*

This belongs to typical quasi-static loading. Under such quasi-static loading, according to a study on Fangshan gabbro and Fangshan marble, the fracture toughness of the rocks is almost constant (as the loading rate $\dot{k} \leq 10^4$ MPa $m^{½} s^{-1}$) and it is much smaller than their dynamic toughness /Zhang et al., 1999/. In addition, the energy utilisation is much higher in quasi-static loading than in dynamic loading /Zhang et al., 2000/. This shows that the loading rate of the boring machine is proper from the viewpoints of both rock fracture and energy utilisation. However, a big potential for increasing the boring speed of the machine still exists, because the loading rate of the machine could be increased to 10^4 MPa $m^{½} s^{-1}$ by increasing its rotation speed, etc., while the fracture toughness and energy utilisation are still kept small and high respectively.

7.3 Boring machine design and borehole quality

The mechanical boring at Äspö shows that the boring machine design is related to the quality of the borehole. For example, when the boring machine was installed with all the disc cutters, the borehole wall was smooth. However, when the machine was installed with 16 button cutters and 4 disc cutters, the wall of borehole 2 was very rough and many grooves were produced. The major reason for the difference in the wall's quality between the two cases is that the button cutters cause a large side force that is applied to the boring machine, see Figure 7-2. This makes the machine move in the

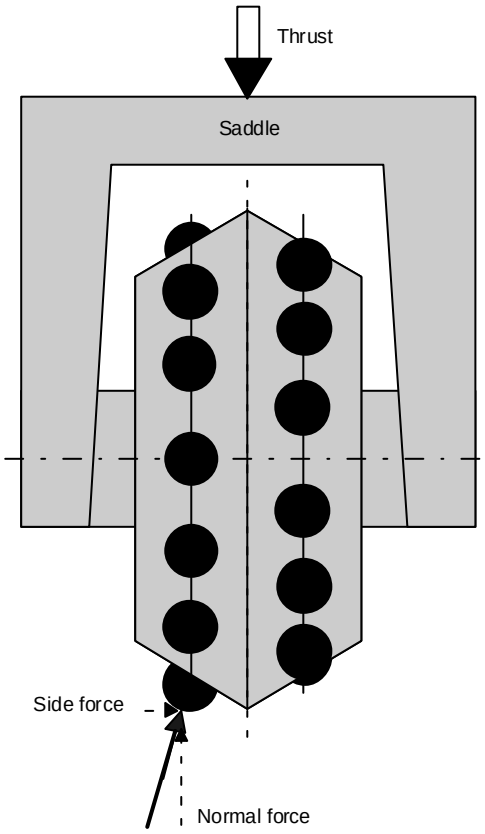

Figure 7-2. *Diagram of loading process of the button cutters.*

horizontal direction and against the wall of the borehole. In this situation one of the outermost gauge cutters is driven into the side wall of the borehole due to the large side force of the machine. The buttons on the gauge cutter are simultaneously pressed into the side wall and they produce rock breakage. Thus, the grooves on the wall of the borehole are produced. This explanation can be confirmed by means of the photograph of the borehole in Figure 6-1. This photograph was taken just after boring breaking of the borehole in the field. The white spots in the photograph are the craters produced by the buttons on the button cutters. From the photograph it can be found that the distance between any two neighbouring grooves on the side wall is equal to the distance between two neighbouring buttons (on one row of buttons) on the gauge cutter. In addition, the field investigation showed that all grooves on the side wall ended on the circle that is just the track of two outermost gauge cutters. Therefore, the grooves on the side wall of the borehole can only be made by the buttons on the outermost gauge cutters.

The above description does not mean that any kind of button cutter definitely causes a large side force on a boring machine. However, this depends on the kind of button cutter used, and particularly on the button distribution. The button cutter shown in Figure 7-2 definitely causes a large side force, because the distribution of the two rows of buttons is not symmetric. Therefore, such a distribution of the buttons should be avoided in the design of the boring machine, so that the side force induced may be reduced to as small a value as possible.

8 Conclusions

- The method of measuring cutter forces in this study is feasible for the boring machine used at Äspö, and it should be valid for other TBM machines.
- The force-coupling phenomenon is not negligible in the measurements of the cutter forces according to this study. Particularly in the case of the button cutters in this study, the coupling phenomenon must be considered.
- The cutter force of the front cutter is much larger than the cutter force of the gauge cutter. Therefore, the medium cracks produced in the bottom are usually longer than those in the wall. With regard to nuclear waste repositories, short medium cracks in the wall should be better than long ones.
- The loading rate of the boring machine is within quasi-static loading. Such a loading rate is proper for rock fracture and fragmentation. However, this loading rate could be greatly increased to a high value such as 10^4 MPa $m^{½}s^{-1}$. If so, the boring speed of the machine would be highly improved, whereas the cracking zone would not be increased.
- The original theoretical relationship between the normal force and the medium crack length could be modified by using a modification factor (≤ 1). However, a further study based on both laboratory and field tests is necessary to develop and modify the present theoretical result.
- It is recommended that the high temperature in the cutters of the boring machine during boring should be considered in the design and manufacture of boring machines, particularly when the continuous boring time is long and the rotation speed of the machine is high.
- The design of the button cutters of the boring machine in this study is unreasonable; i.e. the asymmetrical distribution of the buttons in the button cutter easily causes a side force. Such a side force from each button cutter gives rise to a large side force that is applied to the boring machine. This is harmful to both the boring machine and the quality of the borehole.
- The results from both the theoretical investigation and the in-situ measurements show that the length of a medium crack produced by button cutters in the rock increases with an increasing normal force. In order to avoid long medium cracks in the bottom or wall of a borehole, the thrust of a boring machine should be kept to as small a value as possible. In other words, too high a thrust should be avoided if we want to reduce the crack length or the cracked zone surrounding the borehole.

9 Acknowledgements

The financial support from the Swedish Nuclear Fuel and Waste Management Co. (SKB) is greatly acknowledged. The authors are very grateful to Dr Xiangchun Tan, Ms Åsa Johansson, Mr Ulf Mattila, Mr Christer Andersson, Mr Josef Forslund, and Mr Lars Åström for their help in the experimental design and measurements, to Mr Christer Svemar, Professor Roland Pusch, and Mr Gunnar Ramqvist for their valuable comments and suggestions for the testing plan for the cutter forces and cutter temperature, and to Dr Chunlin Li and Dr Milan Veljkovic for their help in the numerical simulation and data analysis. In addition, the authors would like to thank Mr Dennis Ofiara and his colleagues from the Boretec Company for their help in supplying the cutters for the tests, and Professor Levent Ozdemir and his colleagues for their comments on the test plan.

10 References

Cooper G, Liu Z, Yang M, 1994. The wear of thermally stable diamond during rock cutting. Journal of Energy Resources Technology, Transactions of the ASME 116:268–272.

Hopkins M J, Foden R L, 1979. The in-situ measurement of dynamic cutter forces on raiseborer reaming heads, Proc. Conf. on Mining Machinery, 335–338. Brisbane, July 2–6, 1979.

Kou S Q, 1995. Some basic problems in rock breakage by blasting and by indentation. Doctoral Thesis, 1995:180D, Luleå University of Technology.

Kou S Q, Tan X C, 1995. Test plan for sampling in Äspö TBM tunnel and crack discrimination in laboratory at LuTH. Working document for SKB.

Lindqvist P-A, Tångring S, Rånman K-E, 1979. Mekanisk bergfragmentering – Laboratorieförsök med fullborrning i full skala, Teknisk rapport, 1979:17T.

Lindqvist P-A, Suarez L M, Montoto M, Tan X C, Kou S Q, 1994. Rock indentation data base – testing procedures, results and main conclusions, SKB PR 44-94-023, Swedish Nuclear Fuel and Waste Management Co.

Morell R J, Larson D A, 1974. Tunnel boring technology – disk cutter experiments in metamorphic and igneous rocks. Twin Cities Mining Research Center, Minnesota, U. S. Dept. of the Interior, USBM RI 7961.

Ozdemir L, Dollinger J, 1987. Laboratory studies of high speed tunnel boring. In: Proc. Rapid Excavation and Tunneling Conference. Society of Mining, Metallurgy, and Exploration, Inc (SME) of the American Institute of Mining, Metallurgical, and Petroleum Engineers. Vol. 1, pp.165–187.

Roxborough F F, 1985. Research in mechanical rock excavation: progress and prospects. In: Proc. Rapid Excavation and Tunneling Conference. Society of Mining, Metallurgy, and Exploration, Inc (SME) of the American Institute of Mining, Metallurgical, and Petroleum Engineers. Vol. 1, pp.225–244.

Samuel A E, Seow L P, 1984. Disc force measurements on a full-face tunnelling machine, Int. J. Rock Mech. Min. Sci. & Geomech. Abstr., 21, 83–96.

Snowdon R A, Ryley M D, Temporal J, 1982. A study of disc cutting in selected brittle rocks, Int. J. Rock Mech. Min. Sci. & Geomech. Abstr., 19, 107–121.

Svemar C, 1995. Quality plan for rock sampling in Äspö TBM tunnel, SKB document.

Takaoka S, Hayamizu H, Misawa S, 1973. Studies on the cutting of rock by rotary cutters – Part 1. Rock cutting by disc cutters. Tunnels and Tunnelling, March, 181–185.

Tan X C, Kou S Q, 1995. Quality plan for crack discrimination in laboratory at LuTH. Working document for SKB.

Wang F D, Miller R, Ozdemir L, 1974. Improving hard rock tunneling through comparison of laboratory and field tunnel boring studies. In: Proc. Rapid Excavation and Tunneling Conference. Society of Mining, Metallurgy, and Exploration, Inc (SME) of the American Institute of Mining, Metallurgical, and Petroleum Engineers. Vol. 2, pp.1741–1757.

Zhang Z X, Kou S Q, Lindqvist P-A, Yu Y, 1998. Relationship between fracture toughness and tensile strength of rock. In: YU MH, Fan SC, editors. Strength Theories: Applications, Development & Prospects for 21st Century. Beijing/New York: Science Press, p.215–219.

Zhang Z X, Kou S Q, Yu J, Yu Y, Jiang L G, Lindqvist P A, 1999. Effects of loading rates on rock fracture. Int. J. Rock Mech. & Min. Sci. 36(5), 597–611.

Zhang Z X, Kou S Q, Jiang L G, Lindqvist P A, 2000. Effects of loading rates on rock fracture: Fracture characteristics and energy partitioning. Int. J. Rock Mech. & Min. Sci. 37(5), 745–762.

Appendix A: Determination of the coefficients a_1, $a_2 \ldots a_9$ for the front cutter (cutter 3)

The coefficients α_1, α_7, α_4, α_3, α_9 and α_6 can be easily determined according to equations (3-2) and (3-3). The typical curves showing the calibrated results for the coefficients are shown in Figure A-1.

From Figure A-1 we can see that the result of the curve fit is quite good. The calibration results for the six coefficients are listed in Table A-1. We take the average value of each coefficient as the final coefficient.

Unlike the 6 coefficients above, the other three coefficients, α_2, α_5 and α_8, are difficult to determine, because the curves corresponding to these coefficients are not linear, see the curves in Figure A-2. From the figure we can conclude the following. (1) The curves relevant to α_2 and α_8 are complicated rather than linear. This will cause the determination of α_2 and α_8 to be very difficult, and further will give rise to some errors in the calibration. (2) The curve corresponding to α_5 can be approximately taken as linear. (3) One-time loading and repeat loading give rise to different shapes of the curves relevant to α_2 and α_8.

According to the observation made during the calibration in the laboratory, a one-time loading, except for an independent lateral loading, always produces one or a few shallow holes with clear plastic deformation in the steel plate beneath the cutter. We think that this situation is different from that in field excavation, because it is impossible to produce such big plastic-deformation holes with the cutter in rock. Therefore, we think that repeat loading (the buttons in the cutter entered in the same holes produced previously) is more similar to the real situation in field rock excavation. In addition, we find that the values of α_2 and α_8 determined using all the data and the corresponding values determined using part of the data ($F_T>0$) vary greatly. Considering that in field rock excavation three forces usually appear at the same time, we choose the values determined from the data with $F_T>0$. Thus we obtain the final values of α_2, α_5 and α_8: $\alpha_2 = 0.0127$, $\alpha_5 = -0.1011$, and $\alpha_8 = -0.0131$.

As described above, the values of α_2 and α_8 are not so stable as that of the other coefficients. In other words, they have a poor repeatability in calibration. Particularly, their values usually change too much. One of the main reasons is possibly that the cutter is loaded asymmetrically, due to the fact that no two buttons in any row in the cutter are in a single line parallel to the axis of the cutter. The above facts influence the calibration result. Therefore, if necessary, the calibration should be modified.

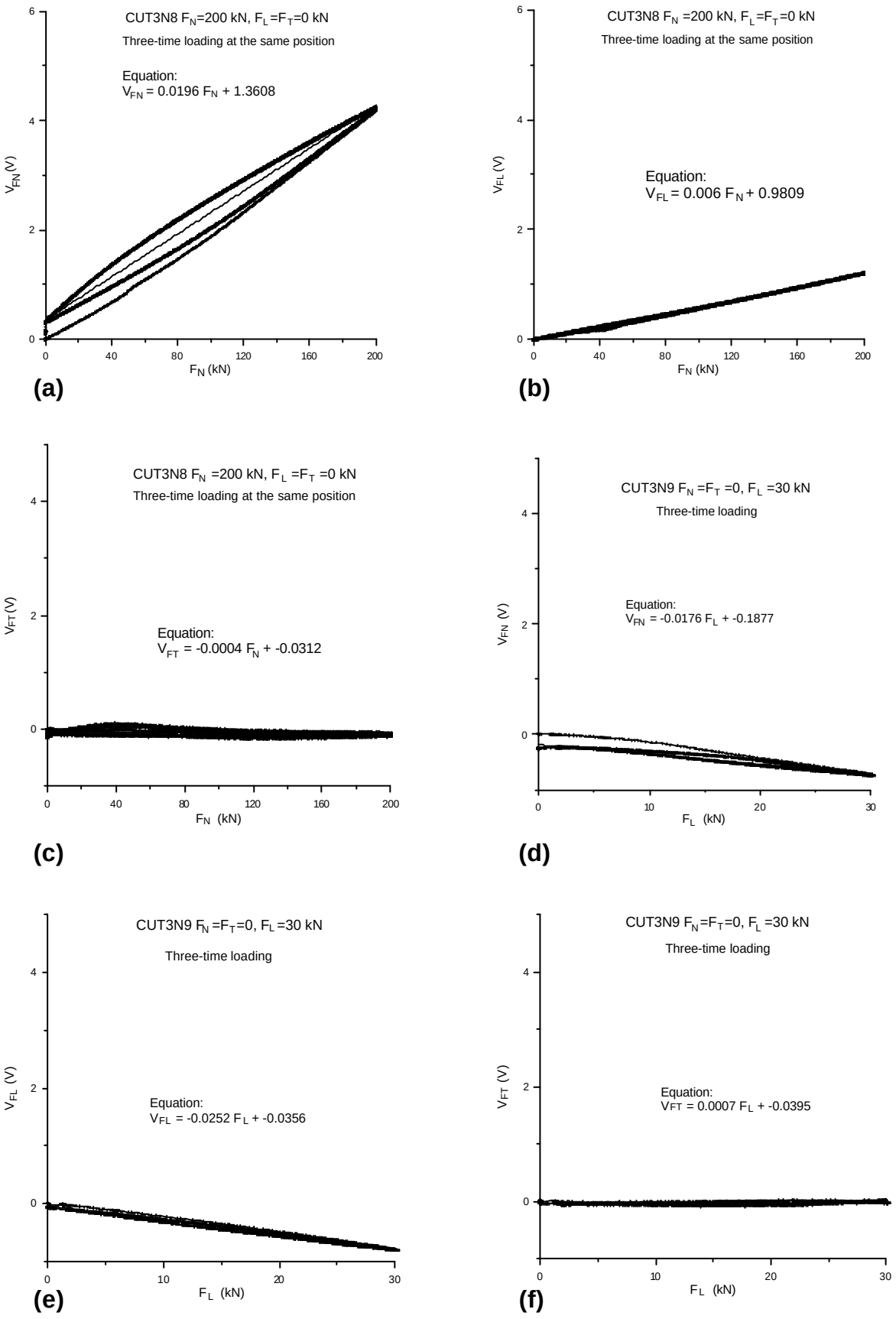

Figure A-1. *Calibration curves relevant to the coefficients a_1, a_3, a_4, a_6, a_7 and a_9.*

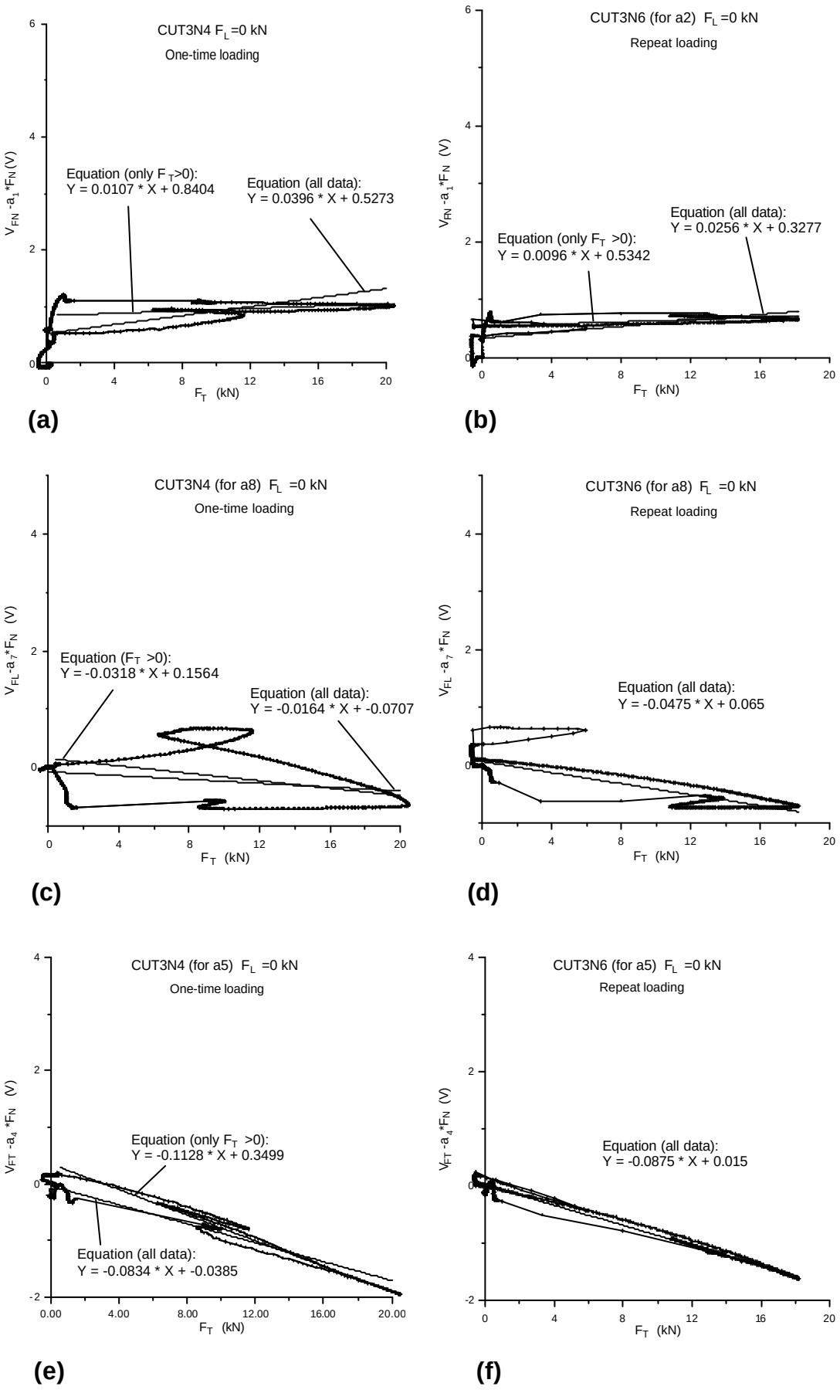

Figure A-2. *Calibration curves relevant to the coefficients* a_2, a_5 *and* a_8.

Table A-1. Calibration results for cutter 3.

Cal. No.	a_1 V_{FN}/F_N R	a_7 V_{FL}/F_N R	a_4 V_{FT}/F_N R	a_3 V_{FN}/F_L R	a_9 V_{FL}/F_L R	a_6 V_{FT}/F_L R
2	0.0194	0.0048	-.0002			
3				-.0175	-.0274	-.0015
7	0.0201	0.0053	-.0007			
8	0.0196	0.0060	-.0004			
9				-.0176	-.0252	0.0007
Average values	0.0197	0.0054	-.0004	-.0176	-.0263	-.0007

Table A-2. Calibration results for cutter 3.

(a)

Cal. No.	a_2 $(V_{FN} - a_1 F_N) / F_T$			
	O-loading		R-loading	
	a_2^{a*}	$a_2^{p\#}$	a_2^{a}	a_2^{p}
4	0.0396	0.0107		
10	0.0478	0.0169		
11	0.0485	0.0147		
15	0.0302	0.0157		
6			0.0256	0.0096
12			0.0554	0.0133
16			0.0275	0.0152
Average	0.0415	0.0145	0.0361	0.0127
Final				0.0127

(b)

Cal. No.	a_8 $(V_{FN} - a_1 F_N) / F_T$			
	O-loading		R-loading	
	a_8^{a}	a_8^{p}	a_8^{a}	a_8^{p}
4	-0.0164	-0.0318		
10	-0.0312	-0.0689		
11	-0.0307	-0.0307		
15	0.0079	0.0403		
6			-0.0475	-0.0519
12			-0.07	-0.0468
16			0.0253	0.0593
Average	-0.0176	-0.0228	-0.0307	-0.0131
Final				-0.0131

(c)

Cal. No.	$(V_{FN} - a_1 F_N) / F_T$			
	O-loading		R-loading	
	a_5^a	a_5^p	a_5^a	a_5^p
4	-0.0834	-0.1128		
10	-0.0859	-0.1008		
11	-0.097	-0.097		
15	-0.1210	-0.1210		
6			-0.0875	-0.0875
12			-0.0928	-0.0928
16			-0.123	-0.123
Average	-0.0968	-0.1079	-0.1011	-0.1011
Final				-0.1011

In Table A-2 the symbol "*" means that the coefficient was determined by all the data, and "#" does that the coefficient was determined by part of the data or the data with $F_T>0$. "R" and "O" represent repeat loading and one-time loading, respectively.

Finally, we obtain all the values of α_1–α_9 for cutter 3.

$$\left.\begin{aligned} a_1 &= 0.0197 \\ a_2 &= 0.0127 \\ a_3 &= -0.0176 \\ a_4 &= -0.0004 \\ a_5 &= -0.1011 \\ a_6 &= -0.0007 \\ a_7 &= 0.0054 \\ a_8 &= -0.0131 \\ a_9 &= -0.0263 \end{aligned}\right\} \qquad \text{(A-1)}$$

Appendix B: Modification of equations for front cutter

Two laboratory tests numbered CUT3N14 and CUT3N18 are used to make the modification. In both tests repeat loading was used and all the three directional loads were applied. The forces calculated by equation (3-7) and their respective real forces are shown in Figure B-1.

B.1 Characteristics of the differences between the calculated forces and the real forces

From Figure B-1 we can see that there exists a big difference between the real F_L and the calculated F_L around the second peak F_T. Because the peak values of the three forces are very important, we should make some modifications to equation (3-7), so that we may obtain a new equation to give a correct calculation result. After analysing all the calibration tests, we find that a positive value of the coefficient α_8 always gives a better result around the second peak of F_T. In addition, considering that the repeat loading condition is close to the field excavation situation, we choose $\alpha_8 = 0.0593$ from the test numbered CUT3N16, which was performed with a repeat loading. This can be seen in Figure B-2.

When $\alpha_8 = 0.0593$ and the other coefficients are not varied, equation (3-7) is changed into:

$\Delta = 4.3826\times10^{-5}$

$1/\Delta = 2.28\times10^{4}$

$$\left.\begin{aligned} F_N &= 61.6V_{FN} - 40.79V_{FL} - 16.19V_{FT} \\ F_T &= -0.33V_{FN} + 0.48V_{FL} - 9.65V_{FT} \\ F_L &= 11.91V_{FN} - 45.31V_{FL} - 25.08V_{FT} \end{aligned}\right\} \quad \text{(B-1)}$$

B.2 Modification

From Figure B-2 we can easily find that the differences between the real three forces and the forces calculated by equation (B-1) are basically proportional to the real cutter forces. Furthermore, we can draw the following conclusions.

- From Figure B-2a we can see that, when F_L is increased from 0 to 15 kN (the real F_N was kept constant and the real F_T was 0 kN), the F_N calculated by equation (B-1) is increased from $(F_N)_A$ to $(F_N)_B$. Obviously, the difference between $(F_N)_A$ and $(F_N)_B$ is induced only by F_L. In other words, an increase in the real F_L causes the calculated F_N to increase by a certain value.

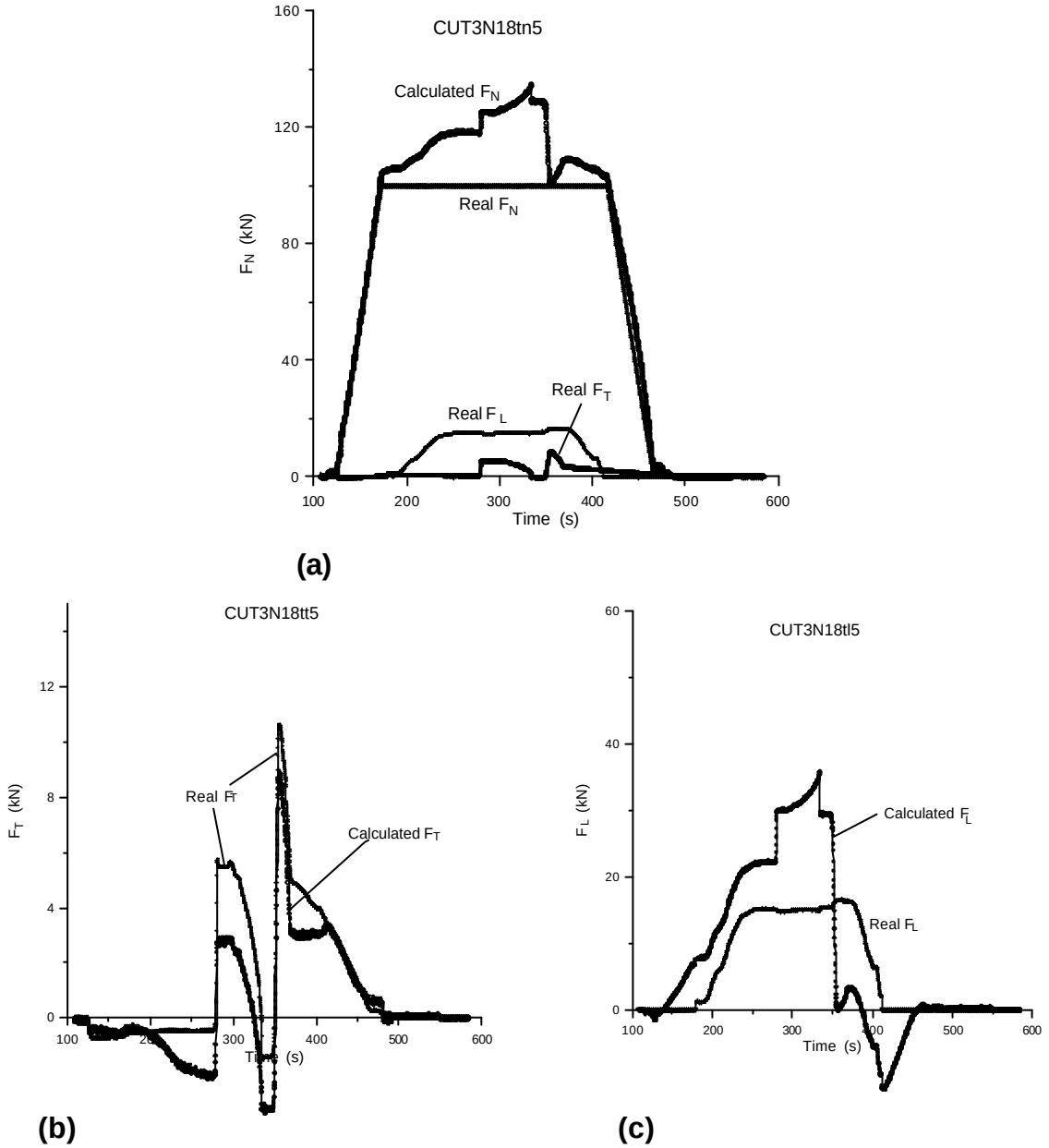

Figure B-1. *Comparison between the real forces and the forces calculated by equation (3-7).*

- From Figure B-2a we can also find that the calculated F_N is increased from $(F_N)_B$ to $(F_N)_C$ only due to the increase in F_T. A similar phenomenon is found at point E in the figure. However, the ratio between the increment of the F_N calculated at point C and the real F_L at C is different from that between the increment of the F_N calculated at point E and the real F_L at E. One main reason is that the determination of the coefficient α_8 does not follow both peak values of F_T.

- From Figure B-2b we can see that from point A to B the calculated F_L has a great increment due to an increase in the real F_T. A similar phenomenon can be found at point C in the figure. Similarly to the situation in Figure B-2a, the changes in the F_L calculated at points B and C are different from each other.

- From Figure B-2c we can find that from point A to B the calculated F_T is decreased only because the real F_L is increased from 0 to about 15 kN.

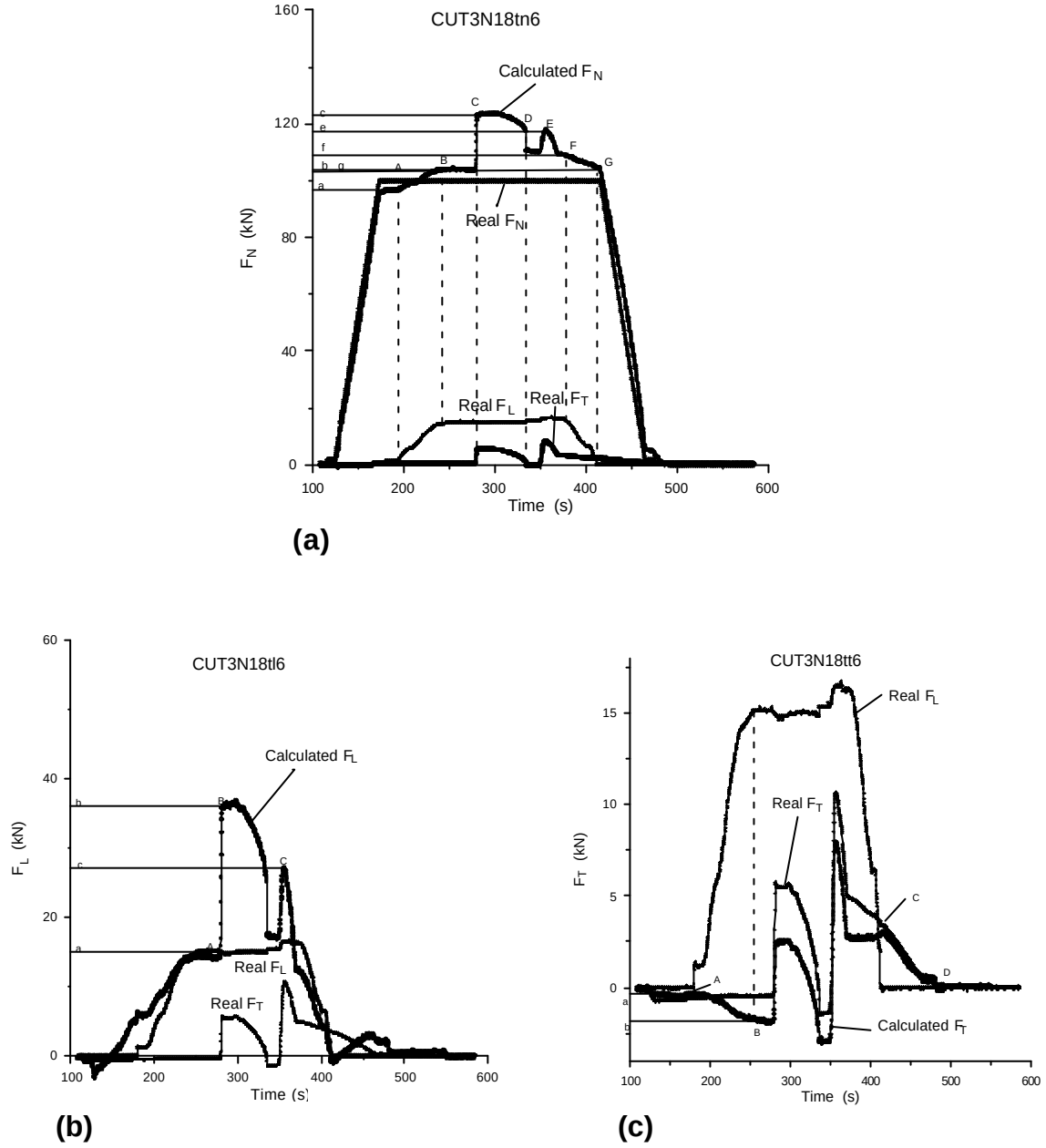

Figure B-2. *Comparison between the real forces and the forces calculated by equation (3-7) with a_8 = 0.0593 instead of a_8 = -0.0131.*

All the above phenomena are also found in the test for CUT3N14. The data related to the above phenomena are listed in Table B-1.

In Table B-1 F_L^r is the real F_L applied in the laboratory tests. ΔF_N^c is the increment of the calculated F_N induced by the real F_L. The other parameters have similar meanings.

From the data in Table B-1 we can obtain some modification factors. They are listed in Table B-2.

Table B-1. Data for the increments of the calculated forces for CUT3N18 and CUT3N14.

Test	F_L^r	DF_N^c	DF_T^c	F_T^r(kN)		DF_N^c(kN)		DF_L^c(kN)	
No.	(kN)	(kN)	(kN)	Peak1	Peak2	Peak1	Peak2	Peak1	Peak2
N18	15	5.9	-1.61						
N14	30	16.3	-3.7						
N18				5.5	10.6	20	13.5	21	12
N14				10	21	34.8	18.5	45	18.8

Table B-2. Modification factors from CUT3N18 and CUT3N14.

Test	DF_N^c/F_L^r	DF_T^c/F_L^r	DF_N^c/F_T^r		DF_L^c/F_T^r	
No.			Peak1	Peak2	Peak1	Peak2
N18	0.39	-0.11	3.63	1.27	3.82	1.13
N14	0.54	-0.12	3.48	0.88	4.5	0.9
Average	0.47	-0.12	3.56	1.08	4.16	1.02
			2.32		2.59	

Assuming that the modified forces F_N*, F_L* and F_T* are equal to the respective real forces F_N^r, F_L^r and F_T^r in Table B-2, we can obtain the following results:

$$\left.\begin{aligned} F_L^* &= F_L - 2.59F_T^* \\ F_T^* &= F_T + 0.12F_L^* \\ F_N^* &= F_N - 0.47F_L^* - 2.32F_T^* \end{aligned}\right\} \quad \text{(B-2)}$$

The solution of equation (B-2) is

$$\left.\begin{aligned} F_L^* &= 0.76F_L - 1.98F_T \\ F_T^* &= 0.76F_T + 0.09F_L \\ F_N^* &= F_N - 0.57F_L - 0.83F_T \end{aligned}\right\} \quad \text{(B-3)}$$

Using equation (B-1) we can obtain the three forces F_N, F_L and F_T, and in turn we obtain new results from equation (B-3):

$$\left.\begin{aligned} F_N^* &= 55.09V_{FN} - 15.36V_{FL} + 6.12V_{FT} \\ F_T^* &= 0.82V_{FN} - 3.71V_{FL} - 9.59V_{FT} \\ F_L^* &= 9.71V_{FN} - 35.39V_{FL} + 0.05V_{FT} \end{aligned}\right\} \quad \text{(B-4)}$$

By means of equation (B-4), we can obtain the three forces according to the measured voltages from the strain gauges on the shaft of the cutter. The curves of the comparison between the real forces in the laboratory calibration and the forces calculated by equation (B-4) are shown in Figure B-3.

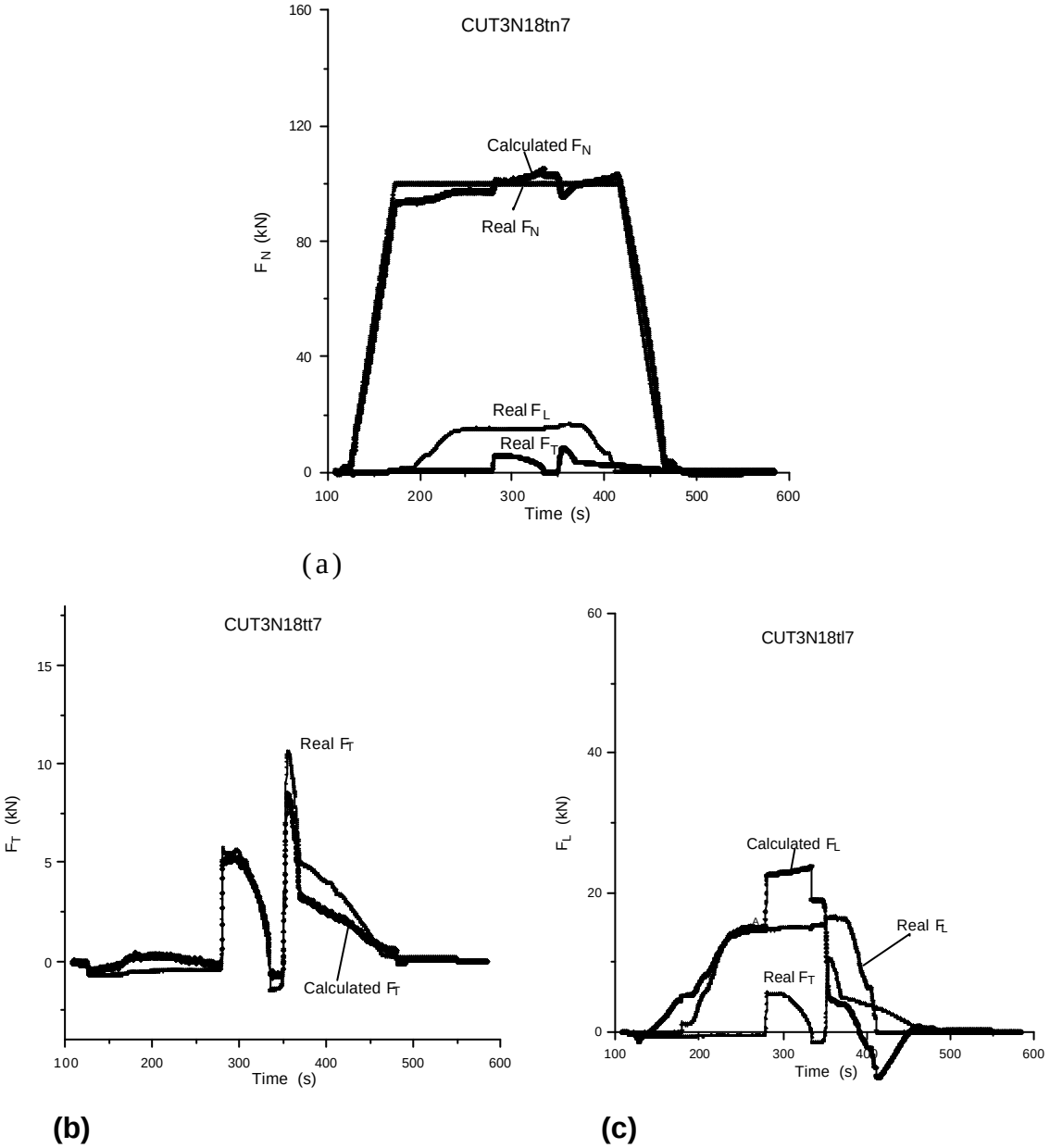

Figure B-3. *Calculated forces and the real forces.*

From Figure B-3 we can see that the results are much better than those in Figure B-2, but the differences between the real forces and the calculated forces around the second peak values of F_T are still clear. This can be further improved by changing the factors $\Delta F_N^c / F_T^r$ and $\Delta F_L^c / F_T^r$. It is found that the smaller the two factors, the better is the fit around the second peak values of F_T. However, as the two factors become small, the differences between the real F_L and the calculated F_L around the first peak values of F_T increase. In order to obtain a better result, we choose $\Delta F_N^c / F_T^r = 1.91$ and $\Delta F_L^c / F_T^r = 2.07$, and $\Delta F_N^c / F_T^r = 1.08$ and $\Delta F_L^c / F_T^r = 1.02$, respectively. After comparison, it is found that the latter choice is better. So we select $\Delta F_N^c / F_T^r = 1.08$ and $\Delta F_L^c / F_T^r = 1.02$. Thus equation (B-2) to (B-4) can be changed into the following:

$$\left.\begin{aligned} F_L^* &= F_L - 1.02F_T^* \\ F_T^* &= F_T + 0.12F_L^* \\ F_N^* &= F_N - 0.47F_L^* - 1.08F_T^* \end{aligned}\right\} \qquad \text{(B-5)}$$

The solution of equation (B-5) is

$$\left.\begin{aligned} F_L^* &= 0.89F_L - 0.91F_T \\ F_T^* &= 0.89F_T + 0.11F_L \\ F_N^* &= F_N - 0.54F_L - 0.53F_T \end{aligned}\right\} \qquad \text{(B-6)}$$

Using equation (B-1) we can obtain the three forces F_N, F_L and F_T, and in turn we obtain the final results from equation (B-6):

$$\left.\begin{aligned} F_N^* &= 55.34V_{FN} - 16.58V_{FL} + 2.47V_{FT} \\ F_T^* &= 1.02V_{FN} - 4.56V_{FL} - 11.35V_{FT} \\ F_L^* &= 10.9V_{FN} - 40.76V_{FL} - 13.54V_{FT} \end{aligned}\right\} \qquad \text{(B-7)}$$

Here the modified cutter forces F_N^*, F_T^*, and F_L^* are in fact the calculated forces shown in Figure B-4. The comparison between the forces calculated by equation (B-7) and the real forces is shown in Figure B-4. Equation (B-7), i.e. equation (3-8) in Chapter 3, will be used to determine the true cutter forces in field tests according to the data for V_{FN}, V_{FL} and V_{FT} measured in the field.

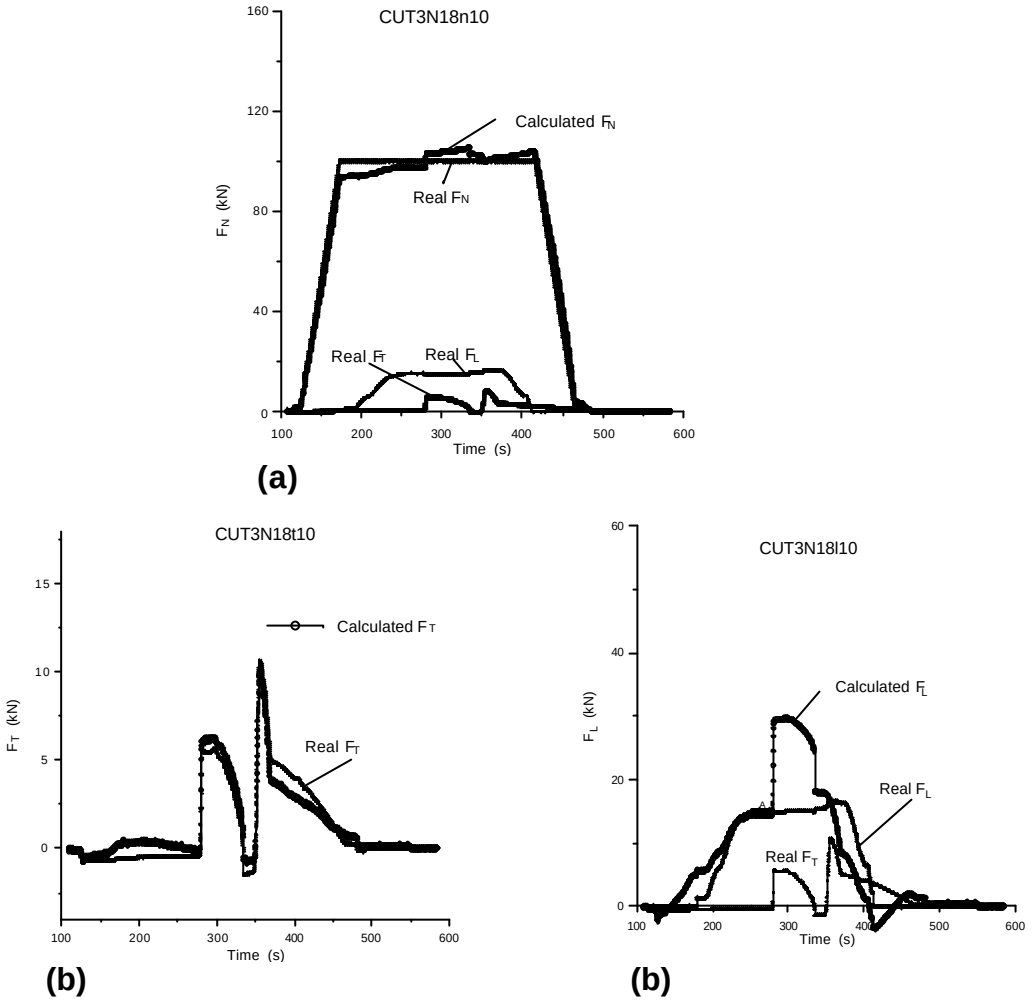

Figure B-4. *Final calculated forces and real forces.*

Appendix C: Data for calibration of cutter 2

Table C-1. Calibration results for cutter 2.

Cal. No.	a_1 V_{FN}/F_N R	a_7 V_{FL}/F_N R	a_4 V_{FT}/F_N R	a_3 V_{FN}/F_L R	a_9 V_{FL}/F_L R	a_6 V_{FT}/F_L R
1	0.0188	0.0058	-.0015			
2				-.0141	-.0213	-.0030
7	0.0172	0.0051	-.0005			
8				-.0140	-.0189	-.0041
15	0.0177	0.0058	0			
16	0.0183	0.0058	-.0006			
Average values	0.0180	0.0056	-.0007	-.0141	-.0201	-.0036

Table C-2. Calibration results for cutter 2.

(a)

Cal. No.	$(V_{FN} - a_1 F_N)/F_T$			
	O-loading		R-loading	
	a_2^{a*}	$a_2^{p\#}$	a_2^{a}	a_2^{p}
4	0.0322	0.0119		
6	0.0164	0.0041		
9	0.0323	-0.0027		
19	0.0196	0.0009		
5			0.0124	0.0205
10			0.0128	0.0024
Average	0.0251	0.0053	0.0126	0.0115
Final				0.0115

(b)

Cal. No.	$(V_{FL} - a_7 F_N)/F_T$			
	O-loading		R-loading	
	a_8^{a}	a_8^{p}	a_8^{a}	a_8^{p}
4	-0.0075	0.0735		
6	-0.0459	-0.0451		
9	-0.0178	-0.0517		
19	-0.0116	-0.0484		
5			0.0118	0.0253
10			-0.0267	-0.0477
Average	-0.0218	-0.0179	-0.0043	-0.0112
Final				-0.0112

(c)

Cal. No.	α_5 $(V_{FT} - a_4 F_N) / F_T$			
	O-loading		**R-loading**	
	a_5^a	a_5^p	a_5^a	a_5^p
4	-0.0828	-0.0867		
6	-0.0555	-0.0974		
9	-0.0963	-0.1078		
19	-0.0993	-0.0988		
5			-0.0728	-0.0871
10			-0.0988	-0.096
Average	-0.0835	-0.0977	-0.0858	-0.0916
Final				-0.0916